IMPACT OF THE TOPOGRAPHY OF THE ACQUISITION SURFACE ON PREPROCESSING AND SUBSEQUENT FREE SURFACE MULTIPLE ELIMINATION AND DEPTH MIGRATION: EXAMINING THE ISSUE AND PROVIDING A PREPROCESSING RESPONSE THAT ACCOMMODATES A VARIABLE TOPOGRAPHY - THEREBY ALLOWING SUBSEQUENT MULTIPLE REMOVAL AND IMAGING METHODS TO DELIVER THEIR PROMISE AND POTENTIAL

A Dissertation Presented to

the Faculty of the Department of Physics

University of Houston

In Partial Fulfillment

of the Requirements for the Degree

Doctor of Philosophy

By

Zhen Zhang

August 2017

IMPACT OF THE TOPOGRAPHY OF THE ACQUISITION SURFACE ON PREPROCESSING AND SUBSEQUENT FREE SURFACE MULTIPLE ELIMINATION AND DEPTH MIGRATION: EXAMINING THE ISSUE AND PROVIDING A PREPROCESSING RESPONSE THAT ACCOMMODATES A VARIABLE TOPOGRAPHY - THEREBY ALLOWING SUBSEQUENT MULTIPLE REMOVAL AND IMAGING METHODS TO DELIVER THEIR PROMISE AND POTENTIAL

Zhen Zhang

APPROVED:

Dr. Arthur B. Weglein, Chairman
Department of Physics

Dr. Lawrence Pinsky
Department of Physics

Dr. Donna Stokes
Department of Physics

Dr. Greg Morrison
Department of Physics

Mr. Cory J. Hoelting
Chevron Energy Technology Company

Dr. Hong Liang
Aramco Services Company

Dean, College of Natural Sciences and Mathematics

Acknowledgements

First, I want to give my sincere gratitude to my advisor, Dr. Arthur B. Weglein. During the past three years of my graduate studies, Dr. Weglein has offered enormous guidance in many aspects including research on Physics, communication skills, team spirit, and most importantly the way to deal with difficulties. Through his classes, oral instructions and papers, I am greatly enlightened by his deep understanding of Physics and seismic exploration. I have greatly benefited from his pursuit for truth.

I would also like to thank my colleagues in M-OSRP. Thanks to Dr. Jim Mayhan for his suggestions in writing papers. Thanks to Prof. Mark Meier, Prof. Fang Liu, Dr. Jinlong Yang, Dr. Chao Ma, Dr. Qiang Fu, Dr. Xinglu Lin, Jing Wu, Yanglei Zou, Yuchang Shen, and Jennifer Chin-Davis for their generous help. Being a member of the Mission-Oriented Seismic Research Program has changed my life.

Thanks to my disseration committee, Prof. Lawrence Pinsky, Prof. Donna Stokes, Prof. Greg Morrison, Mr. Cory Hoelting, and Dr. Hong Liang, for their patience, support and suggestions.

Finally, I feel greatly indebted to my parents for their support, dedication, and love that enable me to finish my degree. As the only child, I love them forever.

IMPACT OF THE TOPOGRAPHY OF THE ACQUISITION SURFACE ON PREPROCESSING AND SUBSEQUENT FREE SURFACE MULTIPLE ELIMINATION AND DEPTH MIGRATION: EXAMINING THE ISSUE AND PROVIDING A PREPROCESSING RESPONSE THAT ACCOMMODATES A VARIABLE TOPOGRAPHY - THEREBY ALLOWING SUBSEQUENT MULTIPLE REMOVAL AND IMAGING METHODS TO DELIVER THEIR PROMISE AND POTENTIAL

An Abstract of a Dissertation

Presented to

the Faculty of the Department of Physics

University of Houston

In Partial Fulfillment

of the Requirements for the Degree

Doctor of Philosophy

By

Zhen Zhang

August 2017

Abstract

This dissertation studies the influence of the topography of the seismic acquisition surface on seismic processing. This is important because in real off-shore and on-shore acquisition, there are many cases in which seismic data have to be acquired along a surface that can be far from horizontal.

This dissertation provides **three** advances and contributions. The **first** examines the issues in preprocessing when the acquisition surface is assumed to be horizontal and it is actually non-horizontal. To address and solve those issues, a new preprocessing formula is derived which accommodates the topography of the measurement surface. Numerical examples compare the preprocessing results that ignore the acquisition topography, and the preprocessing results that accommodate the acquisition topography.

The **second** investigates the effectiveness of inverse scattering series (ISS) free surface multiple elimination that requires deghosted data, where the deghosted data are input with and without the assumption of horizontal acquisition. Comparison with numerical examples demonstrates that effective deghosting, that includes and accommodates the acquisition surface, is a prerequisite for free surface multiple elimination to deliver its capability.

The **third** looks at the subsequent effectiveness of depth imaging, that uses different free surface multiple elimination results from the second advance as input. Quantitative analysis is provided that defines the positive effect of accommodating acquisition topography in preprocessing steps on depth imaging results.

Contents

1 Introduction **1**

1.1 Background of seismic exploration 1

1.1.1 Seismic acquisition and events category 1

1.1.2 Seismic processing as a linked chain 5

1.2 Research motivation of this dissertation 10

1.2.1 Importance of preprocessing for subsequent processing 10

1.2.2 Challenges for preprocessing due to the complicated acquisition environment often found in the real world 11

1.3 Overview of the dissertation 13

2 Preprocessing for ISS multiple removal and Stolt CIII imaging **16**

2.1 Introduction 16

2.2 P_0/P_s separation and wavelet estimation 20

2.2.1 Theory 20

2.2.2 Accommodation of P_0/P_s separation for a non-horizontal measurement surface 26

2.2.3 1D analytic example 27

2.2.4 Numerical tests of both the impact and the accommodation of the topography of measurement surface 30

2.3 Source and receiver deghosting 36

2.3.1 Theory of receiver side deghosting 37

2.3.2 Theory of source side deghosting 40

2.3.3 Accommodation of deghosting for a non-horizontal measurement surface 40

2.3.4 1D analytic example 42

2.3.5 Numerical tests of both the impact and the accommodation of the topography of measurement surface 47

2.4 Conclusions 54

3 ISS free surface multiple elimination **55**

3.1 Introduction 55

3.2 Theory 56

3.2.1 Inverse scattering series 56

3.2.2 Task-specific inverse scattering sub-series 59

3.2.3 ISS free surface multiple elimination 60

3.3 1D analytic example 64

3.4 Numerical tests 65

3.5 Conclusions 68

4 Stolt CIII Imaging **70**

4.1 Theory 70

4.2 1D analytic example 74

4.3 Numerical tests 76

4.3.1 The impact of preprocessing that assumes horizontal measurement surface on Stolt CIII imaging 76

4.3.2 Results using preprocessing that accommodates the topography of the measurement surface 78

4.4 Discussions 81

4.5 Conclusions 85

5 Summary **86**

5.1 Conclusions 86

5.2 Future work 89

References **90**

Appendix A 2D Green's 2nd identity **97**

Appendix B Comparison Between Green's Theorem Wavefield Prediction Method and Convensional Elevation Static Correction Method **99**

List of Figures

1.1 Marine seismic experiment (Weglein et al., 2003). $*$ and ∇ indicate the source and receiver, respectively. The boat moves through the water towing the source and receiver arrays. The collection of different source-receiver wavefield measurements defines the seismic reflection data. 2

1.2 Seismic events (towed streamer acquisition). : direct wave, : reflection of direct wave from the free surface, : source ghost, : receiver ghost, : source-receiver ghost, : free surface multiple, : internal multiple, and : primary. 3

1.3 A chain of processing algorithms based on Green's theorem and the inverse scattering series (ISS) (Weglein, 2016b). 9

2.1 Green's second identity (Stolt and Weglein, 2012). Green's second identity provides a formula for computing a wavefield within a region from the value of the field and its normal derivative at all points on the region boundary. 22

2.2 (a) Actual medium and experiment, (b) reference medium, and (c) two sources overlaid on the reference medium. 23

2.3 The volume and output point r chosen in Green's theorem P_0/P_s separation. 24

2.4 Analytic example of Green's theorem P_0/P_s separation. Figures from left to right represent (1) direct wave, (2) reflection of direct wave from free surface, (3) primary from the water bottom, (4) receiver ghost, (5) source ghost, and (6) source-receiver ghost, respectively. 27

2.5 Velocity model and source position. 30

2.6 Total wave generated on different measurement surfaces (M.S.). (a) Horizontal M.S. at 50 m depth, and (b) undulated M.S. as shown by Figure 2.10. Colorbar on the right represents the amplitude. 31

2.7 Traceplot (offset=0m) of total wave (—) and different events (—) in Figure 2.6(a). **(a)** Direct wave, **(b)** reflection of direct wave from free surface, **(c)** primary and free surface multiple, **(d)** source ghosts, **(e)** receiver ghosts, and **(f)** source-receiver ghosts. 32

2.8 Separated P_0 wave using different measurement surface (M.S.) and/or different assumption of the measurement surface. **(a)** M.S. is horizontal, **(b)** M.S. has 0.1° inclination while P_0/P_s separation assumes it's horizontal, **(c)** M.S. has 1° inclination while P_0/P_s separation assumes it's horizontal, **(d)** M.S. has 2° inclination while P_0/P_s separation assumes it's horizontal, **(e)** M.S. is undulated while P_0/P_s separation assumes it's horizontal, and **(f)** M.S. is undulated and P_0/P_s separation accommodates its topography. Colorbar on the right represents the amplitude. 34

2.9 Wavelet estimation comparison using different measurement surface (M.S.) and/or different assumption of the measurement surface. **(a)** Actual wavelet (—) and wavelet estimated based on P_0 wave predicted at respectively 55 m depth (– – –), 65 m depth (– · –) and 90 m depth (· · · ·) , using actually horizontal M.S., **(b)** actual wavelet (—) and wavelet estimated respectively using predicted P_0 wave of Figure 2.8(b) (– – –), predicted P_0 wave of Figure 2.8(c) (– · · – – –) and predicted P_0 wave of Figure 2.8(d) (· · · ·), **(c)** actual wavelet (—) and wavelet estimated using predicted P_0 wave of Figure 2.8(e) (– – –) and predicted P_0 wave of Figure 2.8(f) (– · – ·). 35

2.10 Configuration of the undulated cable. Maximum depth is 75 m. Minimum depth is 25 m. 36

2.11 (a) Actual medium and experiment, (b) reference medium, and (c) three sources overlaid on the reference medium. 38

2.12 The volume and output point $\mathbf{r}_g$ in Green's theorem receiver side deghosting. 39

2.13 Different events of 1D analytic data for deghosting. 42

2.14 Velocity model and source position. 48

2.15 Data generated by the Cagniard-de Hoop method on different measurement surface (M.S.). **(a)** Horizontal M.S. at depth of 35 m, and **(b)** undulated M.S. with minimum depth of 25 m and maximum depth of 45 m. Colorbar on the right represents the amplitude. 49

2.16 Receiver deghosting result at 15 m depth. **(a)** M.S. is actually horizontal, **(b)** M.S. is 2° inclined, assuming it's horizontal in deghosting, **(c)** M.S. is undulated, assuming it's horizontal in deghosting, and **(d)** M.S. is undulated, with accommodation in deghosting. Colorbar on the right represents the amplitude. 50

2.17 Source deghosting result, using receiver deghosting results Figure 2.16 as input. **(a)** Using Figure 2.16(a) as input, **(b)** Figure 2.16(b) as input, **(c)** Figure 2.16(c) as input, and **(d)** Figure 2.16(d) as input. Colorbar on the right represents the amplitude. 51

2.18 Traceplot of source and receiver deghosting data predicted at 15 m depth. **(a)** Traceplot (offset=300 m) comparison of actual primary and free surface multiple (generated by the Cagniard-de Hoop method) at 15 m depth (▬), deghosted result (Figure 2.17(a)) using total wave generated on horizontal M.S. (—), deghosted result using total wave generated on 1° inclined M.S. assuming it's horizontal in deghosting (- - -) and deghosted result (Figure 2.17(b)) using total wave generated on 2° inclined M.S. assuming it's horizontal in deghosting (- · · · - -), and **(b)** traceplot (offset=300 m) comparison of deghosted result (Figure 2.17(a)) using total wave generated on horizontal M.S. (—), deghosted result (Figure 2.17(c)) using total wave generated on undulated M.S. assuming it's horizontal in deghosting (- - -) and deghosted result (Figure 2.17(d)) using total wave generated on undulated M.S. with accommodation of the M.S.'s topography in deghosting (- · - · -). 52

3.1 (a) Actual medium and experiment, (b) reference medium of half water and half air, and (c) reference Green's function $G_0 = G_0^d + G_0^{FS}$ which is a direct term plus a free surface reflected term. 60

3.2 Predicted free surface multiple (FSM) (left) using Figure 2.17 as input and primary (right) after subtracting the predicted FSM from Figure 2.17. **(a)** Predicted FSM from deghosted data Figure 2.17(a), **(b)** subtraction of Figure 3.2(a) from Figure 2.17(a), **(c)** predicted FSM from deghosted data Figure 2.17(b), **(d)** subtraction of Figure 3.2(c) from Figure 2.17(b), **(e)** predicted FSM. from deghosted data Figure 2.17(c), and **(f)** subtraction of Figure 3.2(e) from Figure 2.17(c). Colorbar on the right represents the amplitude. 66

3.3 Comparison of deghosted data (Figure 2.17(a)) at 15 m depth (▬), actual FSM (generated by the Cagniard-de Hoop method) at 15 m depth (- - -), predicted FSM (Figure 3.2(a)) using the deghosted result of total wave generated on horizontal M.S. (—), predicted FSM using the deghosted result of total wave generated on 1° M.S. while assuming it's horizontal in deghosting(· · · · ·) and predicted FSM (Figure 3.2(c)) using the deghosted result of total wave generated on 2° M.S. while assuming it's horizontal in deghosting (· - · -). 67

3.4 **(a)** Predicted free surface multiple (FSM) from deghosted data Figure 2.17(d), and **(b)** subtraction of Figure 3.4(a) from Figure 2.17(d). Colorbar on the right represents the amplitude. 68

3.5 Comparison of deghosted data (Figure 2.17(a)) at 15 m depth (▬), predicted FSM (Figure 3.2(a)) using the deghosted result of total wave generated on horizontal M.S. (—), predicted FSM (Figure 3.2(e)) using the deghosted result of total wave generated on undulated M.S. while assuming it's horizontal in deghosting (- - -), and predicted FSM (Figure 3.4(a)) using the deghosted result of total wave generated on undulated M.S. with accommodation of its topography in deghosting (· - · -). 69

4.1 Predict P in the volume for (a) general waves and (b) one-way propagating waves from only measurements on S_U use $G_0 = G_0^-$ (Stolt and Weglein, 2012). 72

4.2 Principle of Green's theorem wavefield prediction. 73

4.3 Depth imaging results. **(a)** Imaging using predicted primary Figure 3.2(b) as input, **(b)** imaging using predicted primary Figure 3.2(d) as input, and **(c)** imaging using predicted primary Figure 3.2(f) as input. Colorbar on the right represents the amplitude. 77

4.4 Traceplot ($x_m = 0$ m) comparison of imaging result Figure 4.3(a) (—) with horizontal M.S., imaging result with 1° inclined M.S. assuming it's horizontal in deghosting (- - -) and Figure 4.3(b) (- · -) with 2° inclined M.S. assuming it's horizontal in deghosting. 78

4.5 Imaging result using predicted primary Figure 3.4(b) as input. Colorbar on the right represents the amplitude. 79

4.6 (a) Traceplot ($x_m = 0$ m) comparison of Figure 4.3(a) (—), Figure 4.3(c) (- - -) and Figure 4.5 (- · -) and (b) zoomed view of the red box in (a). 80

4.7 Velocity model. Two layers are half-space. 82

4.8 (a) Horizontal acquisition, and (b) undulated acquisition. 83

4.9 Input data (primary only) for imaging. (a) horizontal acquisition, and (b) undulated acquisition. Colorbar on the right represents the amplitude. 83

4.10 Imaging result with horizontal acquisition (Figure 4.9(a)). Colorbar on the right represents the amplitude. 84

4.11 Imaging result with undulated acquisition (Figure 4.9(b)). The undulated acquisition is assumed horizontal in migration. Colorbar on the right represents the amplitude. 84

B.1 The acoustic model that generate the data for comparison. 101

B.2 The trace comparison between the input data (black solid line), static shift result (blue dashed line), Green's theorem prediction result (red solid line), and the analytic result (green dashed line) at offset 80 m. 102

B.3 The trace comparison between the input data (black solid line), static shift result (blue dashed line), Green's theorem prediction result (red solid line), and the analytic result (green dashed line) at offset 3200 m. 102

B.4 The acoustic model used to generate the data for the second example. 103

B.5 The acquisition surface in the second example. 103

B.6 The input data. Colorbar on the right represents the amplitude. . . . 104

B.7 Prediction result by elevation static correction at depth 30 m. Colorbar on the right represents the amplitude. 105

B.8 Prediction result by Green's theorem wavefield prediction at depth 30 m. Colorbar on the right represents the amplitude. 105

B.9 Trace comparison between the perfect result generated analytically at depth 30 m (blue solid line), the prediction by Green's theorem wavefield prediction method (red dashed line), and the prediction by elevation static correction method (black dashed line) at different offsets. 106

List of Tables

1.1 Four numerical cases of preprocessing in Chapter 2. 14

5.1 Effectiveness of three steps in four numerical cases. 88

Chapter 1

Introduction

1.1 Background of seismic exploration

The goal of exploration seismology is to study and illuminate the subsurface, and thereby locate, delineate and monitor potential underground hydrocarbon reservoirs. The objective of seismic research is to provide new capabilities to the seismic exploration toolbox, so as to increase our capability to locate hydrocarbons.

1.1.1 Seismic acquisition and events category

In a seismic exploration procedure, a man-made source of seismic energy generates seismic waves that propagate through the subsurface. After encountering an interface with rapidly changing physical properties (like velocity and/or density), a portion of the propagating wave gets reflected back to the earth's surface where it is recorded by receivers and constitutes seismic data. Figure 1.1 shows a cartoon of a typical towed streamer acquisition in the marine setting, where the source and receiver are airguns and hydrophones, respectively.

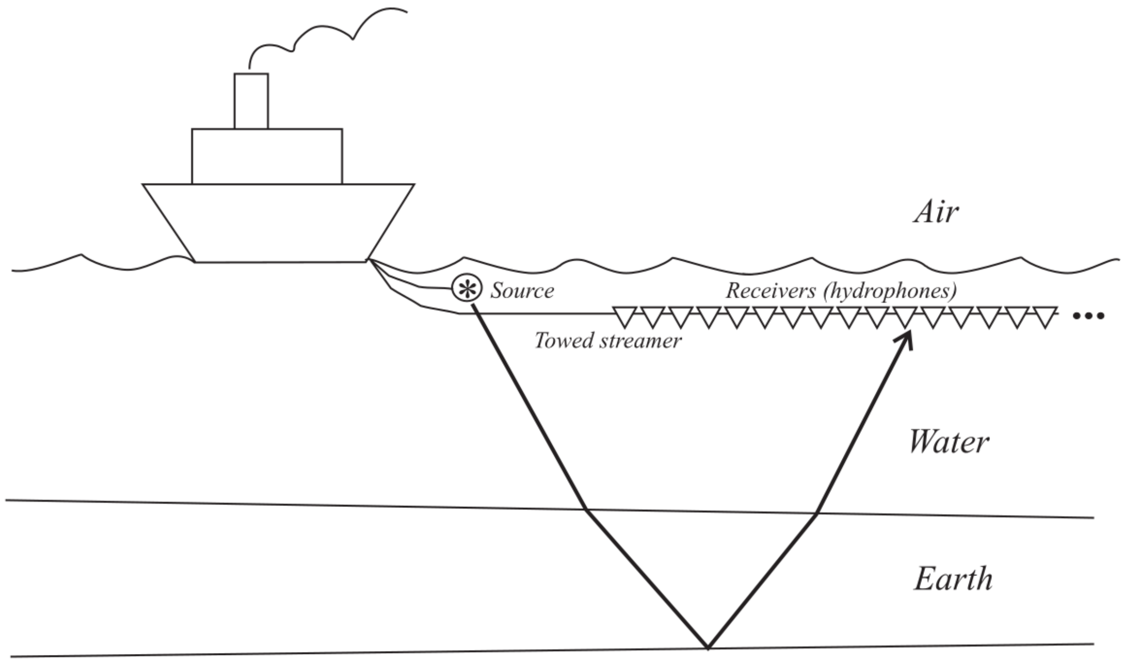

Figure 1.1: Marine seismic experiment (Weglein et al., 2003). $*$ and ∇ indicate the source and receiver, respectively. The boat moves through the water towing the source and receiver arrays. The collection of different source-receiver wavefield measurements defines the seismic reflection data.

A seismic event refers to a distinct arrival of seismic energy (Weglein et al., 2003). For the towed streamer acquisition (Figure 1.1), events are illustrated by Figure 1.2. Below is a categorization of seismic event definition (Weglein et al., 2003) depending on their history for the marine towed streamer acquisition.

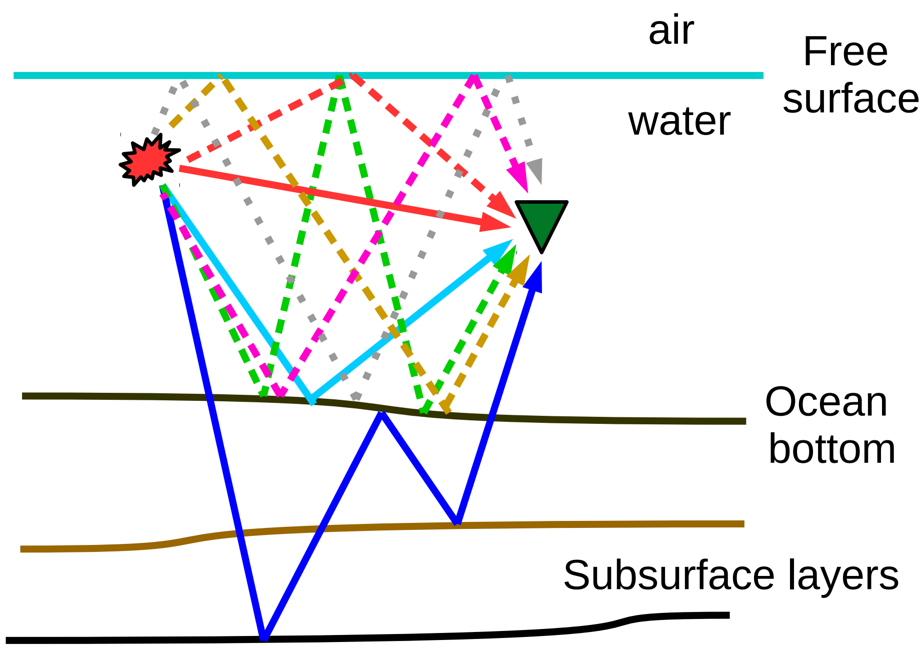

Figure 1.2: Seismic events (towed streamer acquisition). — : direct wave, - - - : reflection of direct wave from the free surface, - - - : source ghost, - - - : receiver ghost, · · · : source-receiver ghost, - - - : free surface multiple, — : internal multiple, and — : primary.

Reference wave. Both the Green's theorem method and inverse scattering series (ISS) method (which will be studied in this dissertation) start from perturbation theory. Perturbation theory separates the actual medium into a reference medium plus a perturbation. The choice of a reference medium depends on the specific seismic objective and application. The waves that propagate in the reference medium are called reference waves (P_0 waves). The waves that travel in the actual medium are called total waves. The difference between the total and reference waves is defined as the scattered wave (P_s waves).

For marine acquisition, if the reference medium is chosen to be a half-space of air over a half-space of water, the reference wave contains a direct wave and a wave that first travels up to the free surface and then down to the receiver. The reference wave does not experience the subsurface; hence, it does not carry any subsurface information and needs to be removed. All other events experience the subsurface and are divided below.

Ghost. Ghost begins its propagation history by traveling up from the source to the free surface (called **source ghost**) or ends its history by traveling down from the free surface to the receiver (called **receiver ghost**) or does both (called **source-receiver ghost**).

After reference waves and ghosts are removed, the remaining waves that begin their history by going downward from the source and end their history by going upward to the receiver are further divided, depending on the number of upward reflections in their history:

Primary. Primary has only one upward reflection in its entire propagation history.

Multiple. Multiple experiences more than one upward reflection in its history. Depending on the location of downward reflection between two consecutive upward reflections, multiple is further classified as free surface multiple and internal multiple. Multiples that have at least one downward reflection at the free surface are called free surface multiples, whereas multiples that have all of their downward reflections below the free surface are called internal multiples. The order of a free surface multiple is determined by the total number of downward reflections at the free surface. In contrast, the order of an internal multiple is defined by the total number of the downward reflections that it has experienced from any subsurface reflectors (Weglein et al., 1997).

Notice that, these definitions of different event types follow a sequence. The above separation of seismic data into different kinds of events is important because only primary events are used in seismic imaging and inversion for physical properties. This is explained in next subsection. All events other than primary events must be identified and removed from seismic data.

1.1.2 Seismic processing as a linked chain

After seismic data acquisition, the next step is to find petroleum reservoirs using the subsurface information carried by the recorded seismic data. Petroleum reservoirs are usually located in structural traps[1]. A structural mapping of subsurface reflectors helps locate those traps and develops an estimation of how properties (such as velocity and density) change across the subsurface reflectors, which in turn helps to locate and delineate oil or natural gas reservoirs. Hence, the subsurface information that the industry wants to obtain from seismic data includes, e.g., where the reflectors are located in the subsurface and how the earth's mechanical properties change across those reflectors. The process to locate the subsurface reflectors is called **imaging**,

[1]In petroleum geology, a structural trap is a type of geological trap that forms as a result of changes in the structure of the subsurface, due to tectonic, diapiric, gravitational and compactional processes. These changes block the upward migration of hydrocarbons and can lead to the formation of a petroleum reservoir (Wikipedia).

and the process to estimate the change in mechanical properties across the reflectors is called **inversion**.

Seismic migration methods that use wave theory for seismic imaging have two components: (1) a wave propagation model, and (2) an imaging condition. For the imaging principle a good reference to start with is Jon Claerbout's 1971 landmark contribution (Claerbout, 1971). He listed three imaging principles. The first imaging principle is exploding-reflector model which is for stacked or zero offset data[2]. This is called Claerbout imaging principle I. The second imaging principle is the time space coincidence of up and downgoing waves (Claerbout II). Waves propagate down from the source, are incident on the reflector and the reflector then generates a reflected up-going wave. According to Claerbout II (CII), the reflector exists at the location in space where the wave that is downward propagating from the source and the up wave from the reflector are at the same time and space. Based on this principle, the reverse time migration method was proposed (e.g., Claerbout, 1971; Whitmore, 1983; Baysal et al., 1983; McMechan, 1983), which is used a lot today by the petroleum industry.

Claerbout III (CIII) imaging starts with surface source and receiver data, and predicts what a source and receiver would record inside the earth. The CIII imaging principle then arranges the predicted source and receiver to be coincident and asks for $t = 0$. If the predicted coincident source and receiver experiment at depth is proximal to a reflector you get a non-zero result at time equals zero. You get a direct

[2]Offset is the distance from the source point to the center of a geophone group. Unless a particular geophone group is specified, the distance to the nearest geophone group center is implied; sometimes the distance is to an individual geophone (Sheriff, 2002).

and definitive yes or no at every subsurface point. This imaging principle leads to a new and first migration (Weglein et al., 2016; Weglein, 2016a) that is **equally effective at the target and/or the reservoir**.

While these three imaging conditions give exactly the same result for a normal incident spike plane wave on a single horizontal reflector, Claerbout II and III are of central industry interest today. This is because we currently process pre-stacked data. And imaging condition II and III will produce different results for a separated source and receiver located in a homogeneous half space above a single horizontal reflector.

In seismic migration methods based on aforementioned imaging principles, a velocity model is required as input[3]. In practice, a smooth and continuous velocity is generally assumed. When a smooth and continuous velocity is used, only primaries are required to locate reflectors, while other events, such as multiples, result in false images of reflectors in imaging methods based on both imaging principles[4] (Weglein, 2016a); therefore, events except for primaries need to be removed[5] from the seismic data before inputting the seismic data to imaging and inversion algorithms to locate the reflectors and estimate the change in properties across those reflectors.

To separate the primaries from recorded seismic data, the removal of reference

[3]The ISS provides an ISS imaging algorithm (e.g., Weglein et al., 2003; Shaw, 2005) that does not require any subsurface information, such as velocity information.

[4]In fact, when an accurate discontinuous velocity model is used, only primaries contribute to migration with the same image and inversion results are independent of whether multiples are kept or removed (Weglein, 2016a).

[5]However, it should be mentioned that reference wave can be utilized to estimate the source wavelet (Weglein and Secrest, 1990). A wavelet is used to describe a short time series which can be used to represent, for example, the source characteristics.

wave, ghosts and multiples is usually achieved in stages. Figure 1.3 shows a seismic processing chain based on two fundamental mathematical physics tools: Green's theorem and inverse scatting series (ISS). The stages/links include

1. Separation of reference wave and scattered wave and wavelet estimation

(e.g., Weglein and Secrest, 1990)

2. Deghosting

(e.g., Weglein et al., 2002; Zhang and Weglein, 2005, 2006)

3. Free surface multiple elimination

(e.g., Carvalho et al., 1992; Weglein et al., 1997, 2003)

4. Internal-multiple attenuation/elimination

(e.g., Araújo et al., 1994; Weglein et al., 1997, 2003)

5. Imaging

(e.g., Stolt and Weglein, 1985, 2012; Weglein et al., 2002, 2011a,b)

and inversion

(e.g., Weglein et al., 1981; Zhang, 2006; Zhang and Weglein, 2009a,b)

In this dissertation, step 1 and step 2 constitute preprocessing. The above seismic processing sequence is a linked chain of steps. The effectiveness of any given step not only depends on how well its own assumptions are satisfied, but also how well all the previous tasks in the chain have been achieved (Zhang, 2007). To date every step in this chain has progressed with increased effectiveness. Work will continue to make each processing step more capable and effective.

The Green's theorem preprocessing methods and ISS processing methods **do not** require any subsurface information and several algorithms are **independent** of earth model type. Notice that these methods require knowledge of the seismic experiment, including, for example, the topography of the acquisition surface.

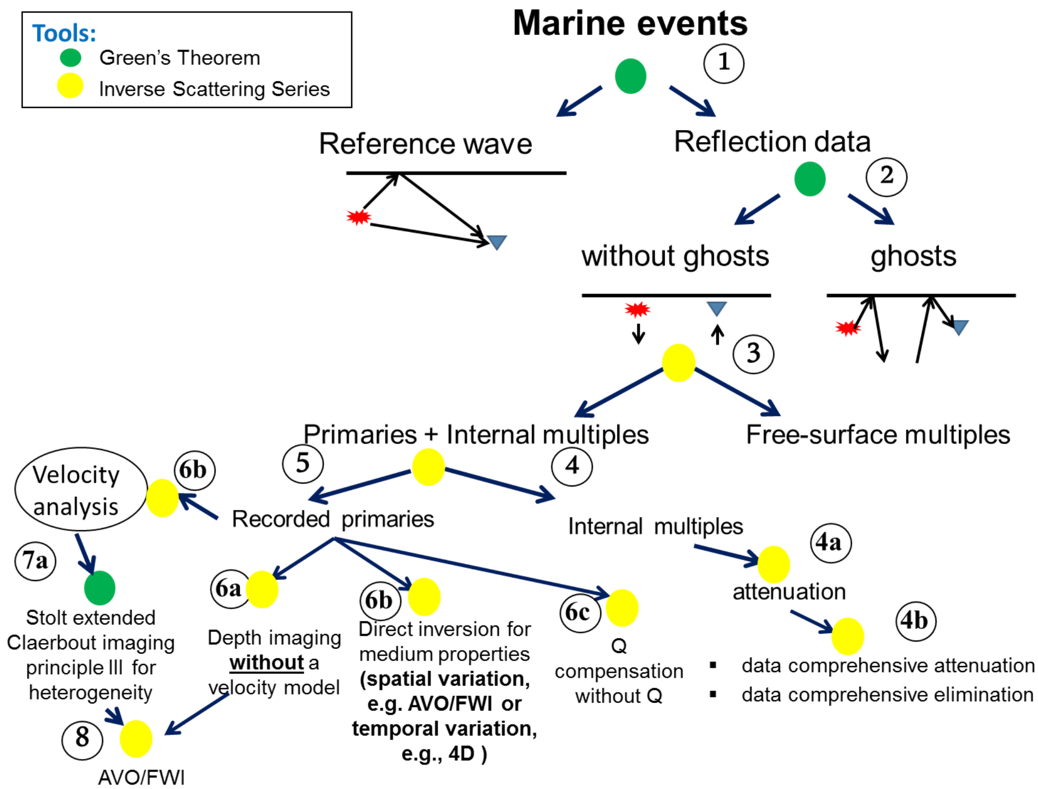

Figure 1.3: A chain of processing algorithms based on Green's theorem and the inverse scattering series (ISS) (Weglein, 2016b).

1.2 Research motivation of this dissertation

1.2.1 Importance of preprocessing for subsequent processing

As mentioned above, to separate primaries for mapping the subsurface, preprocessing and multiple elimination have to be effectively achieved. Weglein et al. (2003) described how every ISS isolated-task subseries requires (1) the removal of the reference wave, (2) an estimate of the source signature and radiation pattern, and (3) source and receiver deghosting. Weglein et al. (2003) also described how the ISS has a nonlinear dependence on these preprocessing steps.

The first step in preprocessing, as we can see from Figure 1.3, is separation of reference wave (P_0 wave) and scattered wave (P_s wave). This step is important because the separated P_s wave contains subsurface information, which is the input for subsequent steps. Meanwhile, the P_0 wave contains (and can provide) the information about the source wavelet, which is essential information in many processing steps.

The second step in preprocessing is deghosting - to remove the ghosts in the separated P_s wave. Actually, deghosting has been a long-standing seismic objective and problem (Amundsen, 1993; Robinson and Treitel, 2008). Accounting for the amplitude and phase distortions caused by the so-called ghost effect was first studied in the context of sources by Van Melle and Weatherburn (1953). Through deghosting, seismic resolution can be enhanced by removing spectrum notches and boosting low frequencies. In addition, deghosting is a prerequisite for free surface and internal-multiple removal as well as for the resolution and delineation of imaged-inverted primaries (Weglein et al., 2002).

1.2.2 Challenges for preprocessing due to the complicated acquisition environment often found in the real world

As we see, preprocessing is important for seismic exploration. However, in the real world, the effectiveness of preprocessing could be influenced by many factors. As shown by Figure 1.1, the character of recorded seismic data is affected by (1) the source that generates the wave, (2) the properties of the medium that waves have experienced, and (3) the nature of the acquisition system. That means that an accurate description of the seismic experiment has to be incorporated into seismic data processing. In the real world, the acquisition surface is generally non-horizontal and may be far from horizontal in off-shore and on-shore environments. However, there are times when people assume horizontal acquisition, for example by using a P-Vz deghosting method (Amundsen, 1993) that assume horizontal acquisition. Hence, the **first** progress I want to achieve in this dissertation is to study the impact of the topography of the acquisition on preprocessing and a solution and algorithm that accommodates a non-horizontal acquisition.

The **second** progress I want to achieve in this dissertation is to observe the consequence in subsequent processing tasks resulting from ignoring the topography of the measurement surface in preprocessing. This is an issue because some subsequent processing methods assume that their input data are collected at a constant depth.

And the effectiveness of processing steps is dependent on the effectiveness of preprocessing. Examples of processing steps are the ISS free surface multiple elimination and Stolt CIII imaging that this dissertation focuses on. As numerical examples in Chapter 3 and Chapter 4 will demonstrate, the consequence of ignoring the acquisition topography in preprocessing can often be severe. In those cases, such adverse consequence needs to be resolved, so that subsequent seismic processing tasks can have their prerequisites satisfied and retain their capability.

To do that, it is important to incorporate the topography of measurement surface in preprocessing. In fact, as pointed out by Weglein et al. (2013) and Mayhan and Weglein (2013), preprocessing methods derived from the Green's theorem are wave-theoretic algorithms that can be defined in the frequency-space domain, and in principle can succeed with measurement surfaces of any shape. **It is a wave-theoretic method and different from the conventional static correction or shift (Yilmaz, 2001)**[6] . The theory of Green's theorem and Green's theorem derived seismic methods will be explained in detail in Chapter 2 and Chapter 4. The theory of inverse scattering series (ISS) and the ISS multiple elimination method will be provided in Chapter 3.

[6]Appendix B will shown a simple numerical example that compares static shift and Green's theorem methods.

1.3 Overview of the dissertation

This dissertation studies the impact of the topography of the acquisition surface on preprocessing and the subsequent free surface multiple elimination and depth migration. Consequences of ignoring the topography of acquisition surface are examined and an algorithm response to fix that problem is provided. The preprocessing algorithm that accommodates non-horizontal acquisition is described; this allows subsequent multiple removal and imaging to deliver their promise and potential.

Chapter 1 provides a brief introduction to seismic exploration. The motivation behind research in this dissertation is described: to define and address an important practical challenge for preprocessing and subsequent processing and interpretation.

Chapter 2 first introduces the theory behind Green's theorem preprocessing methods (P_0/P_s separation and deghosting), followed by an analytic example for each preprocessing task. Based on the fundamental formula of Weglein and Secrest (1990) and Weglein et al. (2002), a P_0/P_s algorithm and a deghosting method for non-horizontal acquisition are derived, respectively. To study the impact of the topography of acquisition surface, four cases of numerical tests are carried out as shown in Table 1.1, using a same velocity model. The first three cases have different measurement surfaces that are (1) horizontal, (2) inclined, and (3) undulating, respectively. In the first three cases studied, the measurement surface is assumed to be horizontal. We then observe artifacts in preprocessing due to this assumption. To address this issue, a fourth set of tests was carried out. It considers the undulated measurement surface case but carries out the preprocessing steps with the derived new formula that accommodates the topography of the measurement surface.

Case	Actual acquisition	Assumption about acquisition
1	Horizontal	Horizontal
2	Inclined (2 degree)	Horizontal
3	Undulated	Horizontal
4	Undulated	No assumption. The topography is accommodated

Table 1.1: Four numerical cases of preprocessing in Chapter 2.

Chapter 3 focuses on the effectiveness of ISS free surface multiple elimination, using the preprocessing results in Chapter 2. This chapter first introduces the algorithm of free surface multiple elimination based on task-specific inverse scattering sub-series. Then four numerical examples of free surface multiple removal are shown, where each uses the deghosted data, respectively, from the four cases of numerical examples shown by Table 1.1.

Chapter 4 focuses on the influence of the topography of measurement surface on depth imaging, which uses data that have gone through preprocessing and multiple elimination. The imaging method used here is the Stolt CIII imaging (Weglein et al., 2016; Weglein, 2016a), a new imaging method that treats all frequencies in the input data with equal effectiveness. First, the theory of Green's theorem wavefield prediction and Claerbout III imaging condition is briefly explained. To study the impact of the topography of acquisition surface on the final imaging, four numerical tests are done, using the four numerical results of free surface multiple elimination in Chapter 3 as input.

Chapter 5 provides the summary of this dissertation as well as future work to be done.

Chapter 2

Preprocessing for ISS multiple removal and Stolt CIII imaging

2.1 Introduction

Green's theorem can offer a number of useful algorithms that concern the broad field of seismic exploration (e.g., deghosting, wavelet estimation, wavefield prediction), by choosing reference medium for certain objectives.

As we know, the first step in preprocessing, which is very important for subsequent seismic tasks, is separation of reference wave (P_0) and scattered wave (P_s) and source signature estimation. Weglein and Secrest (1988, 1990) proposed a general wave theoretic P_0/P_s separation and wavelet estimation method through comparing the Lippmann-Schwinger equation and Green's theorem, given a cable (or in 3D, a surface) where both the pressure and its normal derivative are measured. Tests were done by Keho et al. (1990). To remove the need of normal derivative, Weglein et al. (2000) and Guo et al. (2005) developed P_0/P_s wave separation and source wavelet estimation algorithms that requires only the pressure on one cable, by means of Green's theorem wavefield prediction. Zhang (2007) summarized these wavefield separation and prediction algorithms and discussed their assumptions, limitations, and advantages. The P_0/P_s separation and wavelet estimation methods mentioned above are in (x-ω) domain, where the P_0 or P_s wave is predicted either below or above the M.S.. For on-shore exploration, Tang and Weglein (2014) proposed the algorithm of wavelet estimation based on P_0/P_s separation on exactly the cable in (k,ω) domain.

The second step in preprocessing is deghosting. Deghosting is a long-standing seismic objective and problem (Amundsen, 1993; Robinson and Treitel, 2008). It removes downgoing events of the recorded field (receiver ghost) and events first going up from source to air-water boundary (source ghost). Seismic resolution can be enhanced by removing spectrum notches and boosting low frequencies. Also, deghosting has risen in importance as prerequisites for free surface and internal-multiple removal as well as for the resolution and delineation of imaged-inverted primaries (Weglein et al., 2002).

The problem of accounting for the amplitude and phase distortions introduced by the so-called ghost effect was first studied in the context of sources by Van Melle and Weatherburn (1953). They showed that by using more than one source with a delayed firing pattern, it was possible to mitigate the ghost effect. Based on this, different acquisition techniques were proposed to achieve deghosting. These techniques include over/under streamers (Snneland et al., 2005; Posthumus, 1993; Moldoveanu et al., 2007; Özdemir et al., 2008), ocean-bottom cable (OBC) (Barr and Sanders, 2005), hydrophone plus geophone (Carlson et al., 2007) and multi-component towed-streamers (Robertsson et al., 2008; Vassallo et al., 2013). Other researchers started from signal characteristics of ghosts and designed specialized acquisition like single linearly slanted (Ray and Moore, 1982; Dragoset Jr, 1991) or depth-variable streamer (Soubaras, 2010).

Motivated by progress in acquisition, different deghosting theories have developed. A more general and physically complete method of deghosting was provided using Green's theorem. Weglein et al. (2002) and Zhang and Weglein (2005, 2006) first developed that methodology and it was tested successfully by Zhang (2007). The first test on field data was reported by Mayhan and Weglein (2013). Tang (2014) analyzed the impact of acquisition on deghosting. For on-shore preprocessing, Wu and Weglein (2015a,b, 2016a,b) derived elastic Green's theorem wavefield separation methods in pressure and displacement space, and extended and applied it to on-shore and ocean-bottom acquisition. Lin and Weglein (2016) studied the significance and impact of incorporating a 3D point source in Green's theorem deghosting. Zhang and Weglein (2016) studied 2D receiver deghosting in the space-frequency domain using a depth-variable tower streamer. The Green's theorem preprocessing methods are consistent with inverse scattering series (ISS) wave theory methods that do not require subsurface information (Weglein et al., 2003). As pointed out by Weglein et al. (2003), every ISS isolated-task subseries requires (1) the removal of the reference wavefield, (2) estimation of the source signature and radiation pattern, and (3) source and receiver deghosting, and the ISS has a nonlinear dependence on these preprocessing steps. Green's theorem can offer a number of useful algorithms (see e.g., Zhang (2007); Mayhan (2013)) by choosing different reference medium to achieve different objectives (e.g., deghosting or P_0/P_s separation).

As pointed out by Weglein et al. (2013) and Mayhan and Weglein (2013), deghosting methods derived from the Green's theorem are wave-theoretic algorithms that can be defined in the frequency-space domain, and in principle can succeed with cables of any shape (e.g., slanted). The main purpose of including a nonhorizontal measurement surface (M.S.) equation is to accommodate on-shore and ocean-bottom acquisition where deviation from horizontal acquisition can frequently occur. Therefore, based on Weglein et al. (2002), Zhang (2007) and Zhang and Weglein (2016), we derive a 3D source and receiver deghosting formula in the space-frequency domain for a depth-variable M.S., assuming the topography of M.S. is known. In numerical examples, we test the impact of assuming a horizontal M.S (when M.S. is not actually horizontal) on deghosting and accommodation of a nonhorizontal M.S. using the new depth-variable cable formula.

2.2 P_0/P_s separation and wavelet estimation

2.2.1 Theory

Green's theorem can find its root in the fundamental theorem of integral calculus. The fundamental theorem of integral calculus expresses the value of a definite integral of a given integrable function f over an interval, as the difference between the values of the function f's antiderivative F at the endpoints of the interval,

$$\int_a^b f(x)dx = F(b) - F(a) \tag{2.1}$$

where $F'(x) = f(x)$. This is a fundamental tool to solve problems within a restricted region or interval. The multidimensional extension of this theorem is divergence theorem (also called Gauss's theorem)

$$\int_V (\nabla \cdot \mathbf{A}) d\mathbf{r'} = \oint_S \mathbf{A} \cdot \hat{\mathbf{n}} \, dS \tag{2.2}$$

where V is a volume enclosed by a surface S. $\mathbf{A}$ is a continuously differentiable vector field defined on V. Physically, the divergence theorem relates the normal outflow of a vector field through a closed surface to the volume integration of the divergence of that field. Choosing $\mathbf{A} = \phi\nabla\psi - \psi\nabla\phi$, where ϕ and ψ are both twice continously differentiable on the volume V, there is Green's theorem (also called the Green's second identity)

$$\int_V (\phi\nabla^2\psi - \psi\nabla^2\phi) d\mathbf{r} = \oint_S (\phi\nabla\psi - \psi\nabla\phi) \cdot \hat{\mathbf{n}} \, dS \tag{2.3}$$

Suppose two wavefields in the $(\mathbf{r}, \omega)$ domain P and G_0 satisfy

$$(\nabla^2 + k^2)P(\mathbf{r}; \omega) = \rho(\mathbf{r}; \omega) \tag{2.4}$$

$$(\nabla^2 + k^2)G_0(\mathbf{r}, \mathbf{r}'; \omega) = \delta(\mathbf{r} - \mathbf{r}') \tag{2.5}$$

where ρ is a general source, i.e., it represents both active sources (air guns, dynamite, vibrator trucks) and passive sources (heterogeneities in the earth). If we replace ϕ by P, replace ψ by G_0 and substitute $\nabla'^2 P(\mathbf{r}'; \omega) = \rho(\mathbf{r}'; \omega) - k^2 P(\mathbf{r}'; \omega)$ and $\nabla'^2 G_0(\mathbf{r}', \mathbf{r}; \omega) = \delta(\mathbf{r}' - \mathbf{r}) - k^2 G_0(\mathbf{r}', \mathbf{r}; \omega)$ into Equation (2.6), we have

$$\begin{aligned}
&\int_V \Big[P(\mathbf{r}'; \omega)\nabla'^2 G_0(\mathbf{r}', \mathbf{r}; \omega) - G_0(\mathbf{r}', \mathbf{r}; \omega)\nabla'^2 P(\mathbf{r}'; \omega) \Big] d\mathbf{r}' \\
&= \oint_S \Big[P(\mathbf{r}'; \omega)\nabla' G_0(\mathbf{r}', \mathbf{r}; \omega) - G_0(\mathbf{r}', \mathbf{r}; \omega)\nabla' P(\mathbf{r}'; \omega) \Big] \cdot d\mathbf{S}'
\end{aligned} \tag{2.6}$$

Further we have

$$\begin{aligned}
&\int_V P(\mathbf{r}'; \omega)\delta(\mathbf{r}' - \mathbf{r}) d\mathbf{r}' \\
&= \begin{cases} P(\mathbf{r}; \omega), & \mathbf{r} \ \textit{inside} \ V \\ 0, & \mathbf{r} \ \textit{outside} \ V \end{cases} \\
&= \int_V \rho(\mathbf{r}'; \omega) G_0(\mathbf{r}', \mathbf{r}; \omega) d\mathbf{r}' + \oint_S \Big[P(\mathbf{r}'; \omega)\nabla' G_0(\mathbf{r}', \mathbf{r}; \omega) - G_0(\mathbf{r}', \mathbf{r}; \omega)\nabla' P(\mathbf{r}'; \omega) \Big] \cdot d\mathbf{S}'
\end{aligned} \tag{2.7}$$

As shown by Figure 2.1, Equation (2.7) provides a solution P to Equation (2.4) inside the volume V, with any Green's function G_0 that satisfies Equation (2.5). Please notice that for $\mathbf{r}$ outside V, it does **not** mean the physical P is zero. Physically, Equation (2.7) provides a relationship between the field inside volume and the measured field on the surface. As the following chapters of this dissertation will show theoretically, by choosing different reference medium, Green's theorem can perform different seismic processing tasks like P_0/P_s separation, deghosting, and wavefield prediction.

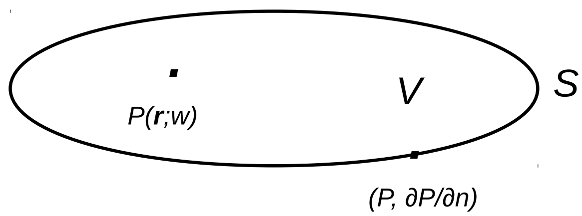

Figure 2.1: Green's second identity (Stolt and Weglein, 2012). Green's second identity provides a formula for computing a wavefield within a region from the value of the field and its normal derivative at all points on the region boundary.

Green's theorem derived seismic processing methods employ a model of the world that consists of a reference medium and sources (Weglein et al., 2003). If we choose the reference medium to be half space of air and half space of water (Figure 2.2(b)), whose property is the same as the actual medium (Figure 2.2(a)) along the measurement surface, the differences between the reference medium and the actual medium can be described as sources (Figure 2.2(c)) ρ, corresponding to the 'source' function or inhomogeneous driving force term(s) in a differential equation governing propagation in the reference medium. There are two sources required for the actual medium and experiment in Figure 2.2(a), using a reference medium in Figure 2.2(b). These two sources are the airgun ρ_{airgun}, and the earth perturbation ρ_{earth}, respectively, and $\rho = \rho_{airgun} + \rho_{earth}$.

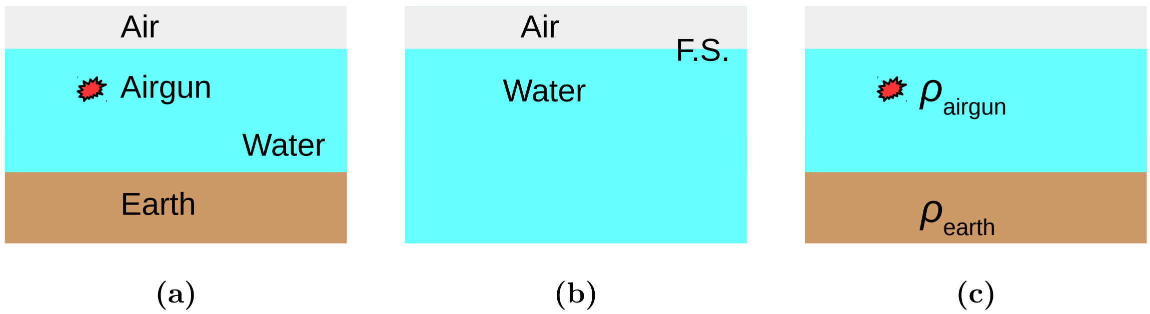

Figure 2.2: (a) Actual medium and experiment, (b) reference medium, and (c) two sources overlaid on the reference medium.

According to the Lippmann-Schwinger equation, the total wavefield at a location $\mathbf{r}$ can be expressed as,

$$\begin{aligned} P(\mathbf{r};\omega) &= \int_{\infty} \rho(\mathbf{r}')G_0(\mathbf{r},\mathbf{r}';\omega)d\mathbf{r}' \\ &= \int_{\infty} \rho_{airgun}(\mathbf{r}')G_0 d\mathbf{r}' + \int_{\infty} \rho_{earth}(\mathbf{r}')G_0 d\mathbf{r}' \end{aligned} \tag{2.8}$$

Here $G_0(\mathbf{r},\mathbf{r}';\omega)$ is a causal Green's function for the reference medium of half air and half water. $G_0(\mathbf{r},\mathbf{r}_s,\omega) = G_0^d(\mathbf{r},\mathbf{r}_s,\omega) + G_0^{FS}(\mathbf{r},\mathbf{r}_s,\omega)$. Here $G_0^d(\mathbf{r},\mathbf{r}_s,\omega) = (-1/4\pi)exp(ikR_+)/R_+$ is the causal whole space Green's function, $k = \omega/c_0$, and $R_+ = |\mathbf{r}-\mathbf{r}_s|$. $G_0^{FS}(\mathbf{r},\mathbf{r}_s,\omega) = (-1/4\pi)exp(ikR_-)/R_-$, where $R_- = |\mathbf{r}-\mathbf{r}_{sI}|$ and $\mathbf{r}_{sI}$ is the mirror image of $\mathbf{r}_s$ with respect to the free surface.

Each of the two sources generates an outgoing wave (corresponding to the three terms of the right hand side of Equation (2.8)). Choose an enclosed volume V' that is bounded by surface S' (as shown by the dashed surface [- - -] in Figure 2.3) whose bottom surface is the measurement surface (M.S.) and whose top is the free surface. It was shown by Weglein and Secrest (1990) based on Green's theorem that at any location $\mathbf{r}$ outside V',

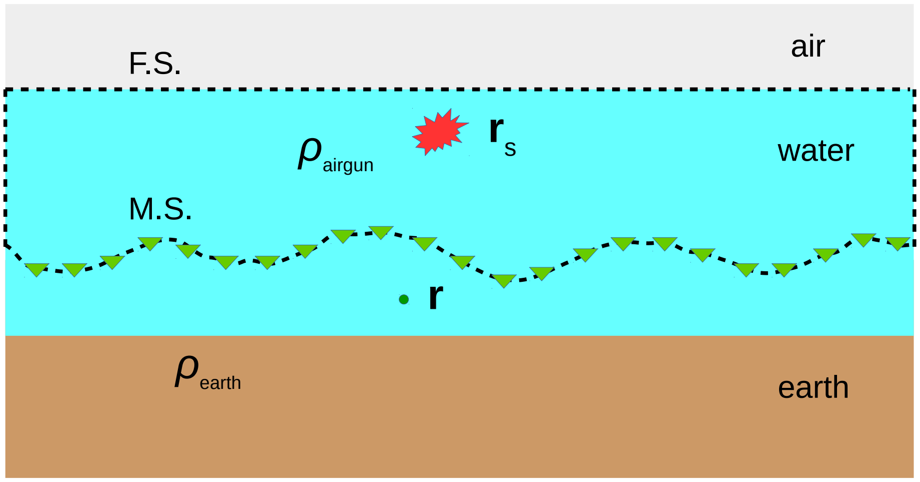

Figure 2.3: The volume and output point r chosen in Green's theorem P_0/P_s separation.

$$0 = \int_{V'} \rho(\mathbf{r}')G_0(\mathbf{r},\mathbf{r}';\omega)d\mathbf{r}' + \oint_{S'} \Big[P(\mathbf{r}';\omega)\nabla_{\mathbf{r}'}G_0(\mathbf{r},\mathbf{r}';\omega) - G_0(\mathbf{r},\mathbf{r}';\omega)\nabla_{\mathbf{r}'}P(\mathbf{r}';\omega)\Big] \cdot d\mathbf{S}' \tag{2.9}$$

This means the surface integral

$$\oint_{S'} \Big[P(\mathbf{r}';\omega)\nabla_{\mathbf{r}'}G_0(\mathbf{r},\mathbf{r}';\omega) - G_0(\mathbf{r},\mathbf{r}';\omega)\nabla_{\mathbf{r}'}P(\mathbf{r}';\omega)\Big] \cdot d\mathbf{S}' = -\int_{V'} \rho(\mathbf{r}')G_0(\mathbf{r},\mathbf{r}';\omega)d\mathbf{r}' \tag{2.10}$$

represents the contribution to the wavefield at any location $\mathbf{r}$ outside the volume V', due to sources inside the volume V', except a minus sign. Here $d\mathbf{S}'$ is the surface element of S' at $\mathbf{r}'$ whose direction is outwards normal to S'. Since the chosen volume V' encloses the airgun, the inside contribution only comes from ρ_{airgun}. At any point, $\mathbf{r}$, beneath $M.S.$, the integral in Equation (2.10) gives the opposite of the contribution of the total field due to the source ρ_{airgun}.

Therefore, we can achieve P_0/P_s separation at $\mathbf{r}$ (Weglein and Secrest, 1990),

$$P_0(\mathbf{r};\omega) = -\oint_{S'} \Big\{ P(\mathbf{r}';\omega)\nabla' G_0(\mathbf{r},\mathbf{r}';\omega) - G_0(\mathbf{r},\mathbf{r}';\omega)\nabla' P(\mathbf{r}';\omega) \Big\} \cdot d\mathbf{S}' \tag{2.11}$$

Here, P is input total field observed at $\mathbf{r}'$. Since both P and G_0 vanishes on the free surface, the RHS reduces to an integration on just the M.S.,

$$P_0(\mathbf{r};\omega) = -\int_{M.S.} \Big\{ P(\mathbf{r}';\omega)\nabla' G_0(\mathbf{r},\mathbf{r}';\omega) - G_0(\mathbf{r},\mathbf{r}';\omega)\nabla' P(\mathbf{r}';\omega) \Big\} \cdot d\mathbf{S}' \tag{2.12}$$

This is the P_0 wave predicted at $\mathbf{r}$. If the source $\rho_{airgun}(\mathbf{r}')$ is an isotropic point source $A(\omega)\delta(\mathbf{r}' - \mathbf{r}_s)$, from $P_0(\mathbf{r};\omega) = \int_\infty \rho_{airgun}(\mathbf{r}')G_0(\mathbf{r},\mathbf{r}';\omega)d\mathbf{r}'$ we can get $P_0(\mathbf{r};\omega) = A(\omega)G_0(\mathbf{r},\mathbf{r}_s;\omega)$. Then the source signature $A(\omega)$ can be estimated by the separated P_0 wave divided by the reference Green's function

$$A(\omega) = \frac{P_0(\mathbf{r};\omega)}{G_0(\mathbf{r},\mathbf{r}_s;\omega)} \tag{2.13}$$

For 2D the case, Equation (2.11) reduces to an integration over a closed line instead of closed surface,

$$\begin{aligned} &P_0(x,z;\omega) = \\ &-\oint_{l'} \Big\{ P(x',z';\omega)\nabla' G_0(x,z,x',z';\omega) - G_0(x,z,x',z';\omega)\nabla' P(x',z';\omega) \Big\} \cdot d\mathbf{l}' \end{aligned} \tag{2.14}$$

It can be derived from 2D Green's 2nd identity (Appendix A). Differently from the 3D case, 2D causal all space Green's function $G_0^d(\mathbf{r},\mathbf{r}_s,\omega) = -\frac{i}{4}H_0^{(1)}(kR_+)$ and $H_0^{(1)}$ is the zeroth order Hankel function of the first kind. Using the Sommerfeld radiation condition, Equation (2.12) reduces to

$$\begin{aligned} &P_0(x,z;\omega) = \\ &-\int_{m.l.} \Big\{ P(x',z';\omega)\nabla' G_0(x,z,x',z';\omega) - G_0(x,z,x',z';\omega)\nabla' P(x',z';\omega) \Big\} \cdot d\mathbf{l}' \end{aligned} \tag{2.15}$$

2.2.2 Accommodation of P_0/P_s separation for a non-horizontal measurement surface

When the measurement surface is horizontal, the gradient operator in Equation (2.12) becomes simply the derivative with respect to depth, and d**S**' becomes $dx'dy'$

$$
\begin{aligned}
&P_0(x, y, z, x_s, y_s, z_s; \omega) = \\
&-\int_{m.s.} \Big\{ P(x', y', z_g, x_s, y_s, z_s; \omega) \frac{d}{dz'} G_0(x, y, z, x', y', z'; \omega)\Big|_{z'=z_g} \\
&\qquad - G_0(x, y, z, x', y', z_g; \omega) \frac{d}{dz'} P(x', y', z', x_s, y_s, z_s; \omega)\Big|_{z'=z_g} \Big\} dx'dy'
\end{aligned}
\tag{2.16}
$$

When the measurement surface has some regular lateral variation in depth $z'(x', y')$, where z' is the depth function of coordinate x' and y', we can derive its normal vector $\mathbf{n} = (-\frac{1}{\Sigma}\frac{\partial z'(x',y')}{\partial x'}, -\frac{1}{\Sigma}\frac{\partial z'(x',y')}{\partial y'}, \frac{1}{\Sigma})$, where $\Sigma = \sqrt{1 + (\frac{\partial z'(x',y')}{\partial x'})^2 + (\frac{\partial z'(x',y')}{\partial y'})^2}$. So Equation (2.12) reduces becomes,

$$
\begin{aligned}
&P_0(x, y, z, x_s, y_s, z_s; \omega) = \\
&-\int_{m.s.} \Big\{ P(x', y', z', x_s, y_s, z_s; \omega)(-\frac{1}{\Sigma}\frac{\partial z'}{\partial x'}\frac{\partial}{\partial x'} - \frac{1}{\Sigma}\frac{\partial z'}{\partial y'}\frac{\partial}{\partial y'} + \frac{1}{\Sigma}\frac{\partial}{\partial z'}) \\
&G_0(x, y, z, x', y', z'; \omega) - G_0(x, y, z, x', y', z'; \omega)\frac{\partial}{\partial n'} P(x', y', z', x_s, y_s, z_s; \omega) \Big\} \Sigma\, dx'dy'
\end{aligned}
\tag{2.17}
$$

where $\frac{\partial}{\partial n'} P(x', y', z', x_s, y_s, z_s; \omega)$ is the normal derivative of $P(x', y', z', x_s, y_s, z_s, \omega)$ with respect to the cable.

Similarly, for the 2D case, Equation (2.15) further reduces to

$$
\begin{aligned}
P_0(x, z, x_s, z_s; \omega) = -\int_{m.l.} \Big\{ &P(x', z_g, x_s, z_s; \omega)\frac{d}{dz'} G_0(x, z, x', z'; \omega)\Big|_{z'=z_g} \\
&- G_0(x, z, x', z_g; \omega) \frac{d}{dz'} P(x', z', x_s, z_s; \omega)\Big|_{z'=z_g} \Big\} dx'
\end{aligned}
\tag{2.18}
$$

for a horizontal measurement line and

$$P_0(x,z,x_s,z_s;\omega) = \tag{2.19}$$

$$-\int_{m.l.}\Big[P(x',z',x_s,z_s;\omega)\big(-\frac{\frac{dz'(x')}{dx'}}{\sqrt{1+(\frac{dz'(x')}{dx'})^2}}\frac{\partial}{\partial x'}+\frac{1}{\sqrt{1+(\frac{dz'(x')}{dx'})^2}}\frac{\partial}{\partial z'}\big)$$

$$G_0(x,z,x',z';\omega)-G_0(x,z,x',z';\omega)\frac{\partial}{\partial n'}P(x',z',x_s,z_s;\omega)\Big]dx'\sqrt{1+(\frac{dz'(x')}{dx'})^2}$$

for a depth-variable measurement line.

2.2.3 1D analytic example

Assume the source is at z_s and the receiver is at $z_g(> z_s)$. As shown in Figure 2.4, total wave at z_g consists of (from left to right),

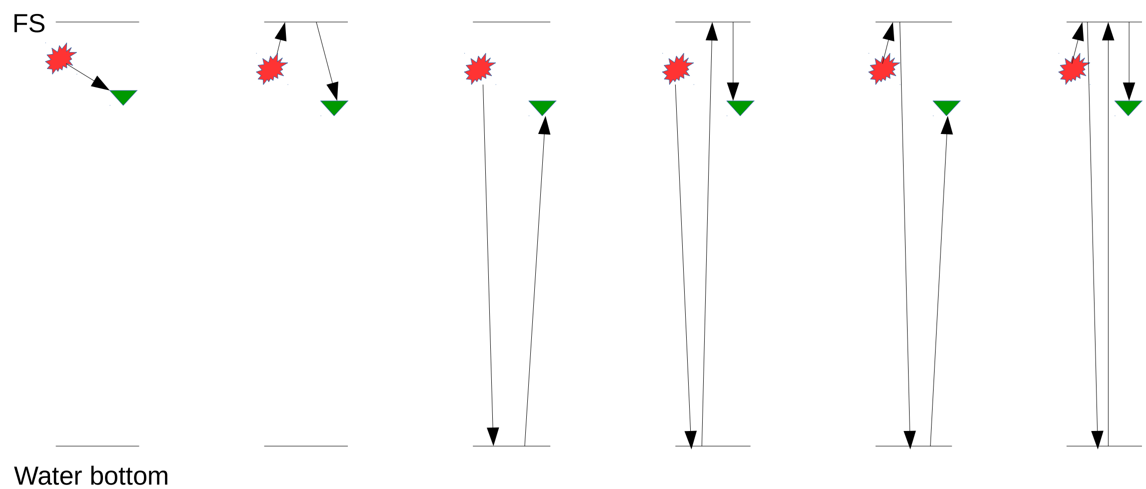

Figure 2.4: Analytic example of Green's theorem P_0/P_s separation. Figures from left to right represent (1) direct wave, (2) reflection of direct wave from free surface, (3) primary from the water bottom, (4) receiver ghost, (5) source ghost, and (6) source-receiver ghost, respectively.

direct wave

$$P^{dir}(z_g, z_s; \omega) = G_0^+(z_g, z_s, \omega) = \frac{e^{ik(z_g - z_s)}}{2ik} \tag{2.20}$$

the reflection of direct wave from free surface

$$P^{dg}(z_g, z_s; \omega) = \frac{e^{i(-k)(0-z_s)}}{2ik}(-1)e^{ik(z_g-0)} = -\frac{e^{ik(z_g+z_s)}}{2ik} \tag{2.21}$$

primary from the water bottom

$$P^{pri}(z_g, z_s; \omega) = \frac{e^{ik(z_{wb}-z_s)}}{2ik}Re^{i(-k)(z_g-z_{wb})} = \frac{R}{2ik}e^{ik(2z_{wb}-z_s-z_g)} \tag{2.22}$$

receiver ghost of this primary

$$P^{rg}(z_g, z_s; \omega) = \frac{e^{ik(z_{wb}-z_s)}}{2ik}Re^{i(-k)(0-z_{wb})}(-1)e^{ik(z_g-0)} = -\frac{R}{2ik}e^{ik(2z_{wb}-z_s+z_g)} \tag{2.23}$$

source ghost of this primary

$$P^{sg}(z_g, z_s; \omega) = \frac{e^{i(-k)(0-z_s)}}{2ik}(-1)e^{ik(z_{wb}-0)}Re^{i(-k)(z_g-Z_{wb})} = -\frac{R}{2ik}e^{ik(2z_{wb}+z_s-z_g)} \tag{2.24}$$

and source-receiver ghost of this primary

$$P^{srg}(z_g, z_s; \omega) = \frac{e^{i(-k)(0-z_s)}}{2ik}(-1)e^{ik(z_{wb}-0)}Re^{i(-k)(0-z_{wb})}(-1)e^{ik(z_g-0)} = \frac{R}{2ik}e^{ik(2z_{wb}+z_s+z_g)}. \tag{2.25}$$

Here $k = \omega/c_0$ is the wave number. R and z_{wb} are reflection coefficient and depth of water bottom, and the free surface is at depth 0 with reflection coefficient -1, respectively. k and $-k$ mean the wave is propagating downwards and upwards, respectively. Assume $0 < z_s < z_g < z_{wb}$ so that the total upwave is the reflection from earth. Summing Equation (2.20)-(2.25), the total wave at z_g is

$$P(z_g, z_s; \omega) = \frac{1}{2ik}[e^{ik(z_g - z_s)} - e^{ik(z_g + z_s)} + Re^{ik(2z_{wb} - z_g - z_s)} \\ - Re^{ik(2z_{wb} - z_g + z_s)} - Re^{ik(2z_{wb} + z_g - z_s)} + Re^{ik(2z_{wb} + z_g + z_s)}] \tag{2.26}$$

In the case of a 1D source and a 1D earth, Equation (2.12) ($0 < z_s < z'_g < z_g$) becomes

$$\begin{aligned} P_0(z'_g, z_s, \omega) &= -[P(z, z_s; \omega)\frac{d}{dz}G_0(z'_g, z; \omega) - G_0(z'_g, z; \omega)\frac{d}{dz}P(z, z_s; \omega)]|_{z=0}^{z=z_g} \\ &= -[P(z, z_s; \omega)\frac{d}{dz}G_0(z'_g, z; \omega) - G_0(z'_g, z; \omega)\frac{d}{dz}P(z, z_s; \omega)]|_{z=z_g} \end{aligned} \tag{2.27}$$

Here at free surface $z = 0$, $P(z, z_s, \omega) = G_0(z, z'_g, \omega) = 0$. And

$$\begin{aligned} P(z, z_s, \omega) &= \frac{1}{2ik}[e^{ik(z - z_s)} - e^{ik(z + z_s)} + Re^{ik(2z_{wb} - z - z_s)} - \\ &\quad Re^{ik(2z_{wb} - z + z_s)} - Re^{ik(2z_{wb} + z - z_s)} + Re^{ik(2z_{wb} + z + z_s)}] \\ \frac{d}{dz}P(z, z_s, \omega) &= \frac{1}{2}[e^{ik(z - z_s)} - e^{ik(z + z_s)} - Re^{ik(2z_{wb} - z - z_s)} + \\ &\quad Re^{ik(2z_{wb} - z + z_s)} - Re^{ik(2z_{wb} + z - z_s)} + Re^{ik(2z_{wb} + z + z_s)}] \\ G_0(z'_g, z, \omega) &= \frac{1}{2ik}e^{ik|z - z'_g|} - \frac{1}{2ik}e^{ik|z + z'_g|} \\ \frac{d}{dz}G_0(z'_g, z, \omega) &= \frac{1}{2}e^{ik|z - z'_g|}sgn(z - z'_g) - \frac{1}{2}e^{ik|z + z'_g|}sgn(z + z'_g) \end{aligned}$$

Substitute these into Equation (2.27) to perform P_0/P_s separation,

$$P_0(z'_g, z_s, \omega) = \frac{e^{ik(z'_g - z_s)}}{2ik} - \frac{e^{ik(z'_g + z_s)}}{2ik} \tag{2.28}$$

Comparing it with Equation (2.20)-(2.25), we can see the right hand side of Equation (2.28) is reference wave at z'_g, including direct wave and its reflection from free surface.

2.2.4 Numerical tests of both the impact and the accommodation of the topography of measurement surface

The velocity model is shown in Figure 2.5. It has a free surface and a horizontal reflector at 100 m depth. Horizontal, inclined and undulated M.S.'s are tested below, respectively. 3D synthetic data are generated on the M.S. using the Cagniard-de Hoop method. The advantage of the Cagniard-de Hoop method is that it can generate any event of the P_0 wave and the P_s wave. $\frac{\partial}{\partial n'}P(\mathbf{r}', \mathbf{r}_s; \omega)$ is estimated using finite difference with data generated on a secondary M.S. close to the original M.S..

Figure 2.5: Velocity model and source position.

2.2.4.1 Horizontal M.S.

The first measurement surface for test is horizontal, which is to show the effectiveness of Equation (2.16). Figure 2.6(a) shows the total wave generated on the horizontal

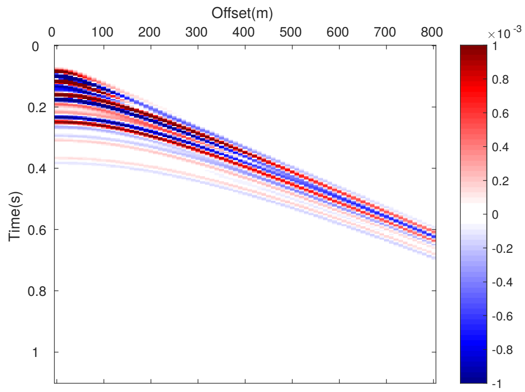

(a)

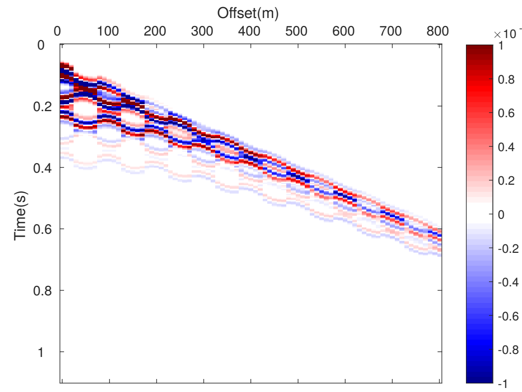

(b)

Figure 2.6: Total wave generated on different measurement surfaces (M.S.). (a) Horizontal M.S. at 50 m depth, and (b) undulated M.S. as shown by Figure 2.10. Colorbar on the right represents the amplitude.

measurement surface using the Cagniard-de Hoop method[1]. Figure 2.7 shows different events respectively generated by the Cagniard-de Hoop method. We can see there is interference between different wave components.

Figure 2.8(a) shows the P_0 wave predicted at 90 m depth using Figure 2.6(a) as input[2]. And Figure 2.9(a) shows comparison in wavelet estimation using predicted P_0 wave at different depth. We can see wavelet estimation at 55 m, 65 m and 90 m depth are all effective, while predicted P_0 wave at 90 m depth gives the most accurate wavelet. This is because as prediction location gets closer to the M.S., smaller offset sampling is needed to maintain accurate evaluation of the integration in Equation (2.16). Thus we choose the deep prediction depth 90 m to guarantee that P_0/P_s is accurate enough, as shown by Figure 2.8(a). Also in numerical examples

[1] Figure 2.6(b) shows the total wave generated on a undulated measurement surface, which will be explained in latter subsection.

[2] Figure 2.8(b)-2.8(f) show the predicted P_0 wave results using input total wave generated on non-horizontal measurement surfaces, which are used by latter subsections.

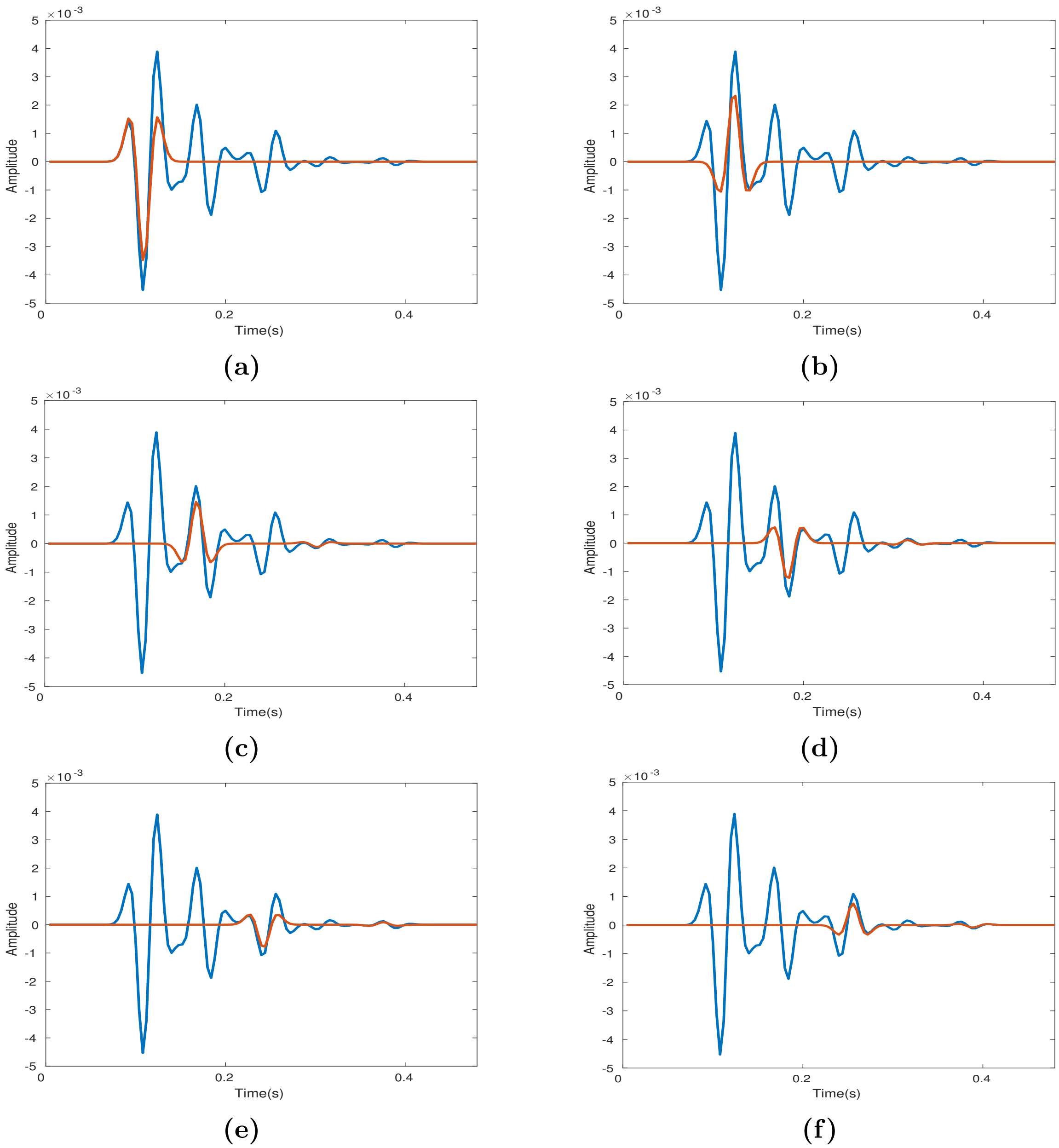

Figure 2.7: Traceplot (offset=0m) of total wave (—) and different events (—) in Figure 2.6(a). **(a)** Direct wave, **(b)** reflection of direct wave from free surface, **(c)** primary and free surface multiple, **(d)** source ghosts, **(e)** receiver ghosts, and **(f)** source-receiver ghosts.

below, the P_0 wave prediction depth is all chosen to be 90 m.

2.2.4.2 Inclined M.S.

The second group of numerical examples tests P_0/P_s separation and wavelet estimation with inclined M.S. but assuming it's horizontal in P_0/P_s separation, using Equation (2.16). Figure 2.8(b)-2.8(d) show the predicted P_0 wave at 90 m depth with 0.1°, 1° and 2° M.S., respectively. And Figure 2.9(b) shows the corresponding wavelet estimation including the actual wavelet. We can see the result of 0.1° M.S. is very effective, but those of 1° M.S. and 2° M.S. have obvious artifacts in both the P_0 prediction and subsequent wavelet estimation. This is probably because P_0 wave has direct wave that travels from the source directly to the receiver; hence P_0/P_s separation is sensitive to the topography of M.S..

2.2.4.3 Undulated M.S.

The last group of numerical examples compares (1) wavelet estimation using inclined M.S. (as shown by Figure 2.10) while assuming it's horizontal in P_0/P_s separation (using Equation (2.16)), with (2) wavelet estimation using the same inclined M.S. while accommodating its topography in P_0/P_s separation (using Equation (2.17)). Figure 2.6(b) shows the total wave generated on the undulated M.S.. Figure 2.8(e) shows the P_0 wave predicted at 90 m depth with horizontal M.S. assumption. In comparison with Figure 2.8(a), it has many artifacts. And these artifacts contaminates subsequent wavelet estimation, as shown by Figure 2.9(c) (– – –).

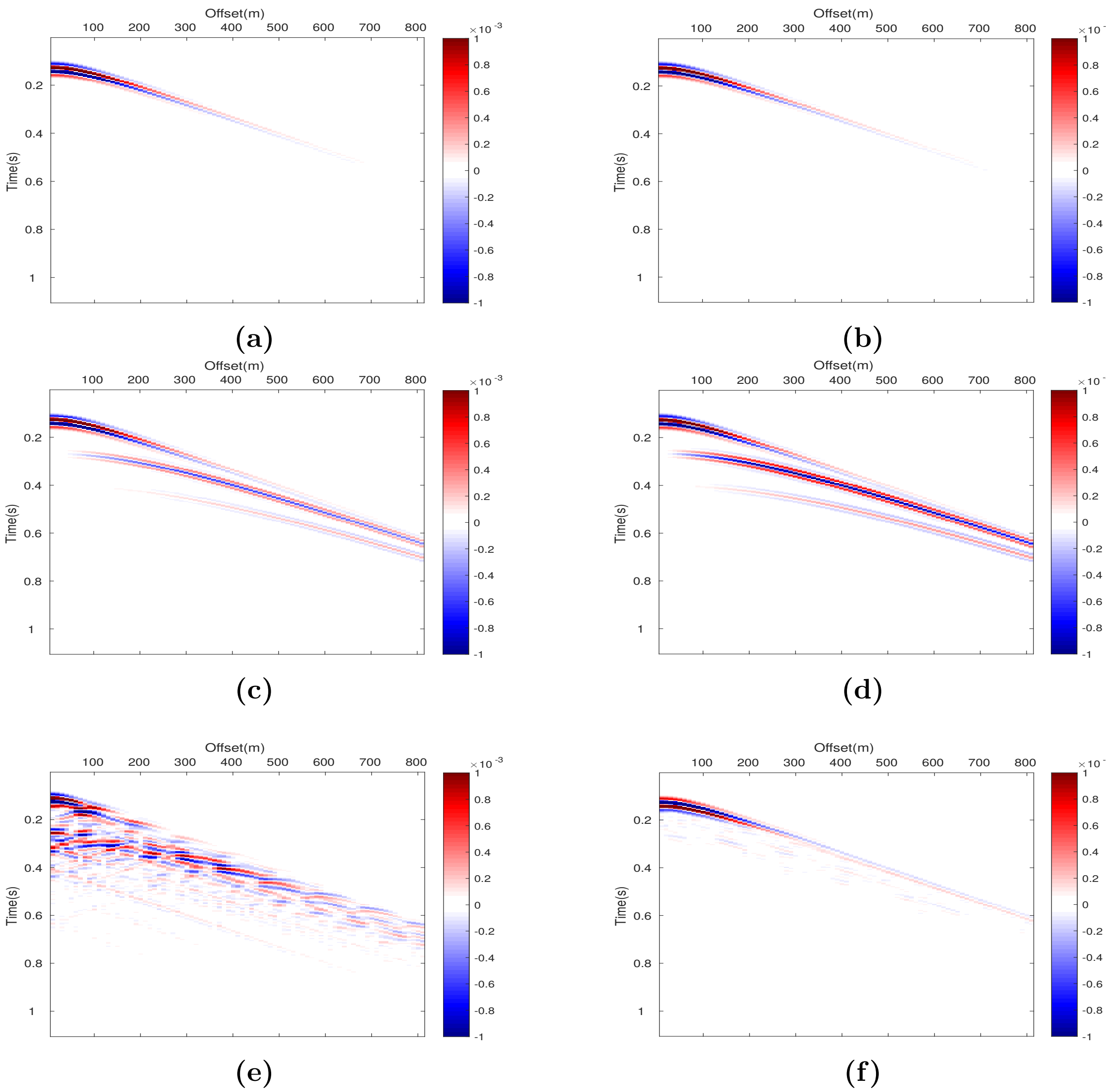

Figure 2.8: Separated P_0 wave using different measurement surface (M.S.) and/or different assumption of the measurement surface. **(a)** M.S. is horizontal, **(b)** M.S. has $0.1°$ inclination while P_0/P_s separation assumes it's horizontal, **(c)** M.S. has $1°$ inclination while P_0/P_s separation assumes it's horizontal, **(d)** M.S. has $2°$ inclination while P_0/P_s separation assumes it's horizontal, **(e)** M.S. is undulated while P_0/P_s separation assumes it's horizontal, and **(f)** M.S. is undulated and P_0/P_s separation accommodates its topography. Colorbar on the right represents the amplitude.

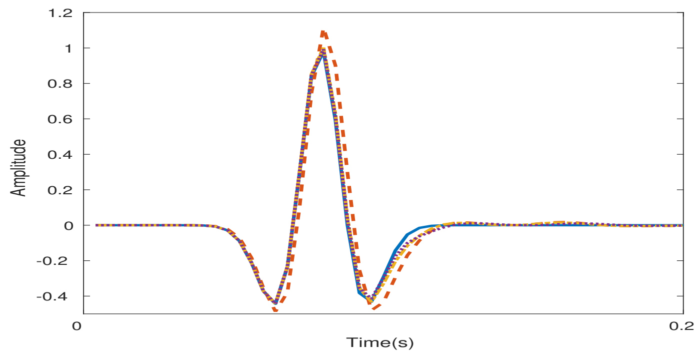

(a)

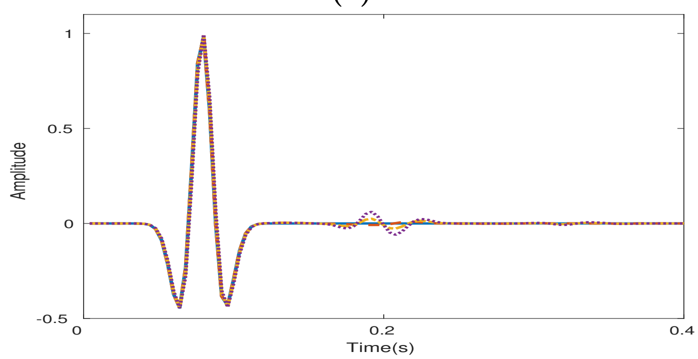

(b)

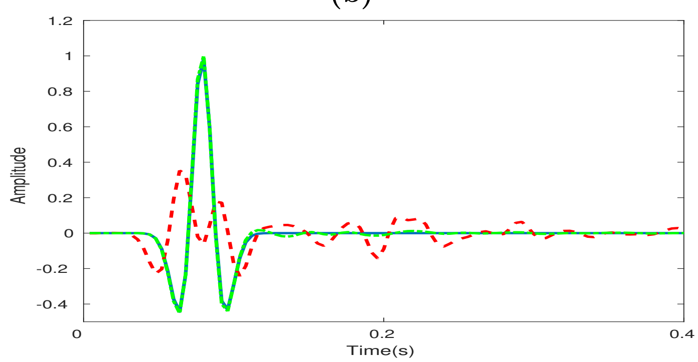

(c)

Figure 2.9: Wavelet estimation comparison using different measurement surface (M.S.) and/or different assumption of the measurement surface. **(a)** Actual wavelet (—) and wavelet estimated based on P_0 wave predicted at respectively 55 m depth (– – –), 65 m depth (– · –) and 90 m depth (· · · ·) , using actually horizontal M.S., **(b)** actual wavelet (—) and wavelet estimated respectively using predicted P_0 wave of Figure 2.8(b) (– – –), predicted P_0 wave of Figure 2.8(c) (– · – – –) and predicted P_0 wave of Figure 2.8(d) (· · · ·), **(c)** actual wavelet (—) and wavelet estimated using predicted P_0 wave of Figure 2.8(e) (– – –) and predicted P_0 wave of Figure 2.8(f) (– · – ·).

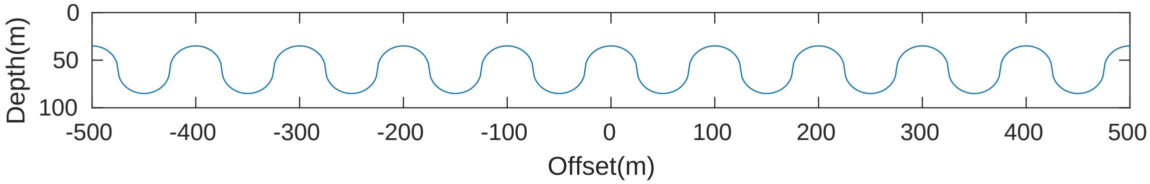

Figure 2.10: Configuration of the undulated cable. Maximum depth is 75 m. Minimum depth is 25 m.

Figure 2.8(f) shows the P_0 wave predicted at 90 m depth with accommodation of M.S. topography. We can see that although the M.S. undulates obviously, the wave separation result is almost as effective as Figure 2.8(a). The subsequent wavelet estimation is shown by Figure 2.9(c) (– · – ·). Clearly, the waveform of true source signature (—) is effectively recovered.

2.3 Source and receiver deghosting

Green's theorem derived deghosting methods in the space-frequency domain using a horizontal measurement surface (M.S.) have been successfully applied to synthetic and field data. Based on Green's theorem wavefield separation theory, this section derives a 3D source and receiver deghosting formula for a depth-variable M.S. assuming its topography is known. In numerical tests, the model has a free surface and one horizontal reflector. We use the Cagniard-de Hoop method to generate synthetic data on horizontal, inclined, and undulated measurement surfaces. Numerical results show that the current Green's theorem deghosting formula for a constant depth M.S. remains useful for a mildly depth-variable M.S.. When the actual M.S. deviates significantly from horizontal, the horizontal M.S. formula produces serious errors and artifacts whereas the new formula produces an effective and satisfactory result. While the analysis and tests in this paper are based on nonhorizontal towed streamers, the motivation (and future work) is for on-shore and ocean-bottom acquisition. Under these circumstances, the deviation from horizontal acquisition can be significant and the ability to accommodate a variable topography can have a considerably positive impact on subsequence processing and interpretation objectives.

2.3.1 Theory of receiver side deghosting

If we choose the reference medium to be a whole space of water (Figure 2.11(b)), whose property is the same as the actual medium (Figure 2.11(a)) along the measurement surface, the differences between the reference medium and the actual medium can be described as sources (Figure 2.11(c)) ρ, corresponding to the 'source' function or inhomogeneous driving force term(s) in a differential equation governing propagation in the reference medium. There are three sources required for the actual medium and experiment in Figure 2.11(a), using a reference medium in Figure 2.11(b). These three sources are the airgun ρ_{airgun}, the air perturbation ρ_{air}, and the earth perturbation ρ_{earth}, respectively, and $\rho = \rho_{air} + \rho_{airgun} + \rho_{earth}$.

According to the Lippmann-Schwinger equation, the total wavefield at a location $\mathbf{r}$ can be expressed as,

$$\begin{aligned} P(\mathbf{r};\omega) &= \int_{\infty} \rho(\mathbf{r}')G_0^+(\mathbf{r},\mathbf{r}';\omega)d\mathbf{r}' \\ &= \int_{\infty} \rho_{air}(\mathbf{r}')G_0^+ d\mathbf{r}' + \int_{\infty} \rho_{airgun}(\mathbf{r}')G_0^+ d\mathbf{r}' + \int_{\infty} \rho_{earth}(\mathbf{r}')G_0^+ d\mathbf{r}' \end{aligned} \tag{2.29}$$

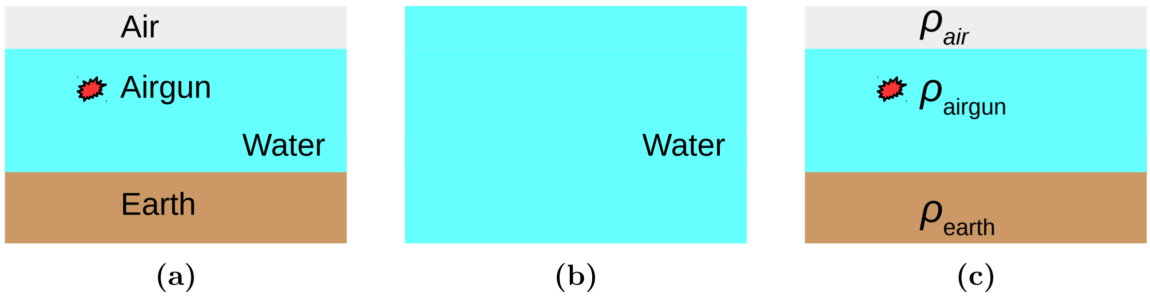

Figure 2.11: (a) Actual medium and experiment, (b) reference medium, and (c) three sources overlaid on the reference medium.

Here $G_0^+(\mathbf{r}, \mathbf{r}'; \omega)$ is a causal Green's function for the homogeneous whole-space reference medium. Its expression is $G_0^+(\mathbf{r}, \mathbf{r}', \omega) = -\frac{1}{4\pi}\frac{exp(ik|\mathbf{r}-\mathbf{r}'|)}{|\mathbf{r}-\mathbf{r}'|}$. Each of the three sources generates an outgoing wave (corresponding to the three terms of the right hand side of Equation (2.29)), propagating straight away from the source point to the field point. Choose an enclosed volume V' that is bounded by surface S' (as shown by the dashed surface [- - -] in Figure 2.12) whose bottom surface is the measurement surface (M.S.) and whose top is an infinite hemisphere. It was shown by Weglein and Secrest (1990) that the Green's theorem derived surface integral,

$$\oint_{S'} \left[P(\mathbf{r}'; \omega)\nabla_{\mathbf{r}'} G_0^+(\mathbf{r}, \mathbf{r}'; \omega) - G_0^+(\mathbf{r}, \mathbf{r}'; \omega)\nabla_{\mathbf{r}'} P(\mathbf{r}'; \omega) \right] \cdot d\mathbf{S}' \qquad (2.30)$$

represents the contribution to the wavefield at any location $\mathbf{r}$ inside the volume V', due to sources outside the volume V'. Here $d\mathbf{S}'$ is the surface element of S' at $\mathbf{r}'$ whose direction is outwards normal to S'. Since the chosen volume V' encloses the air and the airgun, the outside contribution only comes from ρ_{earth} beneath the M.S.. At any point $\mathbf{r} = \mathbf{r}_g$ within V', the integral in Equation (2.30) gives the contribution of the total field due to the source outside ρ_{earth}. That contribution $\int \rho_{earth} G_0^+ d\mathbf{r}'$ is always propagating away from every point in ρ_{earth} and is always upgoing. If, in

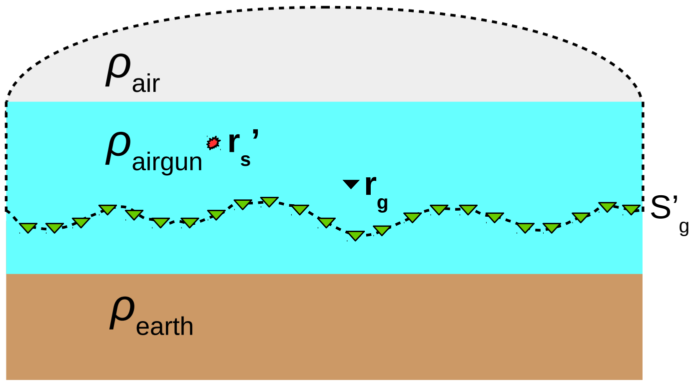

Figure 2.12: The volume and output point $\mathbf{r}_g$ in Green's theorem receiver side deghosting.

addition, the output point $\mathbf{r} = \mathbf{r}_g$ in Equation (2.29) is chosen below ρ_{airgun} (and hence below ρ_{air}); then $\int_{V'}(\rho_{air} + \rho_{airgun})G_0^+ d\mathbf{r}'$ is downgoing at that point $\mathbf{r}$ inside V' and below ρ_{airgun}. For that type of output point, the $\int \rho_{earth} G_0^+ d\mathbf{r}'$ is both the contribution to the field in V' due to ρ_{earth} and the portion of field at $\mathbf{r}$ that is upgoing.

Therefore, we can achieve receiver deghosting at $\mathbf{r}_g$ in terms of up/down separation (Weglein et al., 2002; Zhang and Weglein, 2005),

$$P^{Rd}(\mathbf{r}_g;\omega) = \oint_{S'} \Big[P(\mathbf{r}';\omega)\nabla_{\mathbf{r}'}G_0^+(\mathbf{r}_g,\mathbf{r}';\omega) - G_0^+(\mathbf{r}_g,\mathbf{r}';\omega)\nabla_{\mathbf{r}'}P(\mathbf{r}';\omega)\Big] \cdot d\mathbf{S}' \quad (2.31)$$

Here, P^{Rd} means receiver deghosted data. We can prove that the integration over the hemisphere goes to zero as its radius goes to infinity, using Sommerfeld radiation condition. Hence,

$$P^{Rd}(\mathbf{r}_g;\omega) = \int_{S'_g} \Big[P(\mathbf{r}';\omega)\nabla_{\mathbf{r}'}G_0^+(\mathbf{r}_g,\mathbf{r}';\omega) - G_0^+(\mathbf{r}_g,\mathbf{r}';\omega)\nabla_{\mathbf{r}'}P(\mathbf{r}';\omega)\Big] \cdot d\mathbf{S}'_g \quad (2.32)$$

2.3.2 Theory of source side deghosting

The Green's theorem deghosting on the source-side can be achieved similarly based on the up/down separation (Zhang and Weglein, 2005, 2006; Zhang, 2007) (with a second application of Equation (2.32)) as expressed by the equation below,

$$P^{SRd}(\mathbf{r}_g,\mathbf{r}_s;\omega) = \tag{2.33}$$
$$\int_{S'_s}\left\{P^{rd}(\mathbf{r}_g,\mathbf{r}'_s;\omega)\nabla_{\mathbf{r}'_s}G_0^+(\mathbf{r}_s,\mathbf{r}'_s;\omega)-G_0^+(\mathbf{r}_s,\mathbf{r}'_s;\omega)\nabla_{\mathbf{r}'_s}P^{rd}(\mathbf{r}_g,\mathbf{r}'_s;\omega)\right\}\cdot d\mathbf{S}'_s$$

where $P^{rd}(\mathbf{r}_g,\mathbf{r}'_s;\omega)$ is receiver deghosted data given by Equation (2.32). If we take Equation (2.32) into Equation (2.33), we can further get

$$P^{SRd}(\mathbf{r}_g,\mathbf{r}_s;\omega) = \tag{2.34}$$
$$\int_{S'_s}\left\{\int_{S'_g}\left[P(\mathbf{r}'_g,\mathbf{r}'_s;\omega)\nabla_{\mathbf{r}'_g}G_0^+(\mathbf{r}_g,\mathbf{r}'_g;\omega)-G_0^+(\mathbf{r}_g,\mathbf{r}'_g;\omega)\nabla_{\mathbf{r}'_g}P(\mathbf{r}'_g,\mathbf{r}'_s;\omega)\right]\cdot d\mathbf{S}'_g\right.$$
$$\nabla_{\mathbf{r}'_s}G_0^+(\mathbf{r}_s,\mathbf{r}'_s;\omega)-G_0^+(\mathbf{r}_s,\mathbf{r}'_s;\omega)$$
$$\left.\nabla_{\mathbf{r}'_s}\int_{S'_g}\left[P(\mathbf{r}'_g,\mathbf{r}'_s;\omega)\nabla_{\mathbf{r}'_g}G_0^+(\mathbf{r}_g,\mathbf{r}'_g;\omega)-G_0^+(\mathbf{r}_g,\mathbf{r}'_g;\omega)\nabla_{\mathbf{r}'_g}P(\mathbf{r}'_g,\mathbf{r}'_s;\omega)\right]\cdot d\mathbf{S}'_g\right\}\cdot d\mathbf{S}'_s$$

2.3.3 Accommodation of deghosting for a non-horizontal measurement surface

When S'_s and S'_g are horizontal, Equation (2.33) reduces to

$$P^{SRd}(x_g,y_g,z_g,x_s,y_s,z_s;\omega) = \tag{2.35}$$
$$\int_{S'_s}dx'_s dy'_s\left\{\frac{\partial}{\partial z''_s}G_0^+(x_s,y_s,z_s,x'_s,y'_s,z''_s;\omega)\Big|_{z''_s=z'_s}P^{rd}(x_g,y_g,z_g,x'_s,y'_s,z'_s;\omega)-\right.$$
$$\left.G_0^+(x_s,y_s,z_s,x'_s,y'_s,z'_s;\omega)\frac{\partial}{\partial z''_s}P^{rd}(x_g,y_g,z_g,x'_s,y'_s,z''_s;\omega)\Big|_{z''_s=z'_s}\right\}$$

where the receiver deghosted data Equation (2.32) reduces to

$$
\begin{aligned}
&P^{rd}(x_g, y_g, z_g, x'_s, y'_s, z'_s;\omega) = \qquad (2.36)\\
&\int_{S'_g} dx'_g dy'_g \Bigg\{ \frac{\partial}{\partial z''_g} G_0^+(x_g, y_g, z_g, x'_g, y'_g, z''_g;\omega)\Big|_{z''_g=z'_g} P(x'_g, y'_g, z'_g, x'_s, y'_s, z'_s;\omega) - \\
&\quad G_0^+(x_g, y_g, z_g, x'_g, y'_g, z'_g;\omega) \frac{\partial}{\partial z''_g} P(x'_g, y'_g, z''_g, x'_s, y'_s, z'_s;\omega)\Big|_{z''_g=z'_g} \Bigg\}
\end{aligned}
$$

And hence Equation (2.34) reduces to

$$
\begin{aligned}
&P^{SRd}(\mathbf{r}_g, \mathbf{r}_s;\omega) \qquad (2.37)\\
&= \int_{S'_s} dx'_s dy'_s \\
&\Bigg\{ \int_{S'_g} dx'_g dy'_g \left[\frac{\partial}{\partial z'_g} G_0^+(\mathbf{r}_g, \mathbf{r}'_g;\omega) P(\mathbf{r}'_g, \mathbf{r}'_s;\omega) - G_0^+(\mathbf{r}_g, \mathbf{r}'_g;\omega) \frac{\partial}{\partial z'_g} P(\mathbf{r}'_g, \mathbf{r}'_s;\omega) \right] \frac{\partial}{\partial z'_s} G_0^+(\mathbf{r}_s, \mathbf{r}'_s;\omega) - \\
&G_0^+(\mathbf{r}_s, \mathbf{r}'_s;\omega) \frac{\partial}{\partial z'_s} \int_{S'_g} dx'_g dy'_g \left[\frac{\partial}{\partial z'_g} G_0^+(\mathbf{r}_g, \mathbf{r}'_g;\omega) P(\mathbf{r}'_g, \mathbf{r}'_s;\omega) - G_0^+(\mathbf{r}_g, \mathbf{r}'_g;\omega) \frac{\partial}{\partial z'_g} P(\mathbf{r}'_g, \mathbf{r}'_s;\omega) \right] \Bigg\} \\
&= \int_{S'_s} dx'_s dy'_s \int_{S'_g} dx'_g dy'_g \\
&\Bigg\{ \frac{\partial}{\partial z'_g} G_0^+(\mathbf{r}_g, \mathbf{r}'_g;\omega) P(\mathbf{r}'_g, \mathbf{r}'_s;\omega) \frac{\partial}{\partial z'_s} G_0^+(\mathbf{r}_s, \mathbf{r}'_s;\omega) - G_0^+(\mathbf{r}_g, \mathbf{r}'_g;\omega) \frac{\partial}{\partial z'_g} P(\mathbf{r}'_g, \mathbf{r}'_s;\omega) \frac{\partial}{\partial z'_s} G_0^+(\mathbf{r}_s, \mathbf{r}'_s;\omega) - \\
&\frac{\partial}{\partial z'_g} G_0^+(\mathbf{r}_g, \mathbf{r}'_g;\omega) \left[\frac{\partial}{\partial z'_s} P(\mathbf{r}'_g, \mathbf{r}'_s;\omega) \right] G_0^+(\mathbf{r}_s, \mathbf{r}'_s;\omega) + G_0^+(\mathbf{r}_g, \mathbf{r}'_g;\omega) \left[\frac{\partial^2}{\partial z'_s \partial z'_g} P(\mathbf{r}'_g, \mathbf{r}'_s;\omega) \right] G_0^+(\mathbf{r}_s, \mathbf{r}'_s;\omega) \Bigg\} \\
&= \int_{S'_s} dx'_s dy'_s \int_{S'_g} dx'_g dy'_g \\
&\Bigg\{ \frac{\partial}{\partial z'_g} G_0^+(\mathbf{r}_g, \mathbf{r}'_g;\omega) P(\mathbf{r}'_g, \mathbf{r}'_s;\omega) \frac{\partial}{\partial z'_s} G_0^+(\mathbf{r}'_s, \mathbf{r}_s;\omega) - G_0^+(\mathbf{r}_g, \mathbf{r}'_g;\omega) \frac{\partial}{\partial z'_g} P(\mathbf{r}'_g, \mathbf{r}'_s;\omega) \frac{\partial}{\partial z'_s} G_0^+(\mathbf{r}'_s, \mathbf{r}_s;\omega) - \\
&\frac{\partial}{\partial z'_g} G_0^+(\mathbf{r}_g, \mathbf{r}'_g;\omega) \left[\frac{\partial}{\partial z'_s} P(\mathbf{r}'_g, \mathbf{r}'_s;\omega) \right] G_0^+(\mathbf{r}'_s, \mathbf{r}_s;\omega) + G_0^+(\mathbf{r}_g, \mathbf{r}'_g;\omega) \left[\frac{\partial^2}{\partial z'_s \partial z'_g} P(\mathbf{r}'_g, \mathbf{r}'_s;\omega) \right] G_0^+(\mathbf{r}'_s, \mathbf{r}_s;\omega) \Bigg\}
\end{aligned}
$$

When z'_g is a function of x'_g and y'_g, Equation (2.32) reduces to

$$P^{rd}(x_g, y_g, z_g, x'_s, y'_s, z'_s, \omega) = \int_{S'_g} \Sigma \, dx'_g dy'_g \tag{2.38}$$
$$\Big\{ (-\frac{1}{\Sigma}\frac{\partial z'_g}{\partial x'_g}\frac{\partial}{\partial x'_g} - \frac{1}{\Sigma}\frac{\partial z'_g}{\partial y'_g}\frac{\partial}{\partial y'_g} + \frac{1}{\Sigma}\frac{\partial}{\partial z'_g}) G_0^+(x_g, y_g, z_g, x'_g, y'_g, z'_g, \omega)$$
$$P(x'_g, y'_g, z'_g, x'_s, y'_s, z'_s, \omega) - G_0^+(x_g, y_g, z_g, x'_g, y'_g, z'_g, \omega)\frac{\partial}{\partial n'} P(x'_g, y'_g, z'_g, x'_s, y'_s, z'_s, \omega) \Big\}$$

where $\Sigma = \sqrt{1 + (\partial z'_g/\partial x'_g)^2 + (\partial z'_g/\partial y'_g)^2}$.

2.3.4 1D analytic example

Assume the source is at z'_s and the receiver is at z'_g. As shown in Figure 2.13, total wave at z'_g consists of (from left to right)

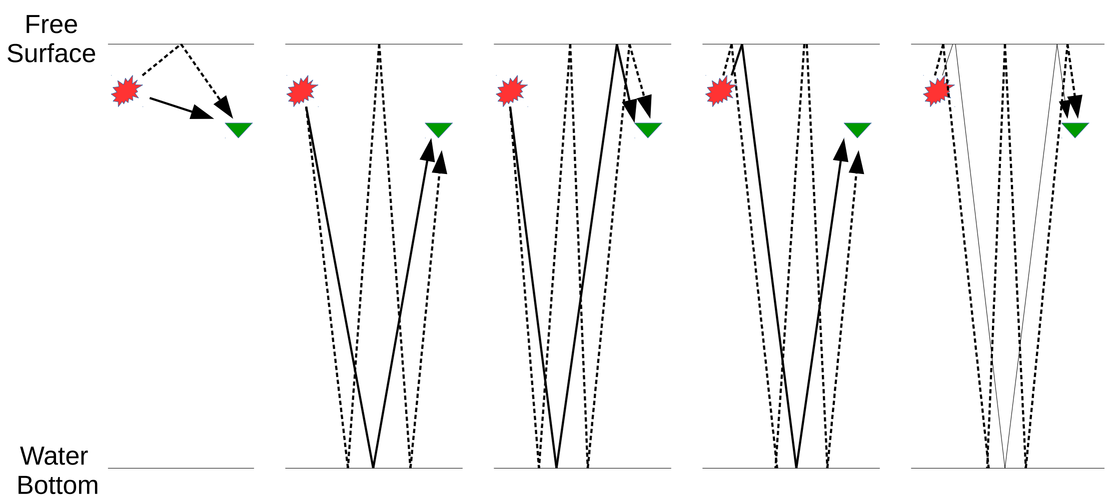

Figure 2.13: Different events of 1D analytic data for deghosting.

(1) direct wave (solid line)

$$P^{dir}(z'_g, z'_s; \omega) = G_0^+(z'_g, z'_s, \omega) = \frac{e^{ik(z'_g - z'_s)}}{2ik} \tag{2.39}$$

with the reflection of direct wave from free surface (dash line),

$$P^{dg}(z'_g, z'_s; \omega) = -\frac{e^{ik(z'_g+z'_s)}}{2ik} \tag{2.40}$$

(2) primary from the water bottom (solid line)

$$P^{pri}(z'_g, z'_s; \omega) = \frac{R}{2ik} e^{ik(2z_{wb}-z'_s-z'_g)} \tag{2.41}$$

with the free surface multiple (dash line),

$$P^{FSM}(z'_g, z'_s; \omega) = -\frac{R^2}{2ik} e^{ik(4z_{wb}-z'_s-z'_g)} \tag{2.42}$$

(3) receiver ghosts of the primary (solid line)

$$P^{prg}(z'_g, z'_s; \omega) = -\frac{R}{2ik} e^{ik(2z_{wb}-z'_s+z'_g)} \tag{2.43}$$

and receiver ghosts of the free surface multiple (dash line),

$$P^{FSMrg}(z'_g, z'_s; \omega) = \frac{R^2}{2ik} e^{ik(4z_{wb}-z'_s+z'_g)} \tag{2.44}$$

(4) source ghosts of the primary (solid line)

$$P^{psg}(z'_g, z'_s; \omega) = -\frac{R}{2ik} e^{ik(2z_{wb}+z'_s-z'_g)} \tag{2.45}$$

and source ghosts of the free surface multiple (dash line),

$$P^{FSMsg}(z'_g, z'_s; \omega) = \frac{R^2}{2ik} e^{ik(4z_{wb}+z'_s-z'_g)} \tag{2.46}$$

(5) source-receiver ghosts of the primary (solid line)

$$P^{psrg}(z'_g, z'_s; \omega) = \frac{R}{2ik} e^{ik(2z_{wb}+z'_s+z'_g)} \tag{2.47}$$

and source-receiver ghosts of the free surface multiple (dash line).

$$P^{FSMsrg}(z_g', z_s'; \omega) = -\frac{R^2}{2ik} e^{ik(4z_{wb}+z_s'+z_g')} \tag{2.48}$$

In the case of a 1D source and a 1D earth, Equation (2.37) reduces to

$$\begin{aligned}
& P^{SRd}(z_g, z_s; \omega) \\
= & \left\{ \frac{\partial}{\partial z_g''} G_0^+(z_g, z_g''; \omega) P(z_g'', z_s''; \omega) \frac{\partial}{\partial z_s''} G_0^+(z_s'', z_s; \omega) - \right. \\
& G_0^+(z_g, z_g''; \omega) \frac{\partial}{\partial z_g''} P(z_g'', z_s''; \omega) \frac{\partial}{\partial z_s''} G_0^+(z_s'', z_s; \omega) - \\
& \frac{\partial}{\partial z_g''} G_0^+(z_g, z_g''; \omega) \left[\frac{\partial}{\partial z_s''} P(z_g'', z_s''; \omega) \right] G_0^+(z_s'', z_s; \omega) + \\
& \left. G_0^+(z_g, z_g''; \omega) \left[\frac{\partial^2}{\partial z_s'' \partial z_g''} P(z_g'', z_s''; \omega) \right] G_0^+(z_s'', z_s; \omega) \right\} \Bigg|_{z_g''=z_g'}^{z_g''=+\infty} \Bigg|_{z_s''=z_s'}^{z_s''=+\infty} \\
= & \left\{ \frac{\partial}{\partial z_g''} G_0^+(z_g, z_g''; \omega) P(z_g'', z_s''; \omega) \frac{\partial}{\partial z_s''} G_0^+(z_s'', z_s; \omega) - \right. \\
& G_0^+(z_g, z_g''; \omega) \frac{\partial}{\partial z_g''} P(z_g'', z_s''; \omega) \frac{\partial}{\partial z_s''} G_0^+(z_s'', z_s; \omega) - \\
& \frac{\partial}{\partial z_g''} G_0^+(z_g, z_g''; \omega) \left[\frac{\partial}{\partial z_s''} P(z_g'', z_s''; \omega) \right] G_0^+(z_s'', z_s; \omega) + \\
& \left. G_0^+(z_g, z_g''; \omega) \left[\frac{\partial^2}{\partial z_s'' \partial z_g''} P(z_g'', z_s''; \omega) \right] G_0^+(z_s'', z_s; \omega) \right\} \Bigg|_{z_g''=z_g', z_s''=z_s'} \\
= & \frac{1}{4ik} e^{ik(z_g'-z_g)} e^{ik(z_s'-z_s)} \left[ikP(z_g'', z_s''; \omega) - \frac{\partial}{\partial z_g''} P(z_g'', z_s''; \omega) - \frac{\partial}{\partial z_s''} P(z_g'', z_s''; \omega) + \right. \\
& \left. \frac{1}{ik} \frac{\partial^2}{\partial z_s'' \partial z_g''} P(z_g'', z_s''; \omega) \right]_{z_g''=z_g', z_s''=z_s'}
\end{aligned} \tag{2.49}$$

where

$$
\begin{aligned}
&G_0^+(z_g, z_g''; \omega) = \frac{1}{2ik} e^{ik|z_g - z_g''|} \\
&\frac{\partial}{\partial z_g''} G_0^+(z_g, z_g''; \omega) = \frac{1}{2} e^{ik|z_g - z_g''|} sgn(z_g'' - z_g) \\
&G_0^+(z_s'', z_s; \omega) = \frac{1}{2ik} e^{ik|z_s'' - z_s|} \\
&\frac{\partial}{\partial z_s''} G_0^+(z_s'', z_s; \omega) = \frac{1}{2} e^{ik|z_s'' - z_s|} sgn(z_s'' - z_s)
\end{aligned}
$$

and

$$P(z_g'', z_s''; \omega) =$$

$$\frac{e^{ik(z_g''-z_s'')}}{2ik} - \frac{e^{ik(z_g''+z_s'')}}{2ik} + \frac{R}{2ik}e^{ik(2z_{wb}-z_s''-z_g'')} - \frac{R}{2ik}e^{ik(2z_{wb}-z_s''+z_g'')} -$$
$$\frac{R}{2ik}e^{ik(2z_{wb}+z_s''-z_g'')} + \frac{R}{2ik}e^{ik(2z_{wb}+z_s''+z_g'')} - \frac{R^2}{2ik}e^{ik(4z_{wb}-z_s''-z_g'')} +$$
$$\frac{R^2}{2ik}e^{ik(4z_{wb}-z_s''+z_g'')} + \frac{R^2}{2ik}e^{ik(4z_{wb}+z_s''-z_g'')} - \frac{R^2}{2ik}e^{ik(4z_{wb}+z_s''+z_g'')}$$

$$\frac{\partial}{\partial z_g''}P(z_g'', z_s''; \omega) =$$

$$\frac{1}{2}e^{ik(z_g''-z_s'')} - \frac{1}{2}e^{ik(z_g''+z_s'')} - \frac{R}{2}e^{ik(2z_{wb}-z_s''-z_g'')} - \frac{R}{2}e^{ik(2z_{wb}-z_s''+z_g'')} +$$
$$\frac{R}{2}e^{ik(2z_{wb}+z_s''-z_g'')} + \frac{R}{2}e^{ik(2z_{wb}+z_s''+z_g'')} + \frac{R^2}{2}e^{ik(4z_{wb}-z_s''-z_g'')} +$$
$$\frac{R^2}{2}e^{ik(4z_{wb}-z_s''+z_g'')} - \frac{R^2}{2}e^{ik(4z_{wb}+z_s''-z_g'')} - \frac{R^2}{2}e^{ik(4z_{wb}+z_s''+z_g'')}$$

$$\frac{\partial}{\partial z_s''}P(z_g'', z_s''; \omega) =$$

$$-\frac{1}{2}e^{ik(z_g''-z_s'')} - \frac{1}{2}e^{ik(z_g''+z_s'')} - \frac{R}{2}e^{ik(2z_{wb}-z_s''-z_g'')} + \frac{R}{2}e^{ik(2z_{wb}-z_s''+z_g'')} -$$
$$\frac{R}{2}e^{ik(2z_{wb}+z_s''-z_g'')} + \frac{R}{2}e^{ik(2z_{wb}+z_s''+z_g'')} + \frac{R^2}{2}e^{ik(4z_{wb}-z_s''-z_g'')} -$$
$$\frac{R^2}{2}e^{ik(4z_{wb}-z_s''+z_g'')} + \frac{R^2}{2}e^{ik(4z_{wb}+z_s''-z_g'')} - \frac{R^2}{2}e^{ik(4z_{wb}+z_s''+z_g'')}$$

$$\frac{\partial^2}{\partial z_s''\partial z_g''}P(z_g'', z_s''; \omega) =$$

$$-\frac{ik}{2}e^{ik(z_g''-z_s'')} - \frac{ik}{2}e^{ik(z_g''+z_s'')} + \frac{ikR}{2}e^{ik(2z_{wb}-z_s''-z_g'')} + \frac{ikR}{2}e^{ik(2z_{wb}-z_s''+z_g'')} +$$
$$\frac{ikR}{2}e^{ik(2z_{wb}+z_s''-z_g'')} + \frac{ikR}{2}e^{ik(2z_{wb}+z_s''+z_g'')} - \frac{ikR^2}{2}e^{ik(4z_{wb}-z_s''-z_g'')} -$$
$$\frac{ikR^2}{2}e^{ik(4z_{wb}-z_s''+z_g'')} - \frac{ikR^2}{2}e^{ik(4z_{wb}+z_s''-z_g'')} - \frac{ikR^2}{2}e^{ik(4z_{wb}+z_s''+z_g'')}$$

So

$$-\frac{\partial}{\partial z_g''}P(z_g'', z_s''; \omega) - \frac{\partial}{\partial z_s''}P(z_g'', z_s''; \omega) =$$

$$e^{ik(z_g''+z_s'')} + Re^{ik(2z_{wb}-z_s''-z_g'')} - Re^{ik(2z_{wb}+z_s''+z_g'')} - R^2e^{ik(4z_{wb}-z_s''-z_g'')} + R^2e^{ik(4z_{wb}+z_s''+z_g'')}$$

$$ikP(z_g'', z_s''; \omega) + \frac{1}{ik}\frac{\partial^2}{\partial z_s''\partial z_g''}P(z_g'', z_s''; \omega) =$$

$$-e^{ik(z_g''+z_s'')} + Re^{ik(2z_{wb}-z_s''-z_g'')} + Re^{ik(2z_{wb}+z_s''+z_g'')} - R^2e^{ik(4z_{wb}-z_s''-z_g'')} - R^2e^{ik(4z_{wb}+z_s''+z_g'')}$$

Therefore, continuing Equation (2.49)

$$\begin{aligned}
&P^{SRd}(z_g, z_s; \omega) \qquad (2.50)\\
&= \frac{1}{4ik}e^{ik(z_g'-z_g)}e^{ik(z_s'-z_s)}\left[2Re^{ik(2z_{wb}-z_s''-z_g'')} - 2R^2e^{ik(4z_{wb}-z_s''-z_g'')}\right]_{z_g''=z_g', z_s''=z_s'}\\
&= \frac{1}{4ik}e^{ik(z_g'-z_g)}e^{ik(z_s'-z_s)}\left[2Re^{ik(2z_{wb}-z_s'-z_g')} - 2R^2e^{ik(4z_{wb}-z_s'-z_g')}\right]\\
&= \frac{R}{2ik}e^{ik(2z_{wb}-z_s-z_g)} - \frac{R^2}{2ik}e^{ik(4z_{wb}-z_s-z_g)}
\end{aligned}$$

In comparison with Equation (2.41) and Equation (2.42), we can see Equation (2.50) predicts the source and receiver deghosted data that can be received at $z = z_g$ for source at $z = z_s$.

2.3.5 Numerical tests of both the impact and the accommodation of the topography of measurement surface

The velocity model is shown in Figure 2.14. It has a free surface and a horizontal reflector at the depth of 50 m. Below there are three numerical examples that generate the total wave

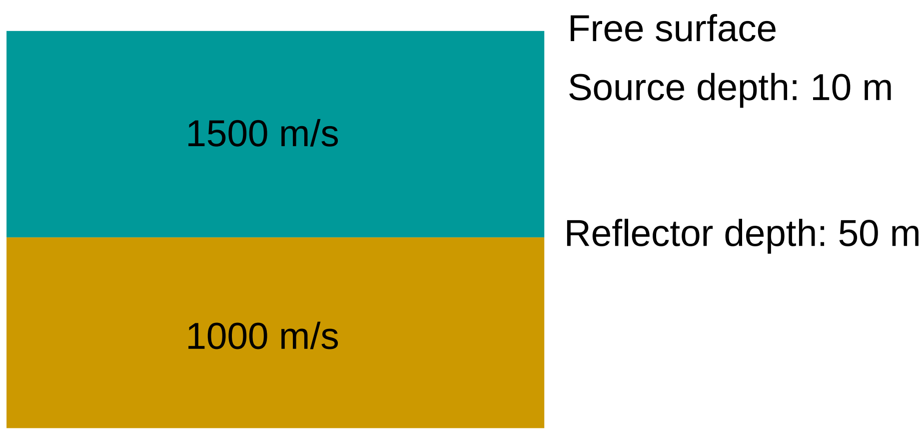

Figure 2.14: Velocity model and source position.

(1) on **horizontal** M.S. and then do deghosting (using Equation (2.35) and Equation (2.36)),

(2) on **inclined** M.S. and then do deghosting, with assuming that the M.S. is horizontal in deghosting (using Equation (2.35) and Equation (2.36)), and

(3) on **undulated** M.S. and then do deghosting, with firstly assuming that the M.S. is horizontal in deghosting (using Equation (2.35) and Equation (2.36)) and with accommodation of the topography of M.S. in deghosting (using Equation (2.35) and Equation (2.38)).

2.3.5.1 Flat measurement surface

Figure 2.15(a) shows the total wave generated at constant depth 35 m. We can see the primary, free surface mutiple and ghosts interfere with each other, especially at far offset. Figure 2.16(a) shows the receiver deghosting result at 15 m depth using Equation (2.36), with Figure 2.15(a) as input. Figure 2.17(a) shows the source deghosting result using Equation (2.35), with Figure 2.17(a) as input. We can see

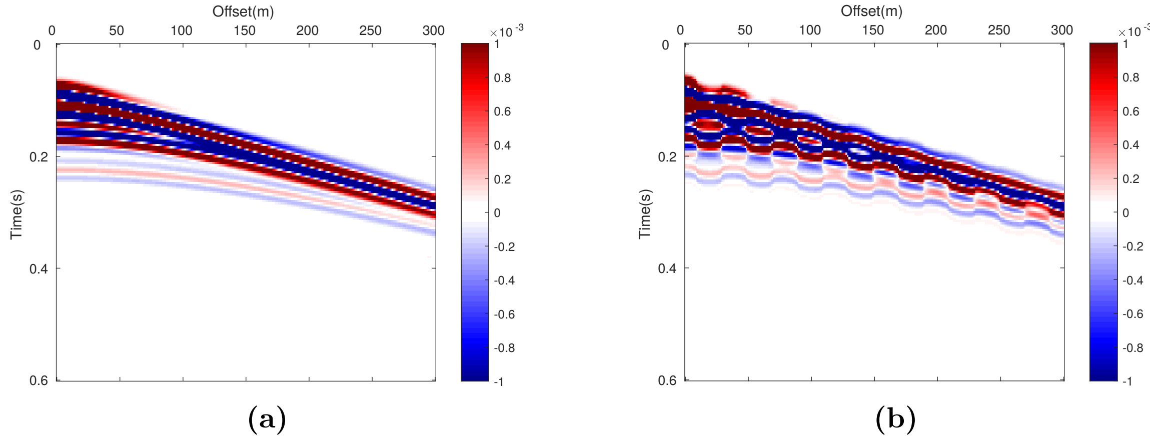

Figure 2.15: Data generated by the Cagniard-de Hoop method on different measurement surface (M.S.). **(a)** Horizontal M.S. at depth of 35 m, and **(b)** undulated M.S. with minimum depth of 25 m and maximum depth of 45 m. Colorbar on the right represents the amplitude.

clearly two events of opposite polarity which are the primary and free surface multiple, respectively.

2.3.5.2 Inclined measurement surface

Figure 2.16(b) shows the receiver deghosting result at 15 m depth, using data generated on 2° M.S. but assuming it's horizontal M.S. in deghosting (Equation (2.36)). Figure 2.17(b) shows the source deghosting result using Equation (2.35), with Figure 2.16(b) as input. We can hardly see any difference between Figure 2.17(a) and Figure 2.17(b). To see clearly the effectiveness of Figure 2.17(a) and Figure 2.17(b) so that we know the impact of the inclination of M.S., Figure 2.18(a) show the comparison in one trace between perfect deghosted data generated by the Cagniard-de Hoop method (which is primary and free surface multiple) and actual deghosted results that assumes horizontal M.S. in deghosting. We can see the deghosting result (—)

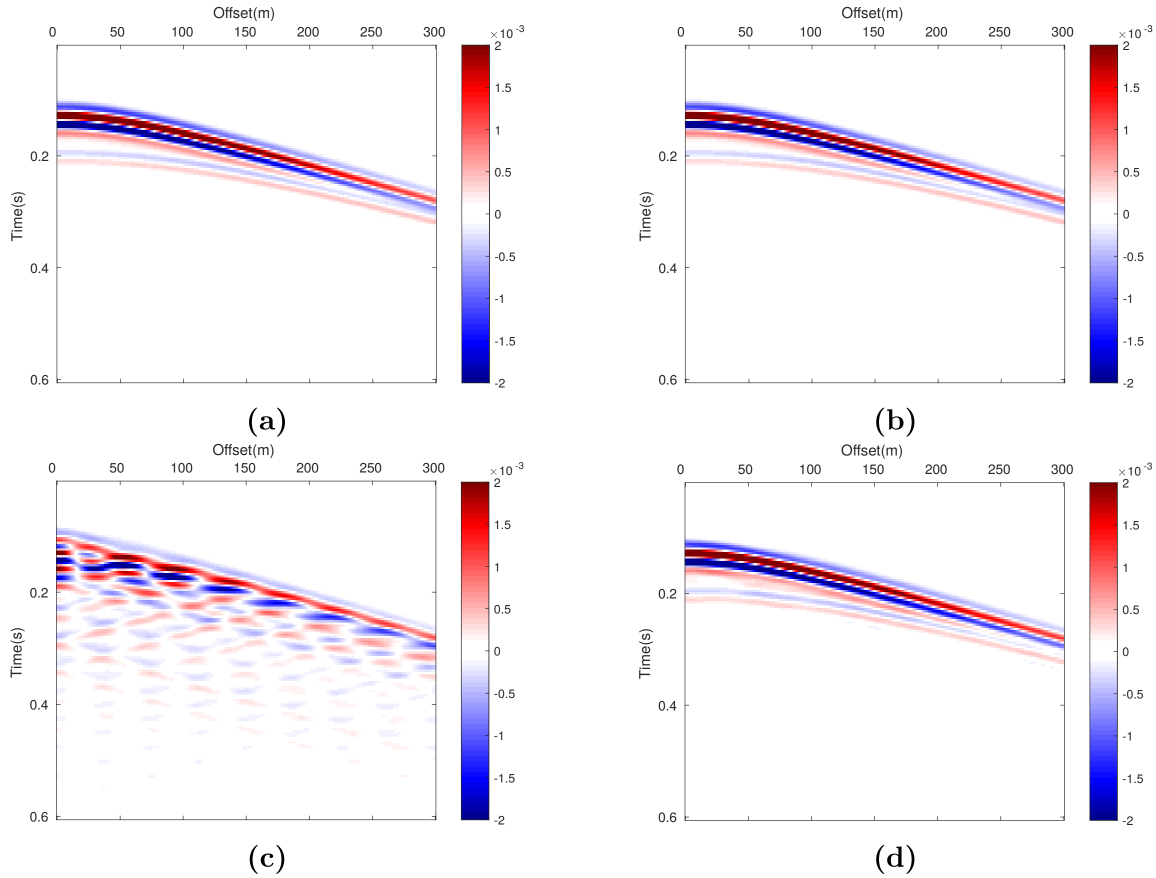

(a)

(b)

(c)

(d)

Figure 2.16: Receiver deghosting result at 15 m depth. **(a)** M.S. is actually horizontal, **(b)** M.S. is 2° inclined, assuming it's horizontal in deghosting, **(c)** M.S. is undulated, assuming it's horizontal in deghosting, and **(d)** M.S. is undulated, with accommodation in deghosting. Colorbar on the right represents the amplitude.

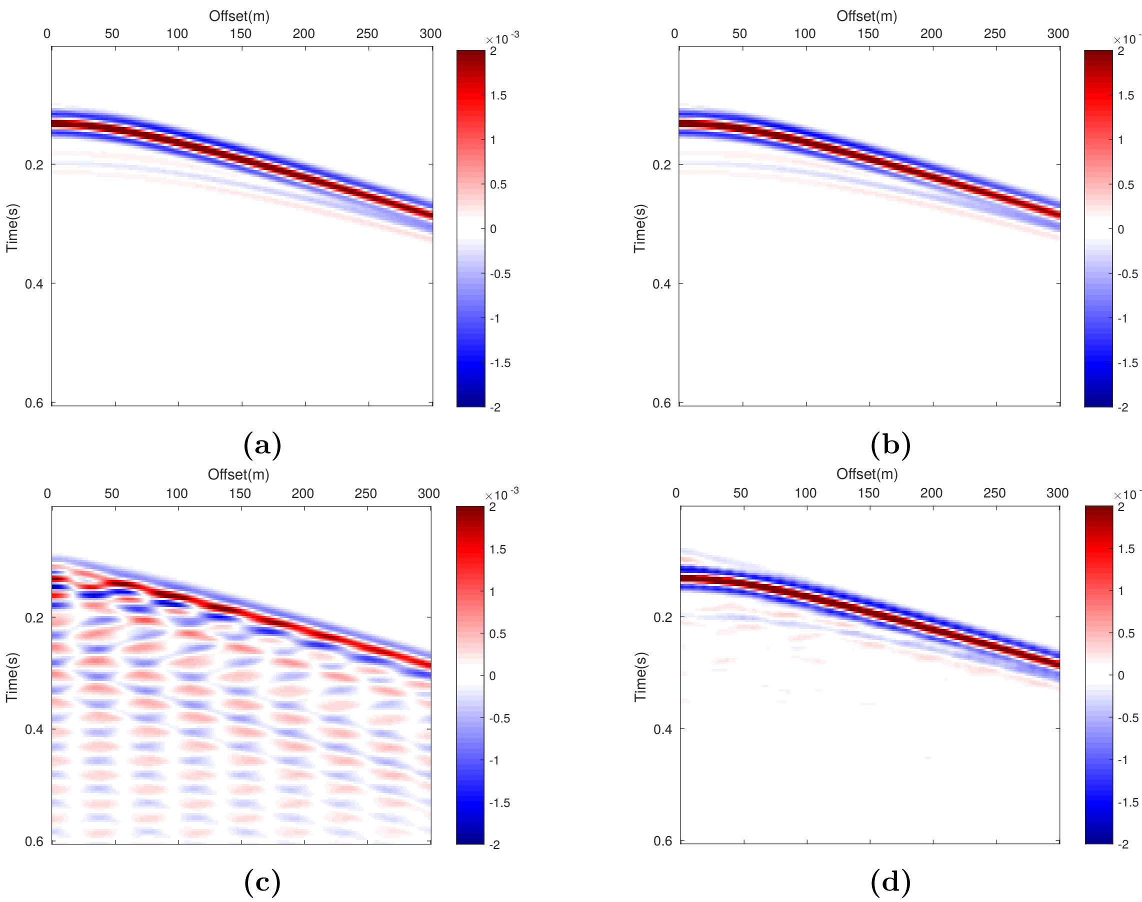

Figure 2.17: Source deghosting result, using receiver deghosting results Figure 2.16 as input. **(a)** Using Figure 2.16(a) as input, **(b)** Figure 2.16(b) as input, **(c)** Figure 2.16(c) as input, and **(d)** Figure 2.16(d) as input. Colorbar on the right represents the amplitude.

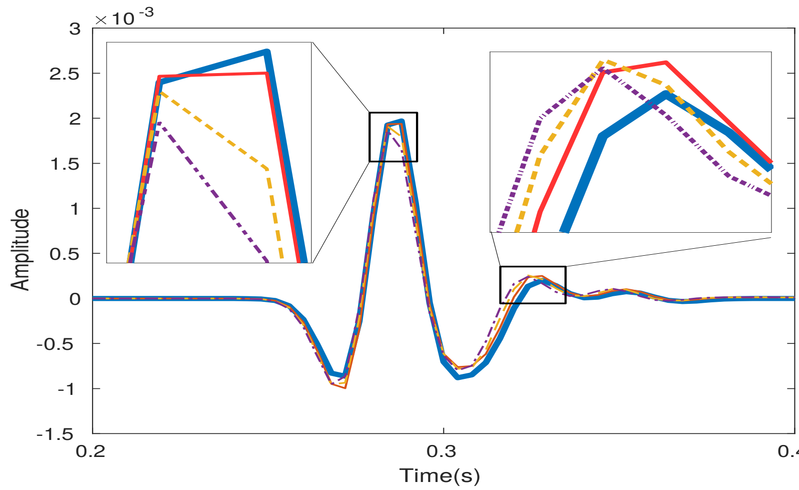

(a)

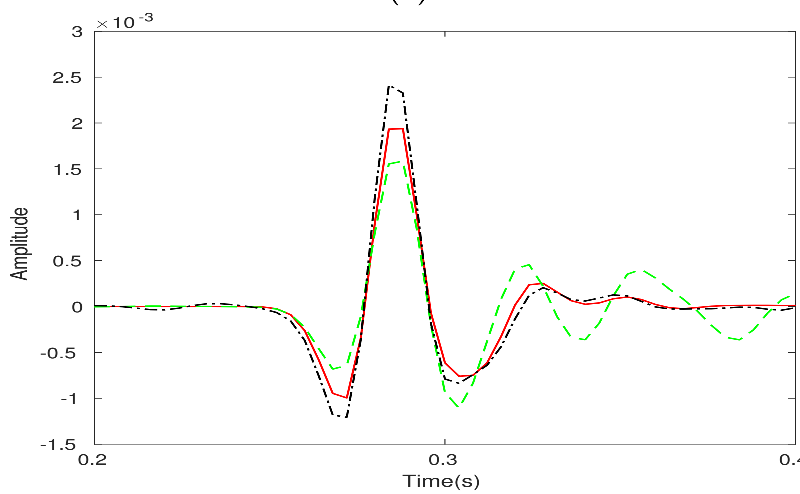

(b)

Figure 2.18: Traceplot of source and receiver deghosting data predicted at 15 m depth. **(a)** Traceplot (offset=300 m) comparison of actual primary and free surface multiple (generated by the Cagniard-de Hoop method) at 15 m depth (▬), deghosted result (Figure 2.17(a)) using total wave generated on horizontal M.S. (—), deghosted result using total wave generated on 1° inclined M.S. assuming it's horizontal in deghosting (- - -) and deghosted result (Figure 2.17(b)) using total wave generated on 2° inclined M.S. assuming it's horizontal in deghosting (-· · · · · -), and
(b) traceplot (offset=300 m) comparison of deghosted result (Figure 2.17(a)) using total wave generated on horizontal M.S. (—), deghosted result (Figure 2.17(c)) using total wave generated on undulated M.S. assuming it's horizontal in deghosting (- - -) and deghosted result (Figure 2.17(d)) using total wave generated on undulated M.S. with accommodation of the M.S.'s topography in deghosting (- · · - · -).

using actually horizontal M.S. is very close to perfect. This means the deghosting method itself for actually horizontal M.S. (Equation (2.36) and Equation (2.35)) is very effective. Also we can see the result using 1° inclined M.S. (- - -) deviates only a little from it (—) and the result using 2° inclined M.S. (- · · · · - -) just deviates a little more. This means that although the assumption of horizontal M.S. in deghosting can bring deviation from perfect deghosted data, such deviation is very slight when the M.S. is close to horizontal.

2.3.5.3 Undulating measurement surface

Figure 2.15(b) shows the total wave generated on periodically undulated M.S. with miminum depth 25 m and maximum depth 45 m. And undulation period is 40 m. Figure 2.16(c) shows the receiver deghosting result at 15 m depth using Figure 2.15(b) as input, assuming the M.S. is horizontal (Equation (2.36)). Figure 2.17(c) shows the source deghosting result using Figure 2.16(c) as input, with Equation (2.35). We can see many periodical artifacts.

Figure 2.16(d) shows the receiver deghosting result using Figure 2.15(b) as input, while accommodating the topography of M.S. (Equation (2.38)). And Figure 2.17(d) shows the source deghosting result using Figure 2.16(d) as input, with Equation (2.35). Almost all artifacts disappear and the result is close to Figure 2.17(a).

Figure 2.18(b) compares a trace (offset=300 m) of Figure 2.17(a), Figure 2.17(c) and Figure 2.17(d). We can see the result (- - -) using Equation (2.35) and (2.36) fails when the M.S. has obvious undulation. In contrast, with accommodation of the topography of undulated M.S., the result (- · - · -) using Equation (2.35) and (2.38) retains the effectiveness of result (—) of which the M.S. is originally horizontal.

2.4 Conclusions

Green's theorem P_0/P_s separation and deghosting algorithms are developed and tested for depth-variable towed streamers. This is relevant for ocean-bottom preprocessing when the ocean bottom is nonflat, and for on-shore preprocessing since the earth's surface can have significant lateral variability. Numerical examples show that if data are acquired on a non-horizontal measurement surface (M.S.), the constant depth assumption can provide effective preprocessing results when the M.S. is close to horizontal. If the M.S. deviates significantly from horizontal, the conventional preprocessing method that assumes a horizontal M.S. may lead to an inaccurate result. In the latter case, the Green's theorem preprocessing formula proposed in this paper can provide effective preprocessing results, by incorporating the topography of the M.S.. This is important for subsequent processing including multiple removal. This step, the Green's theorem preprocessing for towed streamer data, can be extended and utilized for on-shore and ocean-bottom acquisition, where the M.S. can at times be far from horizontal.

Chapter 3

ISS free surface multiple elimination

3.1 Introduction

Free surface multiple elimination (FSME) based on inverse scattering series (ISS) has been successfully applied to synthetic and field data. While subsurface information is not required by FSME, knowledge about the nature of acquisition is needed to achieve effectiveness. This chapter does several numerical tests to analyze the impact caused by assuming horizontal acquisition in preprocessing (deghosting), on FSME that has been currently formulated with horizontal acquisition assumption. In numerical tests, the velocity model, as shown by Chapter 2, has a free surface and one horizontal reflector so internal multiples are not considered in this chapter. Numerical tests show that when the original measurement surface (M.S.) is close to horizontal, the assumption of horizontal acquisition in preprocessing doesn't bring obvious artifacts in FSME; however, when the M.S. undulates significantly, FSME is undermined by ineffective preprocessing with horizontal acquisition assumption which is now inappropriate. To solve this problem, the last set of numerical tests shows the result with accommodation of the M.S.'s undulation in preprocessing, which is very effective.

3.2 Theory

3.2.1 Inverse scattering series

In this subsection, I will provide a brief review of the forward scattering series and inverse scattering series following Weglein et al. (2003). The scattering theory relates the difference between the wavefield P in the actual medium and the wavefield in the reference medium, to the difference between the properties of actual medium and reference medium. In terms of wave equations that govern seismic wave propagation in actual medium and reference medium, we can rewrite Equation (2.4) and Equation (2.5) in a general operator form as (Weglein et al., 2003)

$$LP = \delta \tag{3.1}$$

$$L_0 G_0 = \delta \tag{3.2}$$

where L and L_0 represent the differential operator in the actual medium and reference medium, respectively. And G and G_0 are the corresponding actual Green's function and reference Green's function, respectively. δ represents an impulsive source. The perturbation operator V and the scattered field operator Ψ_s are defined as follows

$$V \equiv L_0 - L \tag{3.3}$$

$$\Psi_s \equiv G - G_0 \tag{3.4}$$

The Lippmann-Schwinger equation as the fundamental equation of scattering theory relates Ψ_s, G_0, V and G

$$\Psi_s = G - G_0 = G_0 V G \tag{3.5}$$

Expanding Equation (3.5) in an infinite series through a substitution of higher order approximations for G in the right hand side, the forward scattering series can be derived

$$\begin{aligned} \Psi_s = G - G_0 &= G_0 V G_0 + G_0 V G_0 V G_0 + ... \\ &= (\Psi_s)_1 + (\Psi_s)_2 + ... \end{aligned} \tag{3.6}$$

where $(\Psi_s)_n \equiv G_0(VG_0)^n$ is the portion of Ψ_s that is nth order in V. The relationship (3.6) provides a Geometric forward series rather than a Taylor series. In general, a Taylor series doesn't have an inverse series, whereas a Geometric series has an inverse series. This enables inverse scattering series to provide a direct method to solve for V, the subsurface information, from the recorded reflection data at the earth surface $D = (\Psi_s)_{m.s.}$. To do that, first write the perturbation V as a series

$$V = V_1 + V_2 + V_3 + ... \tag{3.7}$$

where V_i is the portion of V that is ith order in the data $D = (\Psi_s)_{m.s.}$. Substituting Equation (3.7) into Equation (3.5), we have

$$\begin{aligned}\Psi_s = &G_0(V_1 + V_2 + ...)G_0 \\ &+ G_0(V_1 + V_2 + ...)G_0(V_1 + V_2 + ...)G_0 \\ &+ G_0(V_1 + V_2 + ...)G_0(V_1 + V_2 + ...)G_0(V_1 + V_2 + ...)G_0 \\ &+ ...\end{aligned} \tag{3.8}$$

By evaluating both sides on the measurement surface and setting terms of equal order in the data equal, we can have a series of equations, i.e., the inverse scattering series

$$(\Psi_s)_{m.s.} = D = (G_0V_1G_0)_{m.s.} \tag{3.9}$$

$$(G_0V_2G_0)_{m.s.} = -(G_0V_1G_0V_1G_0)_{m.s.} \tag{3.10}$$

$$(G_0V_3G_0)_{m.s.} = -(G_0V_1G_0V_1G_0V_1G_0)_{m.s.} - (G_0V_1G_0V_2G_0)_{m.s.} - (G_0V_2G_0V_1G_0)_{m.s.} \tag{3.11}$$

$$...... \tag{3.12}$$

Since $(\Psi_s)_{m.s.}$ is the measured scattered wavefield and G_0 can be calculated from the reference medium, V_1 can be solved directly from Equation (3.9), giving the linear portion of the perturbation in terms of data. With V_1, Equation (3.10) can be solved for V_2, and likewise for the higher terms V_i.

In summary, through Equation (3.9) - Equation (3.12), the perturbation $V = V_1 + V_2 + V_3 + ...$ can be found directly using the scattered wavefield on the measurement surface and the information of reference medium, without appealing to earth model type (acoustic, elastic, anelastic, ...) and subsurface information (Weglein et al., 1997, 2003).

3.2.2 Task-specific inverse scattering sub-series

The first application of the inverse scattering series to seismic exploration employed a sub-series to perform free surface multiple removal (Carvalho et al., 1991, 1992; Carvalho, 1992). Towards the ultimate goal of identifying earth material properties, a combination of factors led to imagining-inversion in terms of steps or stages with intermediate objectives (Weglein et al., 2003). Each stage has been defined as achieving a task or objective: (1) removing free surface multiples; (2) removing internal multiples; (3) locating and imaging reflectors in space; (4) determining the changes in earth material properties across those reflectors.

To perform each step, it is necessary to identify the terms and formulate a sub-series responsible for a specific task within the entire series. The rationale for seeking and methods of identifying uncoupled task-specific subseries was first presented by Weglein et al. (2003). After performing a sub-task, the problem is restarted with the processed data as the new input for the next stage. The methodology of restarting the problem meets the requirements of each sub-series and has proven to be very efficient within the ISS technique.

3.2.3 ISS free surface multiple elimination

If we choose the reference medium to be half space of air and half space of water (Figure 3.1(b)), whose property is the same as the actual medium (Figure 3.1(a)) along the measurement surface, the Green's function for the reference medium consists of two terms (Figure 3.1(c))

$$G_0 = G_0^d + G_0^{FS} \tag{3.13}$$

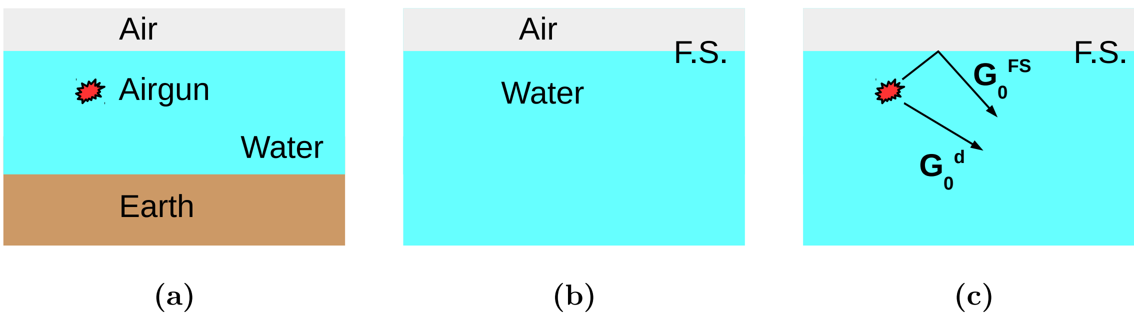

Figure 3.1: (a) Actual medium and experiment, (b) reference medium of half water and half air, and (c) reference Green's function $G_0 = G_0^d + G_0^{FS}$ which is a direct term plus a free surface reflected term.

The first term represents the direct arrival and the second represents the reflection at the free surface. Substituting G_0 into the ISS equations, the first three terms are

$$D = \{(G_0^d + G_0^{FS})V_1(G_0^d + G_0^{FS})\}_{M.S.} \tag{3.14}$$

$$0 = \{(G_0^d + G_0^{FS})V_2(G_0^d + G_0^{FS}) \tag{3.15}$$
$$+ (G_0^d + G_0^{FS})V_1(G_0^d + G_0^{FS})V_1(G_0^d + G_0^{FS})\}_{M.S.}$$

$$0 = \{(G_0^d + G_0^{FS})V_3(G_0^d + G_0^{FS}) + (G_0^d + G_0^{FS})V_1(G_0^d + G_0^{FS})V_2(G_0^d + G_0^{FS}) \tag{3.16}$$
$$+ (G_0^d + G_0^{FS})V_2(G_0^d + G_0^{FS})V_1(G_0^d + G_0^{FS})$$
$$+ (G_0^d + G_0^{FS})V_1(G_0^d + G_0^{FS})V_1(G_0^d + G_0^{FS})V_1(G_0^d + G_0^{FS})\}_{M.S.}$$

Firstly, any ghost-generating terms should be excluded. Since ghosts refers to any event that goes directly from the source to the free surface and/or arrives at the receiver right after hitting the free surface, deghosting selects terms that begin and end with only G_d, i.e., $G_0^d V_i G_0^{FS/d} V_j G_0^d$. After deghosting, any event that hits the free surface is a free surface multiple. To further remove the free surface multiple, the sub-series for FSME select terms that contain only G_0^{FS} between V_i and V_j. That is, the FSME ISS sub-series are

$$D_1' = \{G_0^d V_1 G_0^d\}_{M.S.} \tag{3.17}$$

$$\{G_0^d V_2' G_0^d\}_{M.S.} = -\{G_0^d V_1 G_0^{FS} V_1 G_0^d\}_{M.S.} \tag{3.18}$$

$$\{G_0^d V_3' G_0^d\}_{M.S.} = \tag{3.19}$$
$$-\{G_0^d V_1 G_0^{FS} V_2' G_0^d\}_{M.S.} - \{G_0^d V_2' G_0^{FS} V_1 G_0^d\}_{M.S.} - \{G_0^d V_1 G_0^{FS} V_1 G_0^{FS} V_1 G_0^d\}_{M.S.}$$

$$...... \tag{3.20}$$

where D_1' represents the deghosted data. Based on the recursive relationship between consecutive orders of V' (V_1,V_2',V_3',...), consecutive orders of D', which is the data with free surface multiple eliminated, can be computed recursively. That is,

$$\begin{aligned} D' &= G_0^d V' G_0^d \\ &= G_0^d (V_1 + V_2' + V_3' + ...) G_0^d \\ &= G_0^d V_1 G_0^d + G_0^d V_2' G_0^d + G_0^d V_3' G_0^d + ... \\ &= D_1' + D_2' + D_3' + ... \end{aligned} \tag{3.21}$$

Notice that Equation (3.17) expresses V_1 explicitly in terms of the deghosted data. In the integral form, it can be written as

$$D_1'(\mathbf{r}_g, \mathbf{r}_s; \omega) = \int_\infty d\mathbf{r}_1 \int_\infty d\mathbf{r}_2 G_0^d(\mathbf{r}_g, \mathbf{r}_1; \omega) V_1(\mathbf{r}_1, \mathbf{r}_2; \omega) G_0^d(\mathbf{r}_2, \mathbf{r}_s; \omega) \tag{3.22}$$

where $\mathbf{r}_g = (x_g, y_g, z_g)$ and $\mathbf{r}_s = (x_s, y_s, z_s)$ are the receiver and source location, respectively. $V_1(\mathbf{r}_1, \mathbf{r}_2; \omega)$ is the general form of the perturbation operator V_1. Its degree of spatial freedom are needed to describe potential angle dependent reflectivity and anisotropic effects as function of position. Stolt and Weglein gave a detailed explanation on the form of V_1 in , but the most recent and revised version of the explanation on the form of V_1 can be found in Weglein et al. (2003).

In three dimensions, Equation (3.22) becomes

$$\begin{aligned} &D_1'(x_g, y_g, z_g, x_s, y_s, z_s; \omega) = \\ &\int_{-\infty}^{\infty} dx_1 \int_{-\infty}^{\infty} dy_1 \int_{-\infty}^{\infty} dz_1 \int_{-\infty}^{\infty} dx_2 \int_{-\infty}^{\infty} dy_2 \int_{-\infty}^{\infty} dz_2 \\ &G_0^d(x_g, y_g, z_g, x_1, y_1, z_1; \omega) V_1(x_1, y_1, z_1, x_2, y_2, z_2; \omega) G_0^d(x_2, y_2, z_2, x_s, y_s, z_s; \omega) \end{aligned} \tag{3.23}$$

After Fourier transform over x_g,y_g,x_s, and y_s

$$D'_1(k_{xg}, k_{yg}, z_g, k_{xs}, k_{ys}, z_s; \omega) = \tag{3.24}$$
$$\int_{-\infty}^{\infty} dx_1 \int_{-\infty}^{\infty} dy_1 \int_{-\infty}^{\infty} dz_1 \int_{-\infty}^{\infty} dx_2 \int_{-\infty}^{\infty} dy_2 \int_{-\infty}^{\infty} dz_2$$
$$G_0^d(k_{xg}, k_{yg}, z_g, x_1, y_1, z_1; \omega) V_1(x_1, y_1, z_1, x_2, y_2, z_2; \omega) G_0^d(x_2, y_2, z_2, k_{xs}, k_{ys}, z_s; \omega)$$

Based on the linear relationship between D'_1 and V_1 and recursive relationship between V'_n (Equation (3.17)-Equation (3.20)), the Carvalho's famous recursive equation for FSME sub-series (Carvalho et al., 1992; Carvalho, 1992; Weglein et al., 1997, 2003)) can be derived

$$D'_n(k_{xg}, k_{yg}, z_g, k_{xs}, k_{ys}, z_s; \omega) = \frac{1}{2i\pi^2 \rho_0 A(\omega)} \tag{3.25}$$
$$\int_{-\infty}^{\infty} \int_{-\infty}^{\infty} dk_x dk_y e^{iq(z_g+z_s)} D'_1(k_{xg}, k_{yg}, z_g, k_x, k_y, z_s; \omega) q D'_{n-1}(k_x, k_y, z_g, k_{xs}, k_{ys}, z_s; \omega)$$

for $n \leq 2$ and

$$D'(k_{xg}, k_{yg}, z_g, k_{xs}, k_{ys}, z_s; \omega) = \sum_{n=1}^{\infty} D'_n(k_{xg}, k_{yg}, z_g, k_{xs}, k_{ys}, z_s; \omega) \tag{3.26}$$

Here $D'_1(k_{xg}, k_{yg}, z_g, k_{xs}, k_{ys}, z_s; \omega)$ is the input preprocessed data $D'_1(x_g, y_g, z_g, x_s, y_s, z_s; \omega)$ in wavenumber-frequency domain. $A(\omega)$ and ρ_0 are source signature and reference medium density, respectively. $q = \sqrt{\frac{\omega}{c_0} - k_x^2 - k_y^2}$ is the vertical wavenumber and c_0 is reference medium velocity. D'_n is inverse scattering subseries calculated by D'_1 and D' is the output data with FSM eliminated. Since the Formula (3.25) is in wavenumber domain, currently the ISS FSME algorithm requires the input preprocessed data to be collected at a horizontal surface. If preprocessed data are collected at a non-horizontal surface, it can be rearranged at a horizontal surface through wavefield prediction.

3.3 1D analytic example

Suppose the data after deghosting include,

primary from the water bottom

$$P^{pri} = e^{ik(z_{wb}-z_s)} R e^{i(-k)(z_g-z_{wb})} = Re^{2ikz_{wb}} \tag{3.27}$$

1st order free surface multiple

$$P^{1stFSM} = \frac{e^{ik(z_{wb}-z_s)}}{2ik} R e^{i(-k)(0-z_{wb})} (-1) e^{ik(z_{wb}-0)} R e^{i(-k)(z_g-z_{wb})} = (-R^2) e^{4ikz_{wb}} \tag{3.28}$$

2nd order free surface multiple

$$\begin{aligned} &P^{1stFSM} \\ &= \frac{e^{ik(z_{wb}-z_s)}}{2ik} R e^{i(-k)(0-z_{wb})} (-1) e^{ik(z_{wb}-0)} R e^{i(-k)(0-z_{wb})} (-1) e^{ik(z_{wb}-0)} R e^{i(-k)(z_g-z_{wb})} \\ &= R^3 e^{6ikz_{wb}} \end{aligned} \tag{3.29}$$

......

nth order free surface multiple

$$P^{nthFSM}(z_g, z_s; \omega) = (-1)(-R)^{n+1} e^{2(n+1)ikz_{wb}} \tag{3.30}$$

and higher order free surface mutiples. Here we assume $z_g = z_s = 0$. The input total wave is,

$$\begin{aligned} D'_1 &= P^{pri}(z_g, z_s; \omega) + P^{1stFSM}(z_g, z_s; \omega) + ... + P^{nthFSM}(z_g, z_s; \omega) + ... \\ &= Re^{2ikz_{wb}} + (-R^2)e^{4ikz_{wb}} + (R^3)e^{6ikz_{wb}} + ... + (-1)(-R)^{n+1} e^{2(n+1)ikz_{wb}} + ... \\ &= \frac{Re^{2ikz_{wb}}}{1 + Re^{2ikz_{wb}}} \end{aligned} \tag{3.31}$$

In the case of 1D normal incidence, Equation (3.26) reduce to (Weglein et al., 2003),

$$D' = D'_1 + D'^2_1 + D'^3_1 + ... + D'^n_1 + ... = \frac{D'_1}{1 - D'_1} = \frac{\frac{Re^{2ikz_{wb}}}{1+Re^{2ikz_{wb}}}}{1 - \frac{Re^{2ikz_{wb}}}{1+Re^{2ikz_{wb}}}} = Re^{2ikz_{wb}} \quad (3.32)$$

This is exactly Equation (3.27).

3.4 Numerical tests

Figure 3.2 shows FSME results of deghosted data in Figure 2.17(a)-Figure 2.17(c), using Formula (3.25) and (3.26). From Figure 3.2(a)-3.2(d), we can see that FSME of deghosting data, which has the horizontal M.S. assumption in deghosting, is effective when the original M.S. is actually horizontal or when it's just slightly inclined. This is also shown by Figure 3.3. We can see the predicted FSM using horizontal M.S. (—) is very close to actual FSM (- - -). The result of 1° M.S. (· · · ·) deviates very little and the result of 2 degree M.S. (· - · -) just deviates a little more.

However, as shown by Figure 3.2(e) and 3.2(f), the ineffectiveness of deghosting (Figure 2.17(c)) that assumes the M.S. is horizontal when it's actually undulated contaminates the subsequent FSME. As shown by Figure 3.4, FSME benefits from the effectiveness of deghosting (Figure 2.17(d)) with accommodation of the topography of M.S.. Figure 3.5 shows more clear comparison in trace. We can see the predicted primary with accommodation of the acquisition undulation in deghosting is very close to the predicted primary with actually horizontal acquisition.

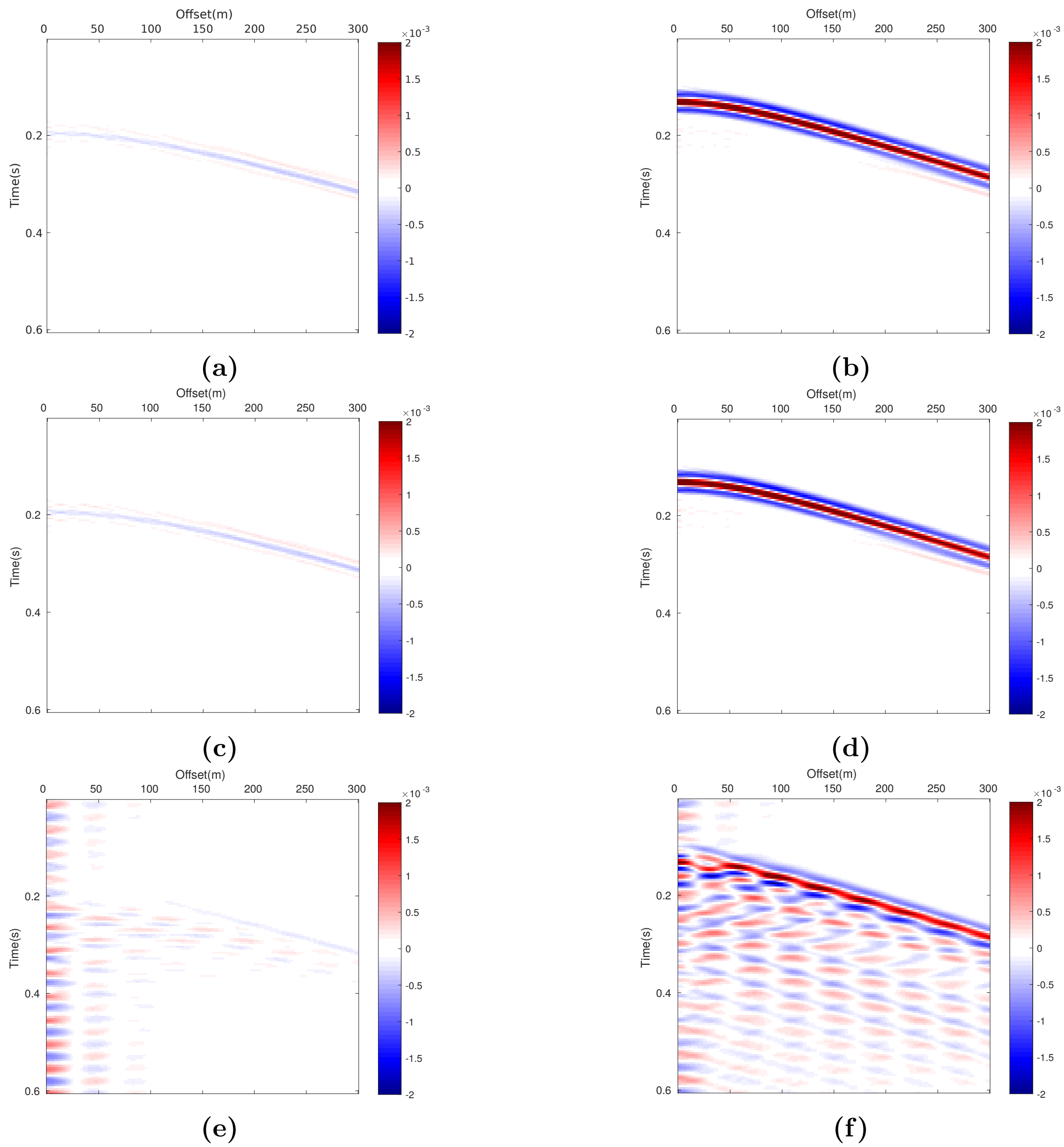

Figure 3.2: Predicted free surface multiple (FSM) (left) using Figure 2.17 as input and primary (right) after subtracting the predicted FSM from Figure 2.17. **(a)** Predicted FSM from deghosted data Figure 2.17(a), **(b)** subtraction of Figure 3.2(a) from Figure 2.17(a), **(c)** predicted FSM from deghosted data Figure 2.17(b), **(d)** subtraction of Figure 3.2(c) from Figure 2.17(b), **(e)** predicted FSM. from deghosted data Figure 2.17(c), and **(f)** subtraction of Figure 3.2(e) from Figure 2.17(c). Colorbar on the right represents the amplitude.

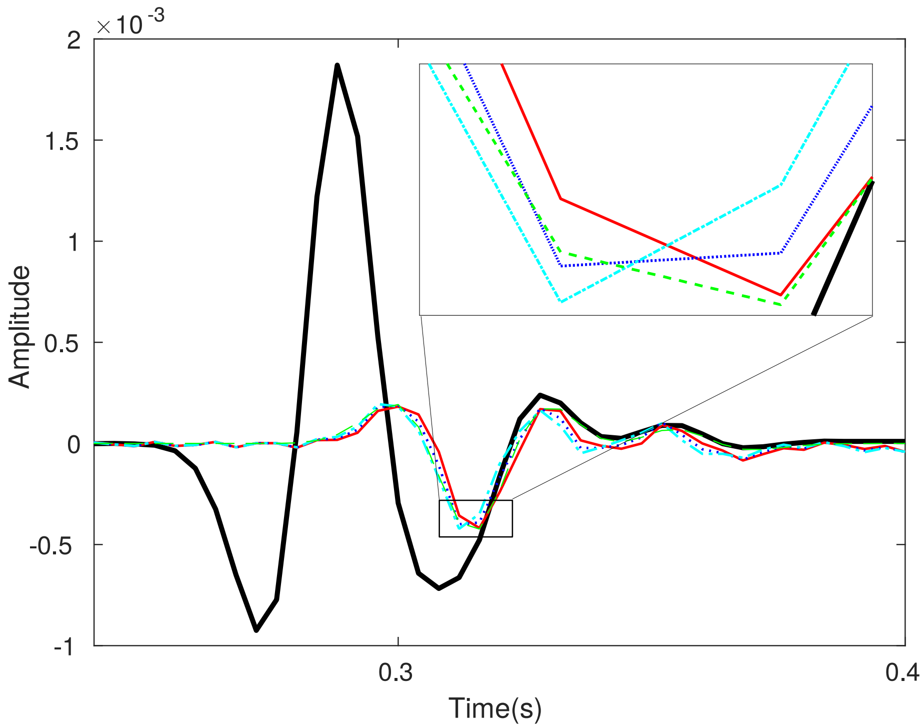

Figure 3.3: Comparison of deghosted data (Figure 2.17(a)) at 15 m depth (▬), actual FSM (generated by the Cagniard-de Hoop method) at 15 m depth (- - -), predicted FSM (Figure 3.2(a)) using the deghosted result of total wave generated on horizontal M.S. (—), predicted FSM using the deghosted result of total wave generated on 1° M.S. while assuming it's horizontal in deghosting(·····) and predicted FSM (Figure 3.2(c)) using the deghosted result of total wave generated on 2° M.S. while assuming it's horizontal in deghosting (·-·-).

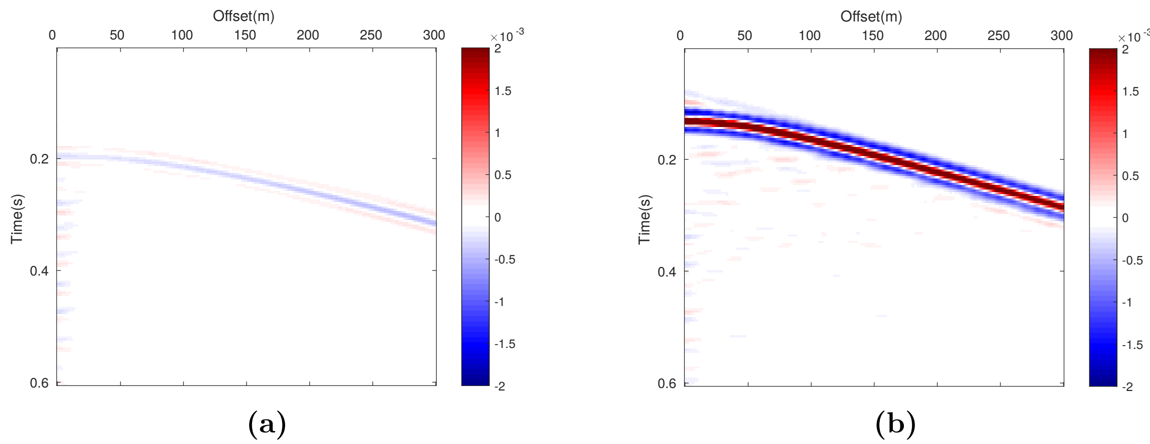

Figure 3.4: **(a)** Predicted free surface multiple (FSM) from deghosted data Figure 2.17(d), and **(b)** subtraction of Figure 3.4(a) from Figure 2.17(d). Colorbar on the right represents the amplitude.

3.5 Conclusions

This chapter tests the impact that the assumption of horizontal acquisition in deghosting could bring to free surface multiple elimination (FSME) whose effectiveness is based on the effectiveness of deghosting. From numerical examples, we see that when the acquisition is horizontal, FSME of deghosted data is very effective. When the M.S. is inclined, the FSME retains capability for 2 degree inclination angle though the deghosting assumes the M.S. is horizontal. However, when the M.S. undulates, assuming it's horizontal in deghosting is inappropriate and undermines subsequent FSME. The impact of such assumption is avoided in the section 3.4, where the FSME uses the preprocessed data from deghosting that accommodates the topography of the M.S..

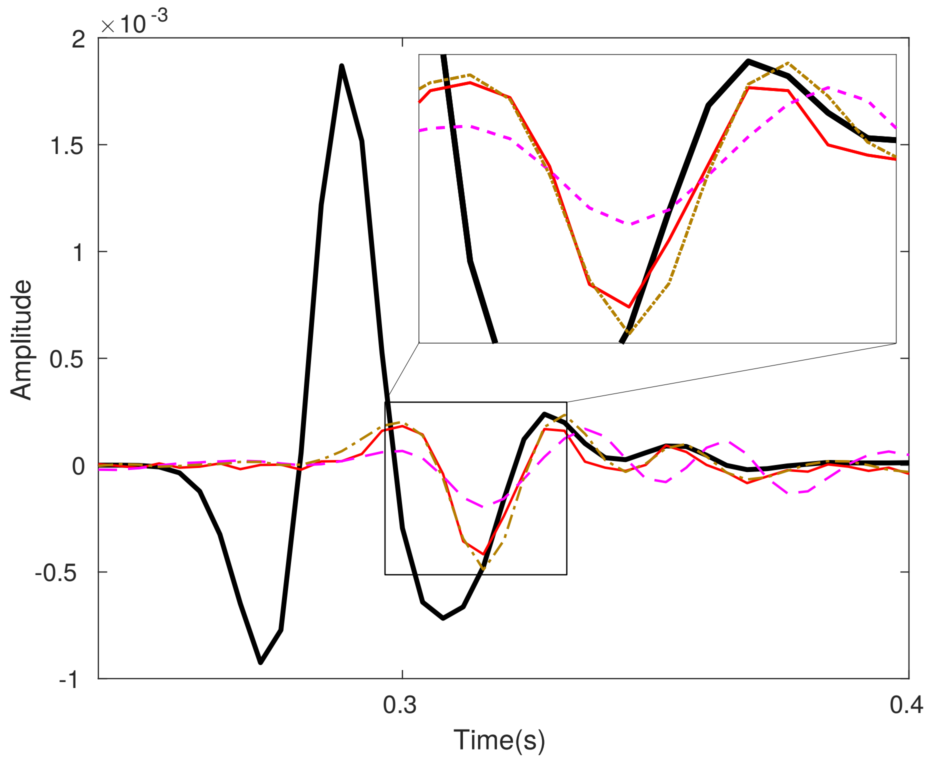

Figure 3.5: Comparison of deghosted data (Figure 2.17(a)) at 15 m depth (▬), predicted FSM (Figure 3.2(a)) using the deghosted result of total wave generated on horizontal M.S. (—), predicted FSM (Figure 3.2(e)) using the deghosted result of total wave generated on undulated M.S. while assuming it's horizontal in deghosting (- - -), and predicted FSM (Figure 3.4(a)) using the deghosted result of total wave generated on undulated M.S. with accommodation of its topography in deghosting (· - · -).

Chapter 4

Stolt CIII Imaging

In this chapter, we do analytical and numerical examples of Stolt CIII imaging that uses the data that have gone through preprocessing in Chapter 2 and free surface multiple elimination in Chapter 3. The reason we choose Stolt CIII imaging is that, in the new imaging method from M-OSRP, both the imaging condition and method of implementation are equally effective at all frequencies at the target and reservoir (Weglein, 2016a).

4.1 Theory

Consider the physical wavefield and Green's function in the $(\mathbf{r};\omega)$ domain that satisfy, respectively

$$(\nabla^2 + k^2)P(\mathbf{r};\omega) = \rho(\mathbf{r};\omega) \tag{4.1}$$

$$(\nabla^2 + k^2)G_0(\mathbf{r},\mathbf{r}';\omega) = \delta(\mathbf{r}-\mathbf{r}') \tag{4.2}$$

where $k = \omega/c$. Here we assume 3D wave propagation and the velocity c is a constant. ρ is a general source, i.e., it represents both active sources (air guns, dynamite, vibrator trucks) and passive sources (heterogeneities in the earth). According to the Lippmann-schwinger equation, the causal solution to Equation (4.1) is

$$P(\mathbf{r};\omega) = \int_{\infty} \rho(\mathbf{r}';\omega) G_0^{+}(\mathbf{r},\mathbf{r}';\omega) d\mathbf{r}' \tag{4.3}$$

On the other hand, as chapter 2 shows, the Green's second identity gives,

$$\begin{aligned} &\int_V \Big[P(\mathbf{r}';\omega)\nabla'^2 G_0(\mathbf{r}',\mathbf{r};\omega) - G_0(\mathbf{r}',\mathbf{r};\omega)\nabla'^2 P(\mathbf{r}';\omega)\Big] d\mathbf{r}' \\ &= \oint_S \Big[P(\mathbf{r}';\omega)\nabla' G_0(\mathbf{r}',\mathbf{r};\omega) - G_0(\mathbf{r}',\mathbf{r};\omega)\nabla' P(\mathbf{r}';\omega)\Big] \cdot d\mathbf{S}' \end{aligned} \tag{4.4}$$

Substituting $\nabla'^2 P(\mathbf{r}';\omega) = \rho(\mathbf{r}';\omega) - k^2 P(\mathbf{r}';\omega)$ and $\nabla'^2 G_0(\mathbf{r}',\mathbf{r};\omega) = \delta(\mathbf{r}'-\mathbf{r}) - k^2 G_0(\mathbf{r}',\mathbf{r};\omega)$ into it, we have

$$\begin{aligned} &\int_V P(\mathbf{r}';\omega)\delta(\mathbf{r}'-\mathbf{r}) d\mathbf{r}' \\ &= \int_V \rho(\mathbf{r}';\omega) G_0(\mathbf{r}',\mathbf{r};\omega) d\mathbf{r}' + \oint_S \Big[P(\mathbf{r}';\omega)\nabla' G_0(\mathbf{r}',\mathbf{r};\omega) - G_0(\mathbf{r}',\mathbf{r};\omega)\nabla' P(\mathbf{r}';\omega)\Big] \cdot d\mathbf{S}' \end{aligned} \tag{4.5}$$

Therefore, for $\mathbf{r}$ in V

$$\begin{aligned} &P(\mathbf{r};\omega) \\ &= \int_V \rho(\mathbf{r}';\omega) G_0(\mathbf{r}',\mathbf{r};\omega) d\mathbf{r}' + \oint_S \Big[P(\mathbf{r}';\omega)\nabla' G_0(\mathbf{r}',\mathbf{r};\omega) - G_0(\mathbf{r}',\mathbf{r};\omega)\nabla' P(\mathbf{r}';\omega)\Big] \cdot d\mathbf{S}' \end{aligned} \tag{4.6}$$

This equation provides the physical solution P to Equation (4.1), with any solution G_0 that satisfies Equation (4.2). If we choose a volume V such that $\rho(\mathbf{r}';\omega) = 0$ for $\mathbf{r}'$ inside V (as shown by Figure 4.1(a)), there is

$$P(\mathbf{r};\omega) = \oint_S \Big[P(\mathbf{r}';\omega)\nabla' G_0(\mathbf{r}',\mathbf{r};\omega) - G_0(\mathbf{r}',\mathbf{r};\omega)\nabla' P(\mathbf{r}';\omega)\Big] \cdot d\mathbf{S}' \tag{4.7}$$

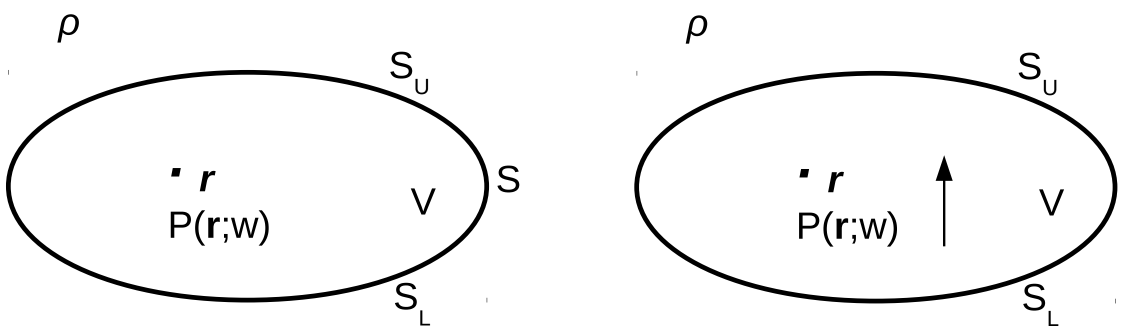

(a) **(b)**

Figure 4.1: Predict P in the volume for (a) general waves and (b) one-way propagating waves from only measurements on S_U use $G_0 = G_0^-$ (Stolt and Weglein, 2012).

As long as G_0 satisfies Equation (4.2) inside V, G_0 can be put any conditions on it and Equation (4.7) always produce the total field at $\mathbf{r}$ inside V. If the field that we are trying to predict is one-way (as shown by Figure 4.1(b)), moving up, or in other words we are trying to predict the reflected wave wavefield, you can show that if you choose the Green's function to be an anti-causal Green's function G_0^-, the upper surface (S_U) will contributes, and the lower surface (S_L) will not; hence, for one-way waves and $\mathbf{r}$ inside V

$$P(\mathbf{r};\omega) = \int_{S_U} \left[P(\mathbf{r}';\omega)\nabla' G_0^-(\mathbf{r}',\mathbf{r};\omega) - G_0^-(\mathbf{r}',\mathbf{r};\omega)\nabla' P(\mathbf{r}';\omega)\right] \cdot d\mathbf{S}' \tag{4.8}$$

Further we can use a Dirichlet anti-causal Green's function $G_0^{-D}(\mathbf{r}',\mathbf{r};\omega) = G_0^-(\mathbf{r}',\mathbf{r};\omega) - G_0^-(\mathbf{r}',\mathbf{r}_I;\omega)$ that vanishes on the upper surface (S_U). r_I is the mirror of $\mathbf{r}$ with respect to S_U; then we will not need the normal derivative of physical field

$$P(\mathbf{r};\omega) = \int_{S_U} P(\mathbf{r}';\omega)\nabla' G_0^{-D}(\mathbf{r}',\mathbf{r};\omega) \cdot d\mathbf{S}' \tag{4.9}$$

This actually leads to prestack Stolt migration Stolt (1978) in Green's theorem formulation (horizontal measurement surfaces) that predicts the wavefield for new source

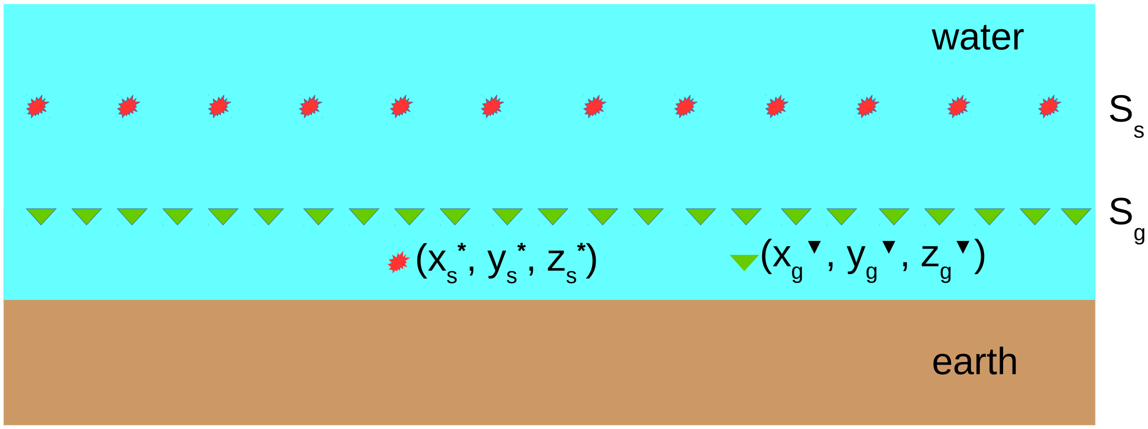

Figure 4.2: Principle of Green's theorem wavefield prediction.

and receiver location for an upgoing wavefield

$$P = \int_{S_s} \frac{\partial G_0^{-D}}{\partial z_s} \int_{S_g} \frac{\partial G_0^{-D}}{\partial z_g} P dS_g dS_s \tag{4.10}$$

Figure 4.2 shows the configuration of Equation (4.10) in marine setting. (x_s, y_s, z_s) and (x_g, y_g, z_g) are source location and receiver location of data $P(x_g, y_g, z_g, x_s, y_s, z_s; \omega)$ that has got rid of ghosts, free surface multiples and internal multiples. Sources and receivers lie on S_s and S_g, respectively. According to Equation (4.10), the predicted wavefield (primary) for new source $(x_s^\star, y_s^\star, z_s^\star)$ and new receiver $(x_g^\blacktriangledown, y_g^\blacktriangledown, z_g^\blacktriangledown)$ (Stolt and Weglein, 1985, 2012; Weglein et al., 2011a,b) is

$$\begin{aligned}
&P(x_g^\blacktriangledown, y_g^\blacktriangledown, z_g^\blacktriangledown, x_s^\star, y_s^\star, z_s^\star; \omega) \qquad (4.11)\\
&= \int_{S_s} dx_s dy_s \Bigg\{ \frac{\partial}{\partial z_s'} G_0^{-D}(x_s^\star, y_s^\star, z_s^\star, x_s, y_s, z_s'; \omega)\Big|_{z_s'=z_s} \\
&\qquad \int_{S_g} dx_g dy_g \left[\frac{\partial}{\partial z_g'} G_0^{-D}(x_g^\blacktriangledown, y_g^\blacktriangledown, z_g^\blacktriangledown, x_g, y_g, z_g'; \omega)\Big|_{z_g'=z_g} P(x_g, y_g, z_g, x_s, y_s, z_s; \omega) \right] \Bigg\} \\
&= \int_{S_s} \int_{S_g} dx_s dy_s dx_g dy_g \Bigg[\frac{\partial}{\partial z_s'} G_0^{-D}(x_s^\star, y_s^\star, z_s^\star, x_s, y_s, z_s'; \omega)\Big|_{z_s'=z_s} \\
&\qquad P(x_g, y_g, z_g, x_s, y_s, z_s; \omega) \frac{\partial}{\partial z_g'} G_0^{-D}(x_g^\blacktriangledown, y_g^\blacktriangledown, z_g^\blacktriangledown, x_g, y_g, z_g'; \omega)\Big|_{z_g'=z_g} \Bigg]
\end{aligned}$$

Here G_0^{-D} is the Dirichlet Green's function constructed by anticausal Green's function, to vanish on the M.S. Its expression is given by

$$G_0^{-D}(x_s^\star, y_s^\star, z_s^\star, x_s, y_s, z_s'; \omega) \tag{4.12}$$
$$= G_0^-(x_s^\star, y_s^\star, z_s^\star, x_s, y_s, z_s'; \omega) - G_0^-(x_s^\star, y_s^\star, z_s^\star, x_s, y_s, 2z_s - z_s'; \omega)$$

and

$$G_0^{-D}(x_g^\blacktriangledown, y_g^\blacktriangledown, z_g^\blacktriangledown, x_g, y_g, z_g'; \omega) \tag{4.13}$$
$$= G_0^-(x_g^\blacktriangledown, y_g^\blacktriangledown, z_g^\blacktriangledown, x_g, y_g, z_g'; \omega) - G_0^-(x_g^\blacktriangledown, y_g^\blacktriangledown, z_g^\blacktriangledown, x_g, y_g, 2z_g - z_g'; \omega)$$

where $G_0^-(\mathbf{r}, \mathbf{r}'; \omega) = -\frac{1}{4\pi}\frac{exp(-ik|\mathbf{r}-\mathbf{r}'|)}{|\mathbf{r}-\mathbf{r}'|}$ is the anticausal Green's function. According to Claerbout imaging condition III, the depth imaging is

$$M(x_m, y_m, z_m, x_h, y_h, z_h = 0; t = 0) \tag{4.14}$$

where $x_m = \frac{1}{2}(x_g^\blacktriangledown + x_s^\star)$, $y_m = \frac{1}{2}(y_g^\blacktriangledown + y_s^\star)$, $z_m = \frac{1}{2}(z_g^\blacktriangledown + z_s^\star)$, $x_h = \frac{1}{2}(x_g^\blacktriangledown - x_s^\star)$, $y_h = \frac{1}{2}(y_g^\blacktriangledown - y_s^\star)$, and $z_h = \frac{1}{2}(z_g^\blacktriangledown - z_s^\star)$. It first resorts the predicted $P(x_g^\blacktriangledown, y_g^\blacktriangledown, z_g^\blacktriangledown, x_s^\star, y_s^\star, z_s^\star; \omega)$ into midpoint gather and lets $z_g^\blacktriangledown = z_s^\star$. Then after transformation into time domain, it chooses the wavefield at zero time.

4.2 1D analytic example

As we do in previous chapters, we first use a 1D analytic example to test Equation (4.11). Suppose the depth of source, receiver and water bottom is z_s, z_g and z_{wb}, respectively. The data with ghosts and multiples removed (i.e., the primary from the water bottom) are

$$P(z_g, z_s; \omega) = \frac{e^{ik(z_{wb}-z_s)}}{2ik} R e^{i(-k)(z_g - z_{wb})} = \frac{R}{2ik} e^{ik(2z_{wb}-z_s-z_g)} \tag{4.15}$$

In the case of 1D source and 1D earth, Equation (4.11) becomes

$$P(z_g^{\blacktriangledown}, z_s^{\star}; \omega) = \frac{\partial}{\partial z_s'} G_0^{-D}(z_s^{\star}, z_s'; \omega)\Big|_{z_s'=z_s} P(z_g, z_s; \omega) \frac{\partial}{\partial z_g'} G_0^{-D}(z_g^{\blacktriangledown}, z_g'; \omega)\Big|_{z_g'=z_g} \tag{4.16}$$

Here

$$\begin{aligned} G_0^{-D}(z_s^{\star}, z_s'; \omega) &= G_0^{-}(z_s^{\star}, z_s'; \omega) - G_0^{-}(z_s^{\star}, 2z_s - z_s'; \omega) \\ &= -\frac{e^{-ik|z_s^{\star}-z_s'|}}{2ik} + \frac{e^{-ik|z_s^{\star}+z_s'-2z_s|}}{2ik} \end{aligned} \tag{4.17}$$

$$\begin{aligned} G_0^{-D}(z_g^{\blacktriangledown}, z_g'; \omega) &= G_0^{-}(z_g^{\blacktriangledown}, z_g'; \omega) - G_0^{-}(z_g^{\blacktriangledown}, 2z_g - z_g'; \omega) \\ &= -\frac{e^{-ik|z_g^{\blacktriangledown}-z_g'|}}{2ik} + \frac{e^{-ik|z_g^{\blacktriangledown}+z_g'-2z_g|}}{2ik} \end{aligned} \tag{4.18}$$

Hence, for $z_s^{\star} > z_s' = z_s$ and $z_g^{\blacktriangledown} > z_g' = z_g$

$$\begin{aligned} &\frac{\partial}{\partial z_s'} G_0^{-D}(z_s^{\star}, z_s'; \omega) \\ &= -\frac{1}{2ik} e^{-ik|z_s^{\star}-z_s'|}(-ik) sgn(z_s' - z_s^{\star}) + \frac{1}{2ik} e^{-ik|z_s^{\star}+z_s'-2z_s|}(-ik) sgn(z_s' + z_s^{\star} - 2z_s) \\ &= -\frac{1}{2} e^{-ik(z_s^{\star}-z_s)} - \frac{1}{2} e^{-ik(z_s^{\star}-z_s)} \\ &= -e^{-ik(z_s^{\star}-z_s)} \end{aligned} \tag{4.19}$$

$$\begin{aligned} &\frac{\partial}{\partial z_g'} G_0^{-D}(z_s^{\blacktriangledown}, z_g'; \omega) \\ &= -\frac{1}{2ik} e^{-ik|z_g^{\blacktriangledown}-z_g'|}(-ik) sgn(z_g' - z_g^{\blacktriangledown}) + \frac{1}{2ik} e^{-ik|z_g^{\blacktriangledown}+z_g'-2z_g|}(-ik) sgn(z_g' + z_g^{\blacktriangledown} - 2z_g) \\ &= -\frac{1}{2} e^{-ik(z_g^{\blacktriangledown}-z_g)} - \frac{1}{2} e^{-ik(z_g^{\blacktriangledown}-z_g)} \\ &= -e^{-ik(z_g^{\blacktriangledown}-z_g)} \end{aligned} \tag{4.20}$$

Therefore, substituting into Equation (4.16),

$$P(z_g^{\blacktriangledown}, z_s^{\star}; \omega) = \frac{R}{2ik} e^{ik(2z_{wb} - z_s^{\star} - z_g^{\blacktriangledown})} \tag{4.21}$$

Compared with Equation (4.15), this is the predicted primary for new source at $z_s^{\star}$ and new receiver at $z_g^{\blacktriangledown}$.

4.3 Numerical tests

4.3.1 The impact of preprocessing that assumes horizontal measurement surface on Stolt CIII imaging

Figure 4.3 shows that imaging result based on Formula (4.11) and Claerbout imaging condition III, using data (the predicted primary) that have gone through deghosting and FSME. Here x_h, y_h, and z_h are set to 0, meaning predicted source and receiver location coincide at all depth and midpoint. From Figure 4.3(a), 4.3(b), and 4.4, we can see the indication of reflector location is quite accurate (the zero point of imaging trace is close to 50 m depth) when the M.S. is (very close to) horizontal. Although the inclination of M.S. makes the imaging deviate from real depth of the reflector and the imaging using 2° M.S. (- · -) deviates more than the imaging using 1° M.S. (- - -), such deviation is quite little since the inclination angle is small.

However, the imaging result (Figure 4.3(c)) is ineffective since previous deghosting assumes horizontal M.S. while it's actually undulated.

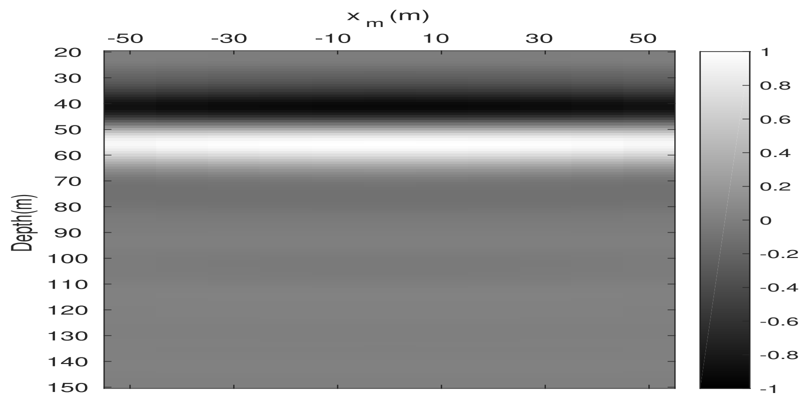

(a)

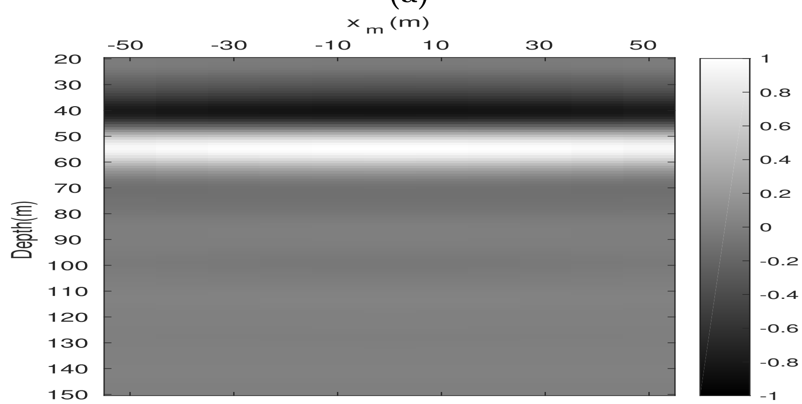

(b)

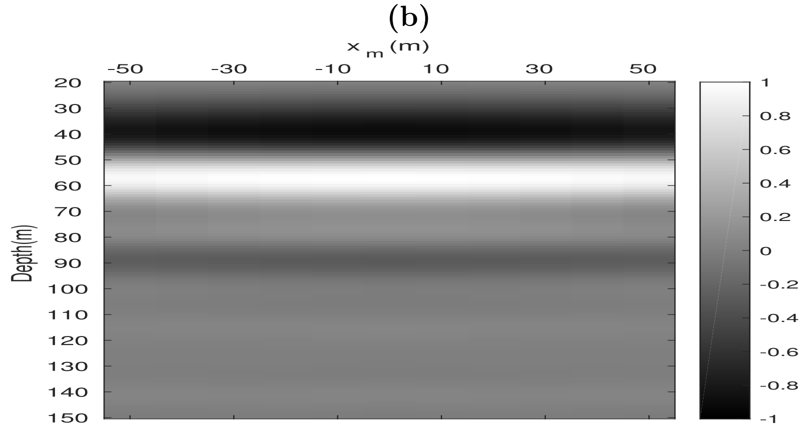

(c)

Figure 4.3: Depth imaging results. **(a)** Imaging using predicted primary Figure 3.2(b) as input, **(b)** imaging using predicted primary Figure 3.2(d) as input, and **(c)** imaging using predicted primary Figure 3.2(f) as input. Colorbar on the right represents the amplitude.

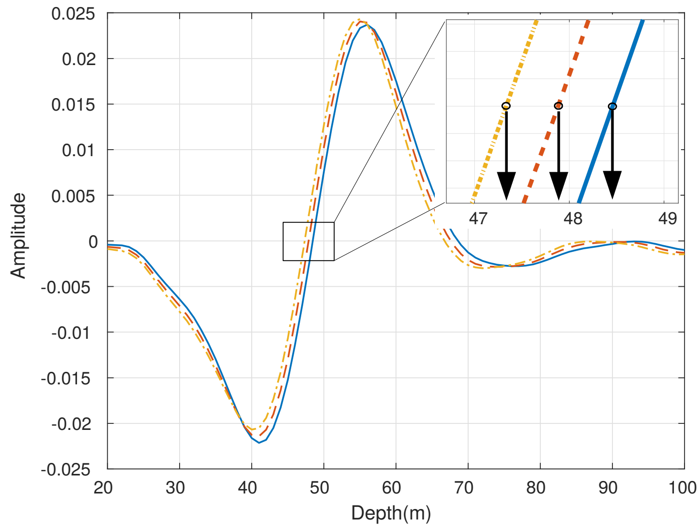

Figure 4.4: Traceplot ($x_m = 0$ m) comparison of imaging result Figure 4.3(a) (——) with horizontal M.S., imaging result with 1° inclined M.S. assuming it's horizontal in deghosting (- - -) and Figure 4.3(b) (- · -) with 2° inclined M.S. assuming it's horizontal in deghosting.

4.3.2 Results using preprocessing that accommodates the topography of the measurement surface

Figure 4.5 shows the imaging result with accommodation of topography of the M.S. in deghosting, which recovers effectiveness.

Figure 4.6 shows the contrast in trace between Figure 4.3(a), 4.3(c) and 4.5, where we can see the impact on resolution. The impact of acquisition that is actually undulated but assumed horizontal in deghosting causes 150% increase in the sidelobe from the horizontal acquisition case. Such major consequence appears because the impact of ignoring the topography of acquisition is accumulative throughout deghosting and all subsequent processing. In contrast, the accommodation of acquisition undulation in deghosting greatly reduce the impact to just 12%. This means the accommodation of the undulated acquisition in deghosting is successful and does greatly benefit the

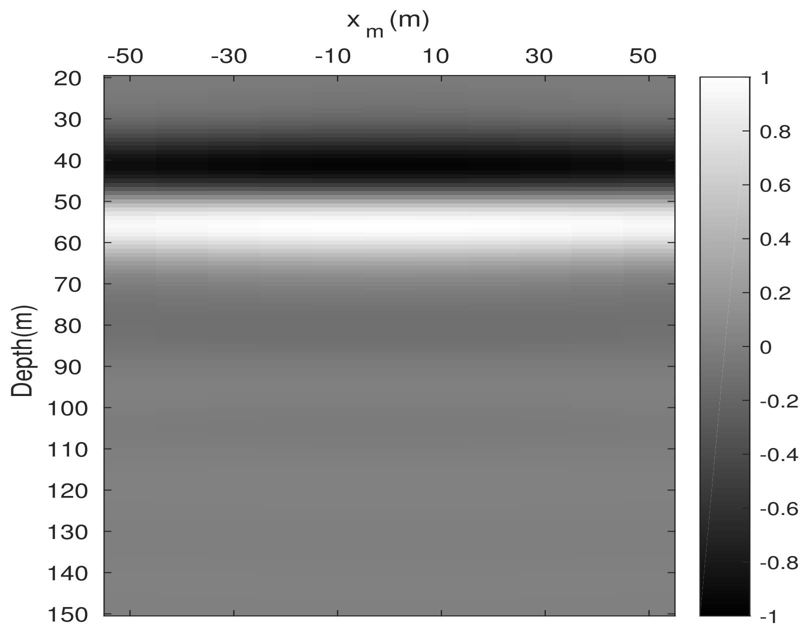

Figure 4.5: Imaging result using predicted primary Figure 3.4(b) as input. Colorbar on the right represents the amplitude.

subsequent free surface multiple elimination and depth imaging.

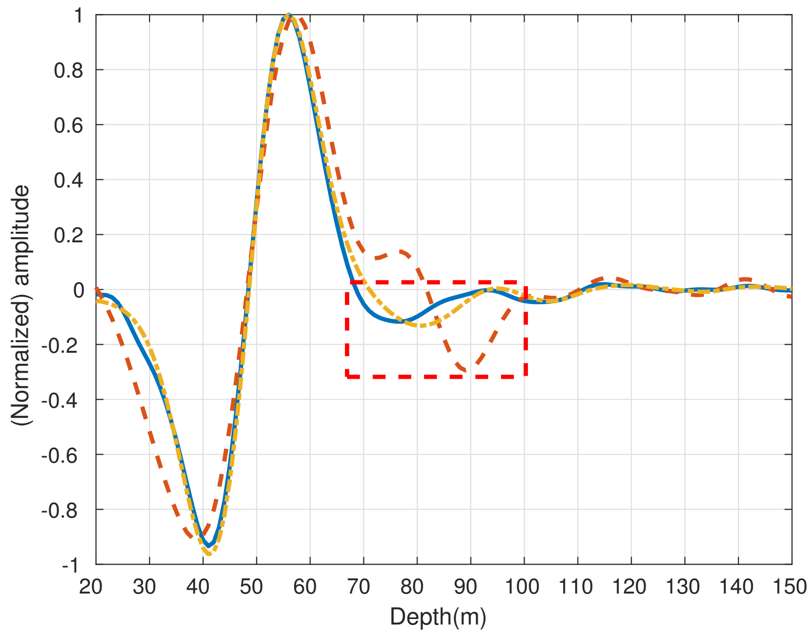

(a)

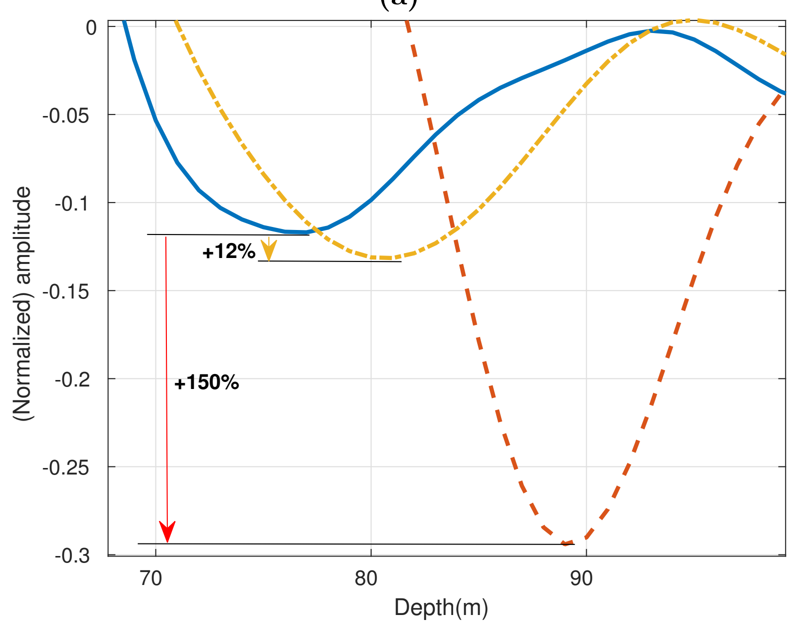

(b)

Figure 4.6: (a) Traceplot ($x_m = 0$ m) comparison of Figure 4.3(a) (——), Figure 4.3(c) (- - -) and Figure 4.5 (- · -) and (b) zoomed view of the red box in (a).

4.4 Discussions

One interesting topic to study is the influence of acquisition **directly** on the imaging **alone**. That is, what the imaging result will be, if the seismic data are acquired along a non-horizontal measurement surface (M.S.) and we perform the removal of the reference wave, the ghosts, and the multiples accommodating the non-horizontal acquisition, while we treat the non-horizontal measurement surface as horizontal in seismic migration. The following numerical example will show the consequence of accommodating/not accommodating the acquisition geometry on seismic imaging. Here, I want to deeply thank **Dr. Qiang Fu** for realization of the migration in the latter tests.

To begin, Figure 4.7 shows the velocity model used to generate synthetic data for the imaging tests. It has a horizontal reflector at 50 m depth. No free surface exists as we assume the reference removal, deghosting and the free surface multiple removal have already been effectively achieved. The source depth is at 5 m. Figure 4.9(a) shows the synthetic data generated on a measurement surface (Figure 4.8(a)) at 35 m depth. Figure 4.9(b) shows the synthetic data generated on a undulated M.S. (Figure 4.8(b)) whose depth varies from 25 m to 45 m. The Stolt CIII imaging results using the reflection data generated on the horizontal measurement surface at 35 m depth (Figure 4.9(a)) and the reflection data generated on the undulated measurement surface (Figure 4.9(b)) as input are shown by Figure 4.10 and Figure 4.11, respectively. We can see Figure 4.10 shows that the imaging is in agreement with 50 m, the depth of the reflector. In this case, the imaging is accurate and effective.

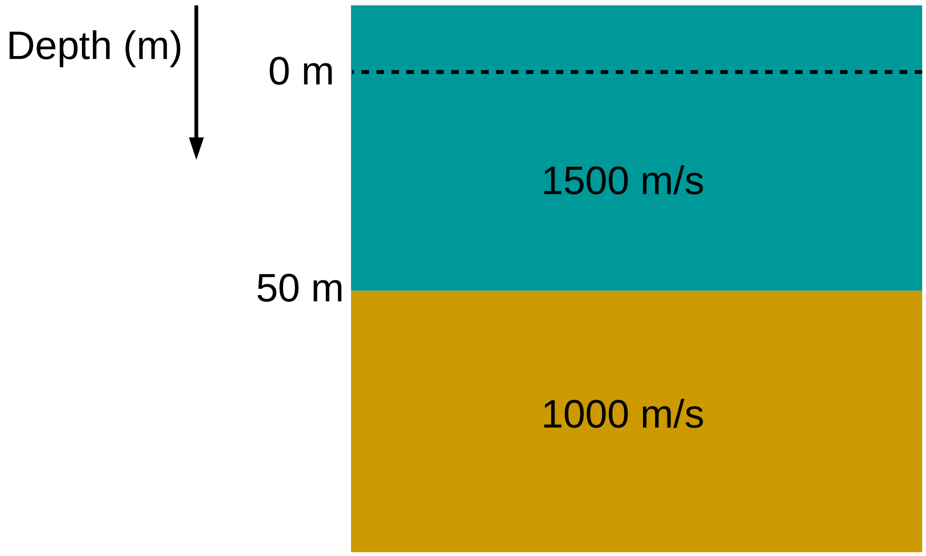

Figure 4.7: Velocity model. Two layers are half-space.

However, as shown by Figure 4.11, the undulating acquisition that is assumed to be horizontal leads to an erroneous undulating imaging result.

This latter erroneous imaging result has very practical meaning and interpretation. It communicates that, although the reflector is horizontal and flat, the unrealistic non-flat geological structure may appear in imaging results, if the measurement surface is non-horizontal and we ignore its geometry. In other words, without accommodating the geometry of acquisition in migration or previous processing steps, artifacts will appear in the imaging result that distort the characterization of subsurface structure and can mislead subsequent interpretation.

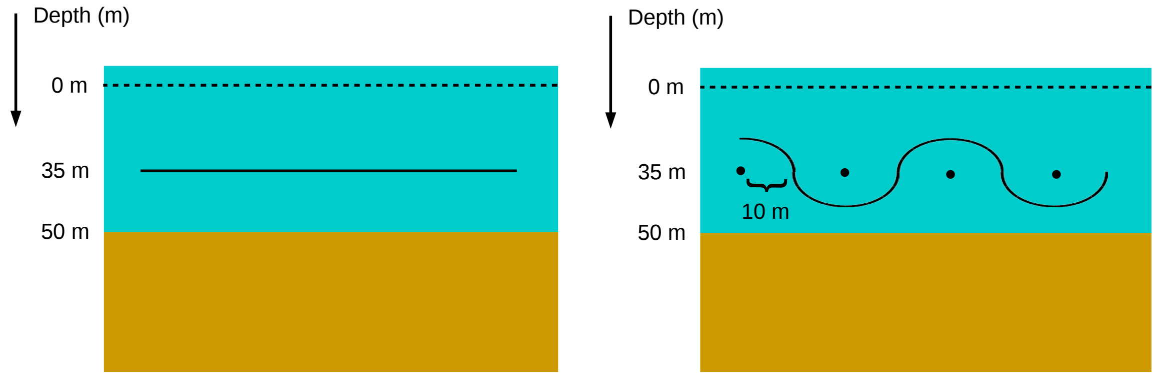

(a) **(b)**

Figure 4.8: (a) Horizontal acquisition, and (b) undulated acquisition.

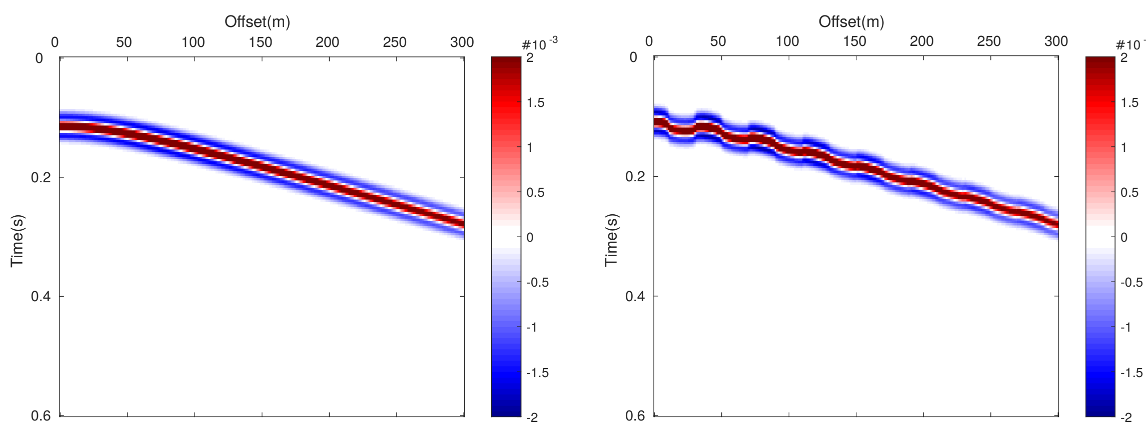

(a) **(b)**

Figure 4.9: Input data (primary only) for imaging. (a) horizontal acquisition, and (b) undulated acquisition. Colorbar on the right represents the amplitude.

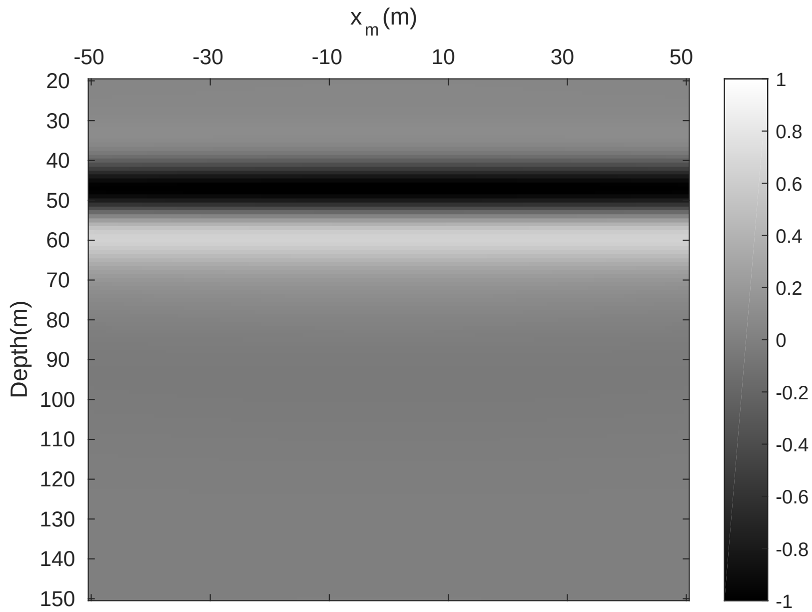

Figure 4.10: Imaging result with horizontal acquisition (Figure 4.9(a)). Colorbar on the right represents the amplitude.

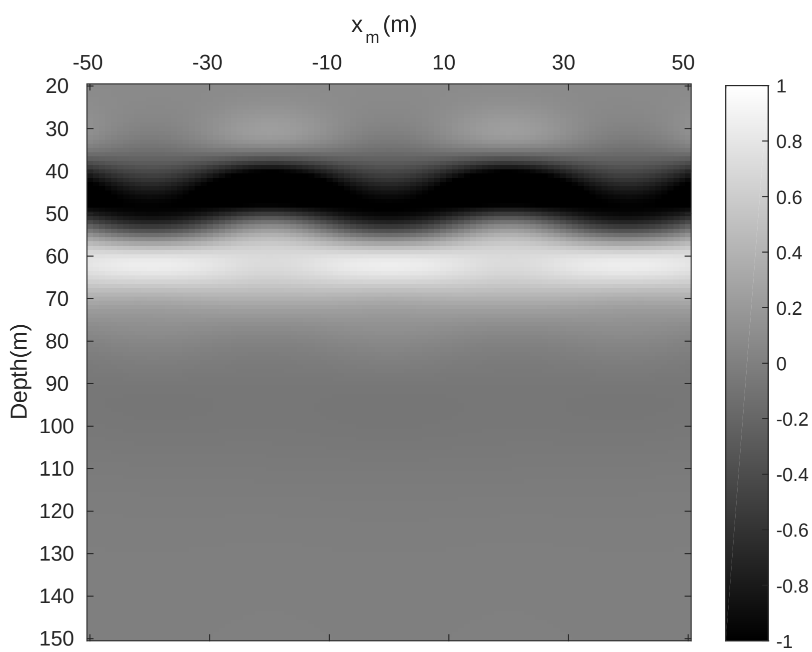

Figure 4.11: Imaging result with undulated acquisition (Figure 4.9(b)). The undulated acquisition is assumed horizontal in migration. Colorbar on the right represents the amplitude.

4.5 Conclusions

The final imaging of the case where the acquisition is close to horizontal turns out to be effective. In fact, it is quite similar to the imaging result of the case with horizontal acquisition. However, the imaging result when the acquisition is far from horizontal and assumed horizontal in deghosting has damaged resolution. This issue is successfully solved by accommodation of the geometry of acquisition in deghosting.

Chapter 5

Summary

5.1 Conclusions

This dissertation focuses on solving a practical issue in satisfying the prerequisites of seismic tasks based on Green's theorem and the inverse scattering series (ISS). This issue is the topography of the measurement surface where seismic data are collected. It has to be incorporated into seismic preprocessing so that the prerequisites of preprocessing and subsequent processing are better satisfied, allowing the latter to achieve their processing and interpretation goals and objectives.

In Chapter 2, the Green's theorem P_0/P_s separation algorithm and source and receiver deghosting algorithm are developed and tested for depth-variable towed streamer acquisition. This is also (particularly) relevant to ocean-bottom preprocessing when the ocean bottom is non-horizontal, and to on-shore preprocessing since the earth's surface can have significant lateral variability. Numerical examples show that if data are acquired on a non-horizontal measurement surface, the horizontal acquisition assumption can provide effective preprocessing results when the measurement surface is close to horizontal. If the measurement surface deviates significantly from horizontal, the current preprocessing algorithms which assume it's horizontal may lead to inaccurate and injurious results. In this case, the new Green's theorem preprocessing formula proposed in this dissertation can provide effective results, by incorporating the topography of the measurement surface.

Chapter 3 and Chapter 4 analyze the impact from making a horizontal acquisition assumption in preprocessing (which is studied in Chapter 2), on subsequent ISS free surface multiple elimination (FSME) and further Stolt CIII imaging, respectively. These two seismic tasks have been currently formulated with horizontal acquisition assumptions. Numerical tests show that when the original measurement surface is close to horizontal, the horizontal acquisition assumption in deghosting doesn't bring serious artifacts to free surface multiple elimination and further imaging. Under those circumstances, these two tasks can remain effective with horizontal acquisition assumption; however, when the measurement surface deviates significantly from horizontal, the artifacts in deghosting results damage the effectiveness of free surface multiple elimination and further undermines the resolution of depth imaging results.

In Chapter 3 and 4, we address this problem when the measurement surface deviates significantly from horizontal. For free surface multiple elimination, Chapter 3 uses the deghosting result in Chapter 2 that accommodates the topography of the measurement surface. This example shows that, with the impact of acquisition undulation well resolved in deghosting, the ISS free surface multiple elimination recovers its capability. Correspondingly, the last numerical example of Chapter 4 shows that, using an effective free surface multiple elimination result as input, the Stolt CIII imaging recovers its capability as well.

Case	Actual acquisition	Assumption about acquisition	Preprocessing (Chapter 2)	ISS FSME (Chapter 3)	Imaging (Chapter 4)
1	horizontal	horizontal	effective	effective	effective
2	inclined	horizontal	effective	effective	effective
3	undulated	horizontal	ineffective	ineffective	ineffective
4	undulated	No assumption. The topography is accommodated.	effective	effective	effective

Table 5.1: Effectiveness of three steps in four numerical cases.

Table 5.1 summarizes the effectiveness of numerical results in different cases throughout preprocessing, ISS free surface multiple elimination and Stolt CIII imaging. In summary, the consequence due to mismatch between actual acquisition and horizontal assumption has to be addressed by considering and incorporating the acquisition topography in preprocessing. This is realized by new Green's theorem preprocessing methods that can accommodate any shape of measurement surface.

5.2 Future work

The study in this dissertation on Green's theorem preprocessing for towed streamer acquisition, can be and will be extended and utilized for on-shore and ocean-bottom acquisition. In fact, because the surface of land and ocean bottom can frequently be far from horizontal, the results of this dissertation are particularly relevant to those circumstances. The horizontal acquisition assumption will be examined in these two cases and addressing of the issues due to this assumption will be carried out. The different added value compared to the conventional static shift method will be examined.

The next step is to investigate the influence of on-shore near-surface properties on on-shore preprocessing. Complicated and unknown on-shore near-surface properties remain a serious issue for on-shore processing. Preprocessing methods that are independent of near-surface properties will be explored and developed.

References

Lasse Amundsen. Wavenumber-based filtering of marine point-source data. *Geophysics*, 58(9):1335–1348, 1993.

Fernanda V. Araújo, Arthur B. Weglein, Paulo M. Carvalho, and Robert H. Stolt. Inverse scattering series for multiple attenuation: An example with surface and internal multiples. pages 1039–1041. SEG Technical Program Expanded Abstracts 1994, 1994.

Fred J. Barr and Joe I. Sanders. Attenuation of watercolumn reverberations using pressure and velocity detectors in a waterbottom cable. pages 653–656. SEG Technical Program Expanded Abstracts 1989, 2005.

Edip Baysal, Dan D. Kosloff, and John W. C. Sherwood. Reverse time migration. *Geophysics*, 48(11):1514–1524, 1983.

David H. Carlson, Andrew Long, W Söllner, H Tabti, Rune Tenghamn, and Nils Lunde. Increased resolution and penetration from a towed dual-sensor streamer. *First Break*, 25(12), 2007.

Paulo M. Carvalho. *Free surface multiple reflection elimination method based on nonlinear inversion of seismic data*. PhD thesis, Universidade Federal da Bahia, 1992.

Paulo M. Carvalho and Arthur B. Weglein. Wavelet estimation for surface multiple attenuation using a simulated annealing algorithm. pages 1481–1484. SEG Technical Program Expanded Abstracts 1994, 2005.

Paulo M. Carvalho, Arthur B. Weglein, and Robert H. Stolt. Examples of a nonlinear inversion method based on the t matrix of scattering theory: Application to multiple suppression. pages 1319–1322. SEG Technical Program Expanded Abstracts 1991, 1991.

Paulo M. Carvalho, Arthur B. Weglein, and Robert H. Stolt. Nonlinear inverse scattering for multiple suppression: Application to real data. part i. pages 1093–1095. SEG Technical Program Expanded Abstracts 1992, 1992.

Jon F. Claerbout. Toward a unified theory of reflector mapping. *Geophysics*, 36(3): 467–481, 1971.

Marsden Dave. Static corrections-a review, part i, part ii, part iii. *The Leading Edge*, 12(1):2, 1993.

William H. Dragoset Jr. Processing for seismic data from slanted cable, 1991. US Patent 4,992,992.

Zhiqiang Guo, Arthur B. Weglein, and T Hing Tan. Using pressure data on the cable to estimate the seismic wavelet. Society of Exploration Geophysicists, 2005 SEG Annual Meeting, 2005.

Luc T. Ikelle, Graham Roberts, and Arthur B. Weglein. Source signature estimation based on the removal of first-order multiples. *Geophysics*, 62(6):1904–1920, 1997.

Timothy H. Keho, Arthur B. Weglein, and Peter G. Rigsby. Marine source wavelet and radiation pattern estimation. pages 1655–1657. SEG Technical Program Expanded Abstracts 1990, 1990.

Hong Liang. *Addressing several key outstanding issues and extending the capability of the inverse scattering subseries for internal multiple attenuation, depth imaging, and parameter estimation*. PhD thesis, University of Houston, 2013.

Xinglu Lin and Arthur B. Weglein. The significance and impact of incorporating a 3D point source in Green's theorem deghosting. pages 4766–4771. SEG Technical Program Expanded Abstracts 2016, 2016.

Fang Liu and Arthur B. Weglein. The first wave equation migration RTM with data consisting of primaries and internal multiples- theory and 1D examples. *Journal of Seismic Exploration*, 23(4):357–366, 2014.

James D. Mayhan. *Wave-theoretic preprocessing to allow the inverse scattering series methods for multiple removal and depth imaging to realize their potential and impact*. PhD thesis, University of Houston, 2013.

James D. Mayhan and Arthur B. Weglein. First application of Green's theorem-derived source and receiver deghosting on deep-water Gulf of Mexico synthetic (SEAM) and field data. *Geophysics*, 78(2):WA77–WA89, 2013.

George A. McMechan. Migration by extrapolation of time-dependent boundary values. *Geophysical Prospecting*, 31(3):413–420, 1983.

Nick Moldoveanu, Leendert Combee, Mark Egan, Gary Hampson, Larry Sydora, and William Abriel. Over/under towed-streamer acquisition: A method to extend seismic bandwidth to both higher and lower frequencies. *The Leading Edge*, 26(1): 41–58, 2007.

Philip M. Morse and Herman Feshbach. *Methods of theoretical physics*. Technology Press, 1946.

Kemal A. Özdemir, Philippe Caprioli, Ali zbek, Ed Kragh, and Johan O. A. Robertsson. Optimized deghosting of over/under towed-streamer data in the presence of noise. *The Leading Edge*, 27(2):190–199, 2008.

Ben J. Posthumus. Deghosting of twin streamer configuration. *Geophysical Prospecting*, 41(3):267–286, 1993.

Clifford H. Ray and Neil A. Moore. High resolution, marine seismic stratigraphic system, 1982. US Patent 4,353,121.

Johan O. A. Robertsson, Ian Moore, Massimiliano Vassallo, Kemal Oezdemir, Dirk-Jan van Manen, and Ali Oezbek. On the use of multicomponent streamer recordings for reconstruction of pressure wavefields in the crossline direction. *Geophysics*, 73(5):A45–A49, 2008.

Enders A. Robinson and Sven Treitel. *Digital imaging and deconvolution: The ABCs of seismic exploration and processing*. Society of Exploration Geophysicists, 2008.

Simon A. Shaw. *An inverse scattering series algorithm for depth imaging of reflection data from a layered acoustic medium with an unknown velocity model*. PhD thesis, 2005.

Yuchang Shen. *Wave-theory-based seismic data preprocessing: an extension of the current deghosting method to allow for a variable measurement surface topography and its impact on the inverse scattering series multiple removal*. PhD thesis, University of Houston, 2017.

Robert E. Sheriff. *5. E*, pages 112–128. 2002.

Robert Soubaras. Deghosting by joint deconvolution of a migration and a mirror migration. pages 3406–3410. SEG Technical Program Expanded Abstracts 2010, 2010.

Robert H. Stolt. Migration by Fourier-transform. *Geophysics*, 43(1):23–48, 1978.

Robert H. Stolt and Arthur B. Weglein. Migration and inversion of seismic data. *Geophysics*, 50(12):2458–2472, 1985.

Robert H. Stolt and Arthur B. Weglein. *Seismic imaging and inversion: Volume 1: Application of linear inverse theory*, volume 1. Cambridge University Press, 2012.

Lars Snneland, Lurs E. Berg, Per Eidsvig, Arild Haugen, Bente Fotland, and Jan Vestby. 2d deghosting using vertical receiver arrays. pages 516–519. SEG Technical Program Expanded Abstracts 1986, 2005.

Lin Tang. *Developing and analyzing Green's theorem methods to satisfy prerequisites of inverse scattering series multiple attenuation for different types of marine acquisition*. PhD thesis, University of Houston, 2014.

Lin Tang and Arthur B. Weglein. Predicting reference medium properties from invariances in Green's theorem reference wave prediction: toward an onshore near surface medium and reference wave prediction. SEG Technical Program Expanded Abstracts 2014, 2014.

Francis Anthony Van Melle and Ken R. Weatherburn. Ghost reflections caused by energy initially reflected above the level of the shot. *Geophysics*, 18(4):793–804, 1953.

Massimiliano Vassallo, Kurt Eggenberger, Dirk-Jan van Manen, Ali zbek, and Peter Watterson. Broadband and beyond with marine towed streamers. *The Leading Edge*, 32(11):1356–1365, 2013.

Arthur B. Weglein. Multiples: Signal or noise? *Geophysics*, 81(4):V283–V302, 2016a.

Arthur B. Weglein. 2016 SEG M-OSRP executive summary presentation: Our technical strategy, plans and impactful advances, contributions and deliveries. Mission-Oriented Seismic Research Program (M-OSRP), 2016b.

Arthur B. Weglein and Bruce G. Secrest. Wavelet estimation for a multidimensional acoustic or elastic earth. pages 936–938. SEG Technical Program Expanded Abstracts 1988, 1988.

Arthur B. Weglein and Bruce G. Secrest. Wavelet estimation for a multidimensional acoustic or elastic earth. *Geophysics*, 55(7):902–913, 1990.

Arthur B. Weglein, W. E. Boyse, and J. E. Anderson. Obtaining three-dimensional velocity information directly from reflection seismic data: An inverse scattering formalism. *Geophysics*, 46(8):1116–1120, 1981.

Arthur B. Weglein, Fernanda Araújo Gasparotto, Paulo M. Carvalho, and Robert H. Stolt. An inverse-scattering series method for attenuating multiples in seismic reflection data. *Geophysics*, 62(6):1975–1989, 1997.

Arthur B. Weglein, Ting H. Tan, Simon A. Shaw, Kenneth H. Matson, and Douglas J. Foster. Prediction of the wavefield anywhere above an ordinary towed streamer: Application to source waveform estimation, demultiple, deghosting, data reconstruction and imaging: 70th annual international meeting. pages 2413–2415. SEG, Expanded Abstracts, 2000.

Arthur B. Weglein, Simon A. Shaw, Kenneth H. Matson, J. L. Sheiman, Robert H. Stolt, Ting H. Tan, Are Osen, G. P. Correa, Kristopher A. Innanen, Zhiqiang Guo, and Jingfeng Zhang. New approaches to deghosting towedstreamer and oceanbottom pressure measurements. pages 2114–2117. SEG Technical Program Expanded Abstracts 2002, 2002.

Arthur B. Weglein, Fernanda V. Arajo, Paulo M. Carvalho, Robert H. Stolt, Kenneth H. Matson, Richard T. Coates, Dennis Corrigan, Douglas J. Foster, Simon A. Shaw, and Haiyan Zhang. Inverse scattering series and seismic exploration. *Inverse Problems*, 19(6):R27–R85, 2003.

Arthur B. Weglein, James D. Mayhan, Lasse Amundsen, Hong Liang, Jing Wu, Lin Tang, Yi Luo, and Qiang Fu. Green's theorem deghosting algorithms in (k, omega)(eg, p-vz deghosting) as a special case of (x, omega) algorithms (based on Green's theorem) with:(1) significant practical advantages and disadvantages of algorithms in each domain, and (2) a new message, implication and opportunity for marine towed streamer, ocean bottom and on-shore acquisition and applications. *Journal of Seismic Exploration*, 22(4):389–412, 2013.

Arthur B. Weglein, James Mayhan, Yanglei Zou, Qiang Fu, Fang Liu, Jing Wu, Chao Ma, Xinglu Lin, and Robert H. Stolt. The first migration method that is equally effective for all acquired frequencies for imaging and inverting at the target and reservoir. pages 4266–4272. SEG Technical Program Expanded Abstracts 2016, 2016.

Arthur B. Weglein, Douglas J. Foster, Kenneth H. Matson, Simon A. Shaw, Paulo M. Carvalho, and Dennis Corrigan. Predicting the correct spatial location of reflectors without knowing or determining the precise medium and wave velocity: Initial concept, algorithm and analytic and numerical example. *Journal of Seismic Exploration*, 10(4):367–382, 2002.

Arthur B. Weglein, Robert H. Stolt, and James D. Mayhan. Reverse time migration and Green's theorem: Part i the evolution of concepts, and setting the stage for the new rtm method. *Journal of Seismic Exploration*, 20(1):73–90, 2011a.

Arthur B. Weglein, Robert H. Stolt, and James D. Mayhan. Reverse time migration and Green's theorem: Part ii a new and consistent theory that progresses and corrects current rtm concepts and methods. *Journal of Seismic Exploration*, 20 (2):135–159, 2011b.

Norman D. Whitmore. Iterative depth migration by backward time propagation. pages 382–385. SEG Technical Program Expanded Abstracts 1983, 1983.

Wikipedia. Structural trap. URL `https://en.wikipedia.org`.

Jing Wu and Arthur B. Weglein. Preprocessing in displacement space for on-shore seismic processing: removing ground roll and ghosts without damaging the reflection data. pages 4626–4630. SEG Technical Program Expanded Abstracts 2015, 2015a.

Jing Wu and Arthur B. Weglein. Preprocessing in the ps space for on-shore seismic processing: removing ground roll and ghosts without damaging the reflection data. pages 4740–4744. SEG Technical Program Expanded Abstracts 2015, 2015b.

Jing Wu and Arthur B. Weglein. Predicting deghosted reflection data for both pressure and multicomponent displacements at the ocean bottom. pages 4751–4755. SEG Technical Program Expanded Abstracts 2016, 2016a.

Jing Wu and Arthur B. Weglein. Green's theorem-based onshore preprocessing: A reduced data requirement assuming a vacuum/earth model for the air/earth interface and the evaluation of the usefulness of that assumption. pages 4685–4689. SEG Technical Program Expanded Abstracts 2016, 2016b.

Jinlong Yang and Arthur B. Weglein. Accommodating the source wavelet and radiation pattern in the internal multiple attenuation algorithm: Theory and initial example that demonstrates impact. pages 4396–4401. SEG Technical Program Expanded Abstracts 2015, 2015.

Öz Yilmaz. *Seismic Data Analysis*. Society of Exploration Geophysicists, 2001.

Haiyan Zhang. *Direct non-linear acoustic and elastic inversion; towards fundamentally new comprehensive and realistic target identification*. PhD thesis, University of Houston, 2006.

Haiyan Zhang and Arthur B. Weglein. Direct nonlinear inversion of 1D acoustic media using inverse scattering subseries. *Geophysics*, 74(6, S):WCD29–WCD39, 2009a.

Haiyan Zhang and Arthur B. Weglein. Direct nonlinear inversion of multiparameter 1D elastic media using the inverse scattering series. *Geophysics*, 74(6, S):WCD15–WCD27, 2009b.

Haiyan Zhang, Arthur B. Weglein, R. G. Keys, Douglas J. Foster, and S. A. Shaw. Discrimination between pressure and fluid saturation using direct non-linear inversion method: an application to time-lapse seismic data. Society of Exploration Geophysicists, 2005 SEG Annual Meeting, 2005.

Jingfeng Zhang. *Wave theory based data preparation for inverse scattering multiple removal, depth imaging and parameter estimation: Analysis and numerical tests of Green's theorem deghosting theory*. PhD thesis, 2007.

Jingfeng Zhang and Arthur B. Weglein. Extinction theorem deghosting method using towed streamer pressure data: analysis of the receiver array effect on deghosting and subsequent free surface multiple removal. pages 2095–2098. SEG Technical Program Expanded Abstracts 2005, 2005.

Jingfeng Zhang and Arthur B. Weglein. Application of extinction theorem deghosting method on ocean bottom data. pages 2674–2678. SEG Technical Program Expanded Abstracts 2006, 2006.

Zhen Zhang and Arthur B. Weglein. 2D Green's theorem receiver deghosting in the (x-omega) domain using a depth-variable cable towards on-shore and ocean-bottom application with variable topography. pages 4735–4740. SEG Technical Program Expanded Abstracts 2016, 2016.

Appendix A

2D Green's 2nd identity

Prove that

$$\iint_S (u\nabla^2 v - v\nabla^2 u)dxdy = \oint_{\partial S} (u\nabla v - v\nabla u) \cdot \mathbf{n}dl \tag{A.1}$$

where u and v are twice continuously differentiable scalar function of x and y on a 2D domain S. ∂S and $\mathbf{n}$ are boundary and normal unit vector of S, respectively.

Prove: Green's theorem in integral calculus is as below,

$$\iint_S (\partial_x Q - \partial_y P)dxdy = \oint_{\partial S} Pdx + Qdy \tag{A.2}$$

Define a vector $\mathbf{f} = (f_1, f_2)$ where $f_1 = Q$ and $f_2 = -P$, there is

$$\begin{aligned}
\iint_S \nabla \cdot \mathbf{n} dxdy &= \iint_S (\partial_x f_1 + \partial_y f_2) dxdy \\
&= \iint_S (\partial_x Q - \partial_y P) dxdy \\
&= \oint_{\partial S} Pdx + Qdy \\
&= \oint_{\partial S} -f_2 dx + f_1 dy \\
&= \oint_{\partial S} (f_1, f_2) \cdot (dy, -dx) = \oint_{\partial S} \mathbf{f} \cdot \mathbf{n} dl
\end{aligned} \tag{A.3}$$

which is the 2D divergence theorem; then choose $\mathbf{f}$ to be $u\nabla v = (u\partial_x v, u\partial_y v)$ instead. There is

$$\iint_S \nabla \cdot (u\nabla v) dxdy = \oint_{\partial S} u\nabla v \cdot \mathbf{n} dl \tag{A.4}$$

Therefore we can get Green's 1st identity in 2D

$$\iint_S (\nabla u \cdot \nabla v + u\nabla^2 v) dxdy = \oint_{\partial S} u\nabla v \cdot \mathbf{n} dl \tag{A.5}$$

and similarly,

$$\iint_S (\nabla v \cdot \nabla u + v\nabla^2 u) dxdy = \oint_{\partial S} v\nabla u \cdot \mathbf{n} dl \tag{A.6}$$

Finally the 2D Green's 2nd identity is available by subtracting the two equations above.

Appendix B

Comparison Between Green's Theorem Wavefield Prediction Method and Convensional Elevation Static Correction Method

Elevation static correction is the static correction made to each seismic trace for elevation effects by conceptually moving the shots and receivers to a common reference surface (which is usually horizontal). It involves a constant time shift to the data trace (Dave, 1993). The simplest way to calculate the constant time shift is the following

$$\Delta t = \frac{z_g - z}{c} \tag{B.1}$$

where z is the elevation of the receiver on the reference measurement surface, z_g is the elevation of the receiver on the actual measurement surface, and c is the velocity of the medium. The elevation static correction shifts each trace of the data by their corresponding Δt and moves the actual measurement surface to the reference measurement surface. A detail tutorial on static correction can be found in Yilmaz (2001).

However, the elevation static correction is an approximation for a more complex problem (Dave, 1993). According to wave theory, moving the receiver from one elevation to another involves a surface integral of the data (Weglein et al., 2011a,b). Although the elevation static correction can serve as a good approximation for near-offset data, it will cause problems when the data come from large offset.

In order to illustrate this issue, I design a very simple numerical example to show the difference between the elevation static correction and the Green's theorem wavefield prediction. Figure B.1 shows the model that generates the data. It is an acoustic model with only one reflector. I test both the elevation static correction and Green's theorem wavefield prediction by predicting the data from the measurement surface at 20m to the measurement surface at 0m. Both results will be compared with analytic data directly generated at 0m, and the comparison will only focus on the primary event.

Figure B.2 shows the trace comparison at offset 80 m, which I consider as near

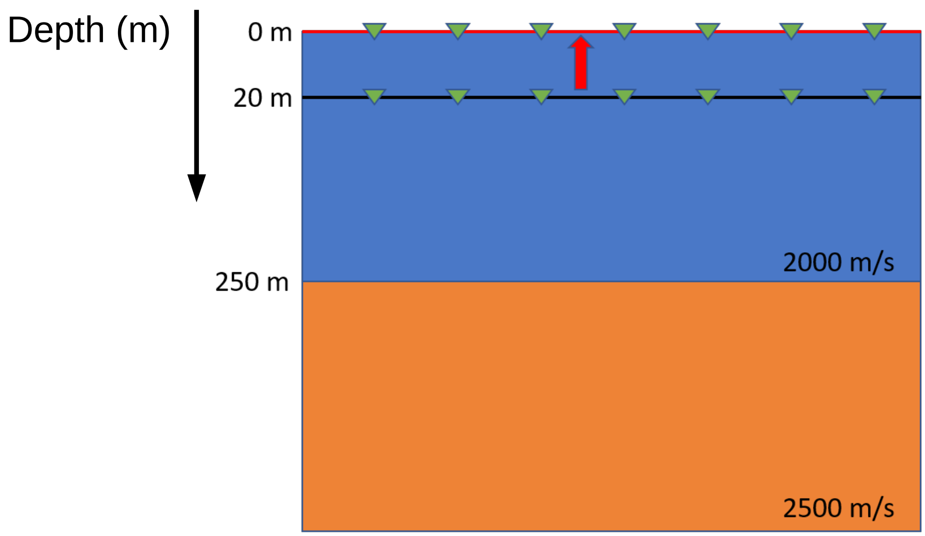

Figure B.1: The acoustic model that generate the data for comparison.

offset. This comparison shows that, the result by the Green's theorem wavefield prediction matches the analytic result very well. The time of the result by the elevation static correction matches the analytic result, but the amplitude is larger than the analytic result.

Figure B.3 shows the trace comparison at offset 3200 m, which is a far offset comparison. The comparison shows that the result by the Green's theorem wavefield prediction still matches the analytic result very well. But the elevation static correction result does not match the analytic result, neither in time nor in amplitude.

Although this numerical comparison only involves the basic form of the elevation static correction, we can conclude that the Green's theorem wavefield prediction method is in principle different from the elevation static correction method.

Another example is to illustrate the issue. A one-reflector acoustic model demonstrated by Figure B.4 is used to generate the data. The data are collected by an

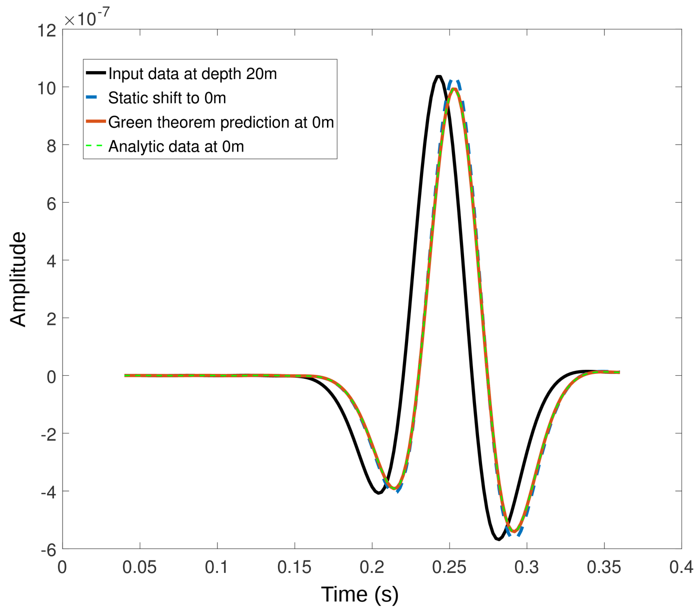

Figure B.2: The trace comparison between the input data (black solid line), static shift result (blue dashed line), Green's theorem prediction result (red solid line), and the analytic result (green dashed line) at offset 80 m.

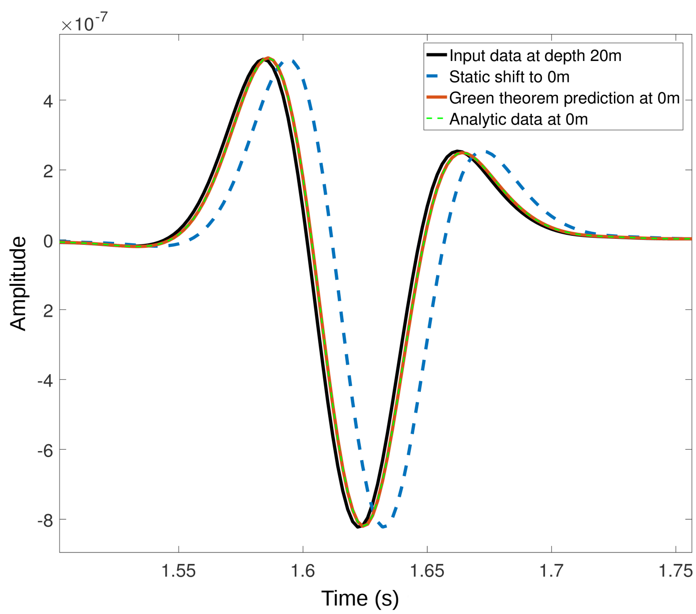

Figure B.3: The trace comparison between the input data (black solid line), static shift result (blue dashed line), Green's theorem prediction result (red solid line), and the analytic result (green dashed line) at offset 3200 m.

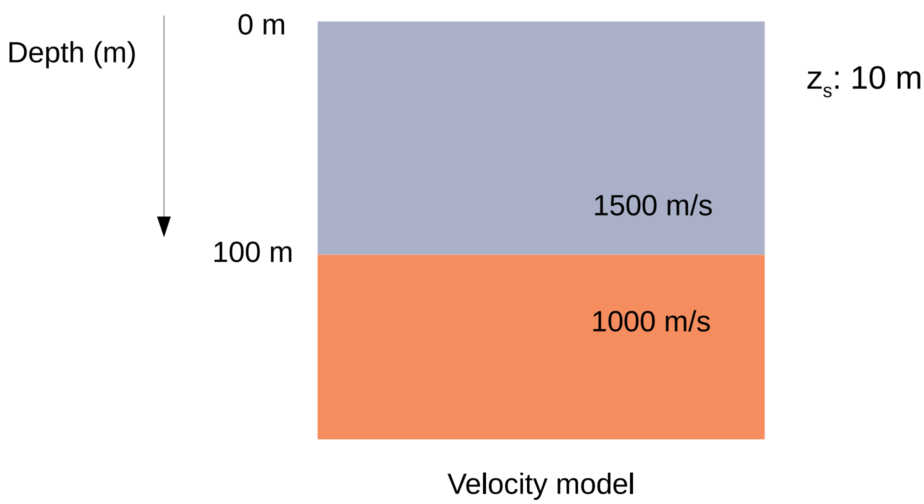

Figure B.4: The acoustic model used to generate the data for the second example.

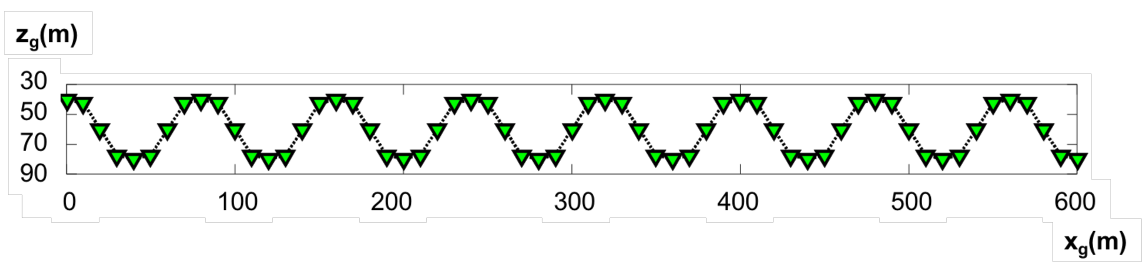

Figure B.5: The acquisition surface in the second example.

acquisition surface that consist of several identical semi-circles shown in Figure B.5. The average depth of the acquisition surface is 60 m and the radii of the semi-circles are 25 m. We only generated one primary event in this case. We will then use both the elevation static correction method and Green's theorem wavefield prediction method to predict the data from the current acquisition surface to a shallower horizontal acquisition surface located at depth 30 m.

Figure B.6 shows the input data generated from the model. Figure B.7 shows the prediction shot gather by elevation static correction method at depth 30 m and Figure B.8 shows the prediction shot gather by Green's theorem wavefield prediction

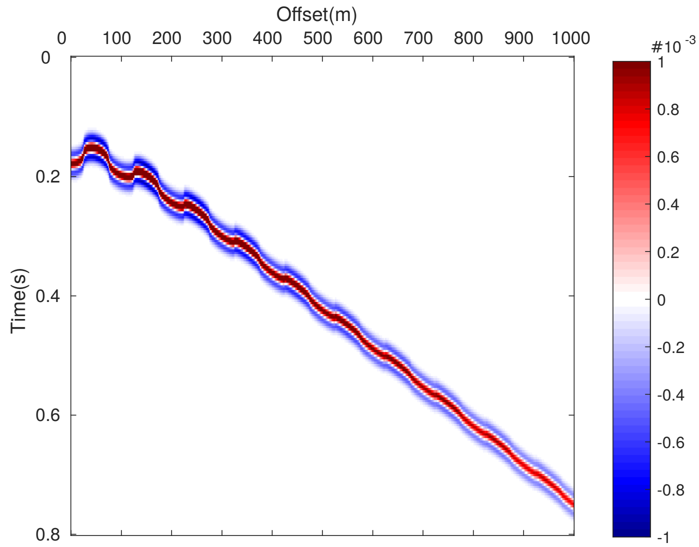

Figure B.6: The input data. Colorbar on the right represents the amplitude.

method at depth 30 m. Comparing these two results we can find that at far offset the arrival time of the predicted events are not the same.

A more detail comparison can be illustrated by the trace comparison. Figure B.9 shows the trace comparison at different offsets between the perfect result generated analytically at depth 30 m (blue solid line), the prediction by Green's theorem wavefield prediction method (red dashed line), and the prediction by elevation static correction method (black dashed line). These trace comparisons show that, the elevation static correction method can only provide a prediction with exact time at 0m offset. As the offset gets bigger, the time of the static correction result deviates more from the perfect result. The amplitude of the static correction result deviates from the perfect result at every offset. On the other hand, the prediction result from the Green's theorem wavefield prediction matches the the perfect result very well at every offset.

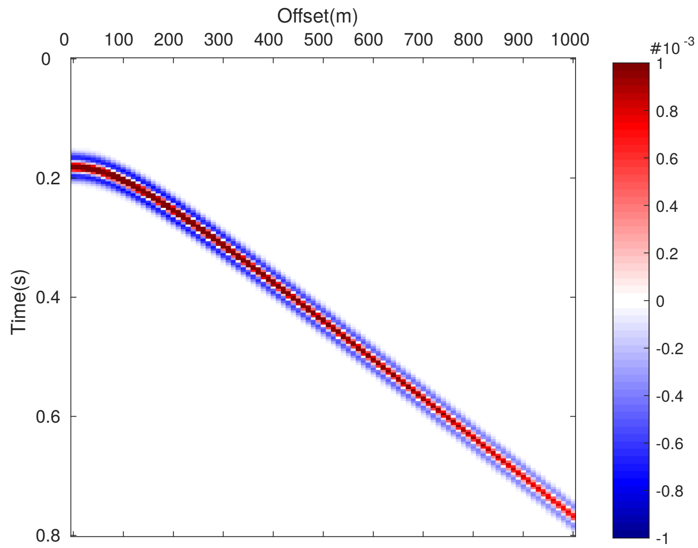

Figure B.7: Prediction result by elevation static correction at depth 30 m. Colorbar on the right represents the amplitude.

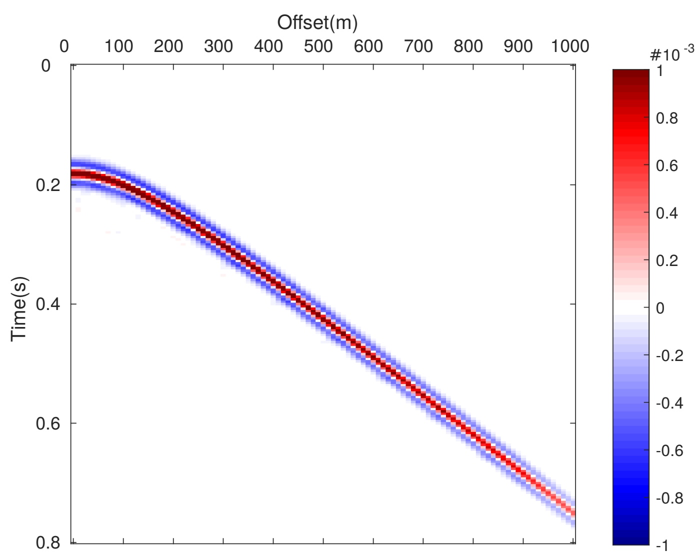

Figure B.8: Prediction result by Green's theorem wavefield prediction at depth 30 m. Colorbar on the right represents the amplitude.

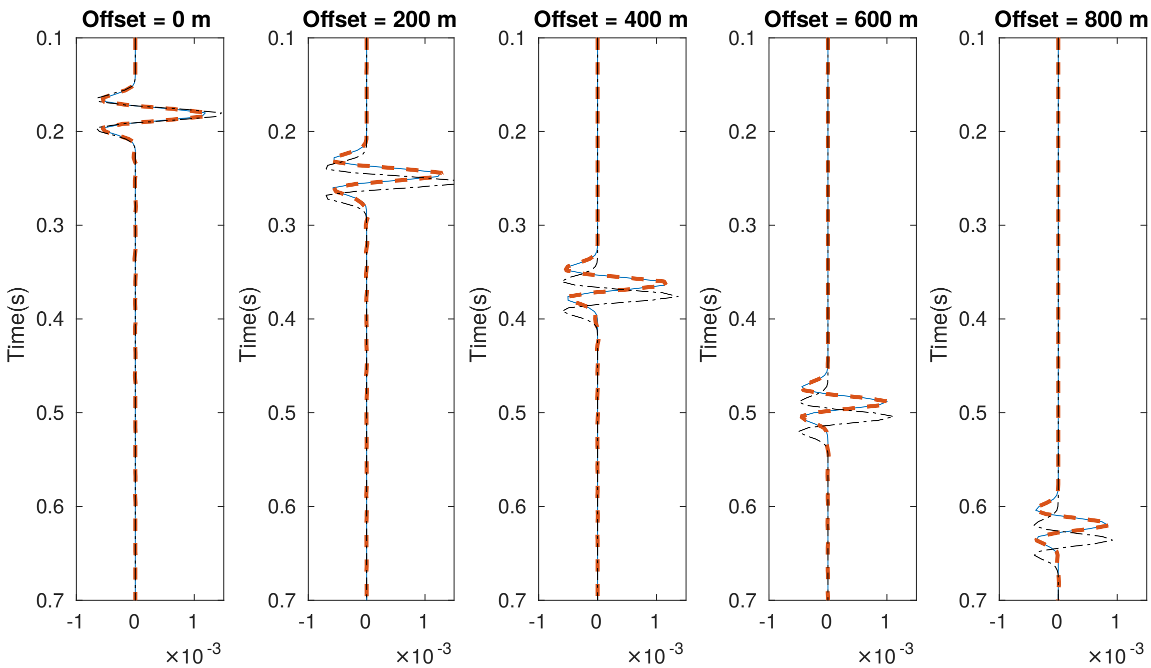

Figure B.9: Trace comparison between the perfect result generated analytically at depth 30 m (blue solid line), the prediction by Green's theorem wavefield prediction method (red dashed line), and the prediction by elevation static correction method (black dashed line) at different offsets.

The behavior of the elevation static correction method can be explained by a mathematical analysis provided by Weglein (personal communication, 2017). The elevation static correction method can be described by the following equation

$$D\left(x_g, z, t\right) = D\left(x_g, z_g, t - \Delta t\right) \tag{B.2}$$

Equation (B.2) can be derived from the wave equation as the following. Starting from the wave equation

$$\left(\nabla^2 - \frac{1}{c^2}\frac{\partial^2}{\partial t^2}\right) D\left(x_g, z_g, t\right) = 0. \tag{B.3}$$

Fourier transform over x and t,

$$\left(\frac{d^2}{dz^2} + \frac{\omega^2}{c^2} - k_g^2\right) D\left(k_g, z_g, \omega\right) = 0 \tag{B.4}$$

In the fourier domain, for a one-way wave prediction,

$$D\left(k_g, z, \omega\right) = e^{-ik_z(z-z_g)} D\left(k_g, z_g, \omega\right) \tag{B.5}$$

where

$$k_z = \sqrt{\frac{\omega^2}{c^2} - k_g^2}. \tag{B.6}$$

When k_g is small, $k_z \approx \omega/c$, so that

$$e^{-ik_z(z-z_g)} \approx e^{-i\frac{\omega}{c}(z-z_g)} = e^{i\omega\Delta t}. \tag{B.7}$$

Therefore

$$D\left(k_g, z, \omega\right) \approx e^{i\omega\Delta t} D\left(k_g, z_g, \omega\right). \tag{B.8}$$

With a stationary phase approximation (high frequency approximation),

$$
\begin{aligned}
D\left(x_g \approx 0, z, t\right) &\approx \int D\left(k_g \approx 0, z, t\right) e^{-i\omega t} d\omega \\
&= \int e^{i\omega \Delta t} D\left(k_g, z_g, \omega\right) e^{-i\omega t} d\omega \\
&= D\left(x_g \approx 0, z_g, t - \Delta t\right).
\end{aligned}
\tag{B.9}
$$

So that, at near offset $x_g \approx 0$, we have

$$
D\left(x_g, z, t\right) = D\left(x_g, z_g, t - \Delta t\right). \tag{B.10}
$$

From the above analysis we know that elevation static correction has an assumption of a horizontal acquisition surface since it involves a fourier transform at the beginning. It also involves a stationary phase approximation, which requires $k_g \approx 0$ or $x_g \approx 0$. The stationary phase approximation implies a near offset or a high frequency approximation, or equivalently, a normal incident approximation in the elevation static correction method.